

Reentrant kinetic phase transitions during dendritic growth of crystals in a two-dimensional medium with phase separation

L. M. Martyushev, V. D. Seleznev, and S. A. Skopinov

Institute of Industrial Ecology, Urals Branch of the Russian Academy of Sciences, Ekaterinburg
(Submitted January 27, 1997)

Pis'ma Zh. Tekh. Fiz. **23**, 1–6 (July 12, 1997)

Computer simulation is used to study two-dimensional dendritic growth in a medium susceptible to phase separation. It is shown that in this highly nonequilibrium system, cyclic changes in the dendrite morphology may accompany a continuous change in the concentration of phase-stratifying impurity. A close analogy is noted between this phenomenon and the reentrant phase transitions in liquid crystals. © 1997 American Institute of Physics.
[S1063-7850(97)00107-9]

Attention is now being focused on many different systems (hydrodynamic, chemical, biological, and others) in which abrupt changes in the properties and symmetry are observed at certain critical values of the thermodynamic fluxes and forces (so-called kinetic phase transitions).^{1–3} One of the most interesting systems which is of practical importance but difficult to study is the nonequilibrium growth of crystals from a solution/melt with appreciable supersaturation/supercooling, leading to the growth of skeletal and dendritic forms.⁴ The morphological characteristics of these dendritic structures are predominantly studied by computer simulation methods because of the mathematical difficulties involved in the analysis.⁵

Studies of dendritic growth in a fairly strongly supersaturated solution in the presence of a second component which, on being repelled by the moving crystal surface and reaching a certain concentration, is transformed into a different phase, thereby creating local obstacles to growth, are of major theoretical interest⁶ and also have useful practical applications.⁷ Media of this type may include a protein–salt solution, in which the protein is converted into a liquid-crystal or gel phase as a result of crystallization of the salt. A similar system was analyzed previously by the authors using a computer τ -model.⁶ It was shown that during the growth of a skeletal crystal in this phase-stratifying medium, both a continuous change in morphology and an abrupt change — kinetic phase transition — are observed. Here we use the same model to analyze the growth of a dendrite (a structure which occurs in the presence of large deviations from equilibrium as compared with a skeletal structure) in a phase-stratifying medium.

Crystal growth is simulated using the τ -model proposed in Ref. 8. We note the main features of this model.

1. The calculations are made on a square grid where each square is of dimension L . The time interval after which the concentration fields are recalculated is taken to be the time for relaxation of the concentration between two neighboring cells $\tau = L^2 / (2D_s)$, where D_s is the coefficient of diffusion of the crystallizing component (salt). Each cell is assigned a specific concentration of salt C_s and impurity C_p and initially, the concentrations in all the cells are the same, $C_{s,in}$ and $C_{p,in}$, respectively.

2. The salt flux density I at each time τ at the crystal–solution interface is given by:

$$I = b(C_s - C_{\text{sat}})(C_{s,s} - C_s) / C_{s,s},$$

where $C_{s,s}$ is the density of the solid salt, C_s is the instantaneous density of the salt in the cell bordering on that in which crystal growth is taking place, C_{sat} is the saturation concentration of the solution, and b is the kinetic coefficient of crystallization. The impurity flux density at the crystal–solution interface is calculated assuming that the impurity is completely expelled by the growing crystal. The bulk fluxes are calculated using the diffusion equation for the flux density in dilute solutions⁸ (for which the impurity diffusion coefficient D_p is introduced). It is assumed that the fluxes of the salt and the second component in the solution are unrelated.

3. When the salt concentration in the cell reaches $C_{s,s}$, the cell is colored and the next cell nuclei become the nearest neighbors to the cell. We shall assume that when the impurity being expelled reaches the concentration $C_{p,s}$, it is converted to a different phase, whereupon no fluxes can pass through the cell and it is impossible for salt to crystallize in the cell.

This model has five controlling parameters: the relative supersaturation $(C_{s,in} - C_{\text{sat}}) / C_{\text{sat}}$, the relative density $(C_{s,s} - C_{s,in}) / C_{s,s}$, the stability parameter bL / D_s , the relative impurity mobility D_s / D_p , and the relative impurity content $C_{p,in} / C_{p,s}$. On the basis of the aim stated in the introductory section, the first three parameters will have only the fixed values (0.9, 0.68, and 0.15, respectively), for which dendrites with tertiary branches are formed in the system according to the results presented in Ref. 8 (the values of the coefficients refer to NaCl salt). The fourth parameter is taken to be 19.5 (which corresponds to the ratio of the diffusion coefficients of NaCl and albumin protein).

The sequence of structures obtained during the growth of a dendrite in the presence of an increasing relative concentration of impurity is shown in Figs. 1a–1e. With increasing impurity content, the impurity converted to a different phase at first gradually fills the interbranch spaces, which negligibly influences the structure of the growing dendrite (see Fig. 1a). When the relative impurity content is in the region of 0.56, the action of the impurity leads to the formation of a

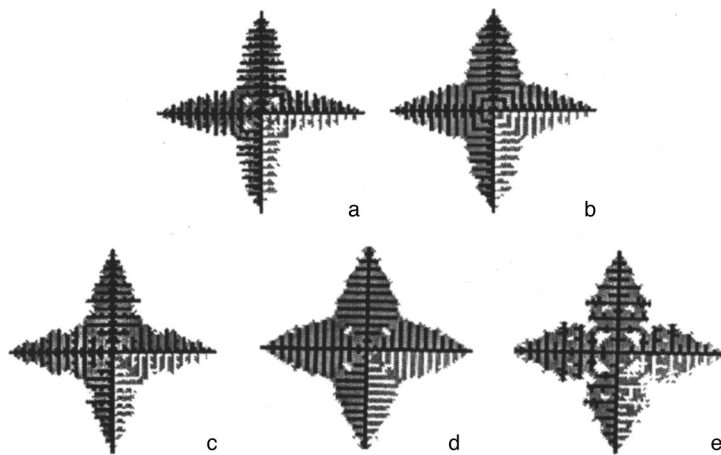


FIG. 1. Morphology of dendrite growth accompanying changes in the relative initial impurity content $C_{p, in} / C_{p, s}$: 0.53 (a), 0.56 (b), 0.59 (c), 0.64 (d), and 0.67 (e). The black shows the salt distribution and the gray shows the impurity transferred to a different phase. For convenience only the distribution of the impurity transferred to a different phase is shown in the bottom right quadrant.

dendrite predominantly with only secondary branches (see Fig. 1b). It was concluded from earlier studies,⁶ that the simplification of the structure initiated at this point should continue and the interbranch spaces should gradually increase. In this case, however, at relative impurity concentrations of 0.58–0.63, the dendrite acquires further branches including tertiary ones (see Fig. 1c). However, when the impurity content is 0.64, the dendrite morphology again reveals only secondary branches (see Fig. 1d). When further impurity is added, the dendrites again acquire further branches including tertiary ones (see Fig. 1e) and this is followed by a very rapid transition to underdeveloped crystal structures.

This cyclic repetition of structures can be attributed to the fairly strong nonequilibrium of the growth process in a phase-stratifying medium. The morphology of the growing structure is influenced by two interrelated parameters: supersaturation at the crystal–solution interface and localized obstacles to growth formed as a result of the nonuniform conversion of the impurity to a different phase (typical feedback). In fact, as the impurity concentration increases, the transition from the structure shown in Fig. 1a to that in Fig. 1b takes place as a result of phase stratification of the impurity near the growing secondary branches, which impedes diffusion and takes place almost simultaneously with the growth of these branches (the transition from a structure with tertiary branches to one with secondary branches in Figs. 1c and 1d can be explained similarly). The transition from the structure shown in Fig. 1b to that in Fig. 1c can be explained by the fact that the dendrite branches become thicker as a result of the earlier phase stratification of the impurity, and in these salt and impurity concentration fields, conditions are created for the formation of tertiary branches. The last transition (see Figs. 1d and 1e) initiated by a change in the impurity content in the system, is caused by an increase in the interbranch spacing and enlargement of the interbranch spaces during the growth process. As a consequence, the density of the crystal structure is reduced, conditions are established for freer movement of impurity from the growing crystal surface, and at the same time, the vicinity of the solution near the crystal becomes less depleted in salt. This leads to rapid branching of the dendrite with the formation of tertiary branches.

This cyclic change in morphology demonstrated by computer simulation has also been observed in various experiments. For instance, it was shown in Ref. 9 that the habit of ice crystals formed from vapor may undergo periodic repetition with changes in supercooling.

The results of our computer simulation suggest that cyclic changes in morphology take place in this system. It may be said that cyclic kinetic phase transitions take place in this highly nonequilibrium system. It is known^{1,2} that kinetic phase transitions are commonly described using the terminology and approaches developed in the physics of equilibrium phase transitions (such as the concept of the order parameter, Landau theory, and so forth). The phenomenon of reentrant phase transitions discovered for some organic substances forming a liquid crystal phase is familiar in the physics of liquid crystals.¹⁰ Reentrant transitions are characterized by a cyclic sequence of phases which gradually replace each other with continuously varying temperature. This effect has not been fully described in the specialist literature, although it can be qualitatively attributed to the presence of two interacting orientational and translational order parameters.¹¹ By using a qualitative analogy, we can describe the sequence of morphologies obtained in the present study with varying impurity content, as a kinetic reentrant transition. The quantitative changes in the structures are not very appreciable in these reentrant kinetic phase transitions (for instance, the fractal dimension of the structures changes very little, 1.61 ± 0.02 , see Fig. 1) although the symmetry of the morphotypes changes periodically, and this may correlate with the cyclic changes in symmetry accompanying the reentrant phase transition.

¹H. Haken, *Synergetics: An Introduction* (Springer-Verlag, Berlin, 1977) [Russ. transl. Mir, Moscow, 1980].

²P. Glansdorff and I. Prigogine, *Thermodynamic Theory of Structure, Stability and Fluctuations* (Wiley, New York, 1971) [Russ. transl. Mir, Moscow 1973].

³J. Feder, *Fractals* (Plenum Press, New York, 1988) [Russ. transl. Mir, Moscow, 1991].

⁴J. S. Langer, *Rev. Mod. Phys.* **52**, 1 (1980).

- ⁵P. K. Galenko and V. A. Zhuravlev, *Physics of Dendrites* (World Scientific, Singapore, 1994) [Russ. original, Soft-Moskva, Moscow, 1993]; R. Sasikumar and R. Sreenivasan, *Acta. Metall. Mater.* **42**, 2381 (1994); S. G. R. Brown, T. Williams, and J. A. Spittle, *Acta. Metall. Mater.* **42**, 2893 (1994); R. I. Mints, S. A. Skopinov, R. M. Kadushnikov, and D. Berg, *Zh. Fiz. Khim.* **66**, 352 (1992).
- ⁶L. M. Martyushev, V. D. Seleznev, and S. A. Skopinov, *Pis'ma Zh. Tekh. Fiz.* **22**(16), 12 (1996) [*Tech. Phys. Lett.* **22**, 648 (1996)].
- ⁷A. Sole, *Stagoskopie* (Franz Deuticke, Vienna, 1960).
- ⁸L. M. Martyushev, V. D. Seleznev, and S. A. Skopinov, *Pis'ma Zh. Tekh. Fiz.* **22**(4), 28 (1996) [*Tech. Phys. Lett.* **22**, 146 (1996)].
- ⁹B. J. Mason, *Contemp. Phys.* **33**, 227 (1992).
- ¹⁰P. E. Cladis, *Phys. Rev. Lett.* **35**, 48 (1975); P. E. Cladis, R. K. Bogardus, and D. Aadsen, *Phys. Rev. A* **18**, 2292 (1978).
- ¹¹P. E. Cladis, *Mol. Cryst. Liquid Cryst.* **67**, 177 (1981).

Translated by R. M. Durham

X-ray monitoring of the filling of cluster lattices in synthetic opals

V. V. Ratnikov

A. F. Ioffe Physicotechnical Institute, Russian Academy of Sciences, St. Petersburg

(Submitted December 15, 1996)

Pis'ma Zh. Tekh. Fiz. **23**, 7–10 (July 12, 1997)

It is proposed that the filling of cluster lattices in synthetic opals can be monitored by measurements of the absorption of x-rays. It is demonstrated that the degree of filling of the pores in the opals depends on the method of incorporating In, Te, and HgSe. © 1997 American Institute of Physics. [S1063-7850(97)00207-3]

Fairly perfect crystals of synthetic opals, comprising a system of close-packed spheres of amorphous SiO₂, 2000–2500 Å in diameter, have now been prepared. These large spheres may consist of smaller spheres (300–400 Å in diameter) which are made up of even smaller spheres, ~70 Å in diameter.¹ The octahedral and tetrahedral voids between the spheres together with their connecting channels form a so-called cluster lattice — a regular three-dimensional system of voids which, when filled with different materials, yield objects with interesting electronic and optical properties.^{2,3} The different subsystems of pores and channels in synthetic opals, their methods of filling, and the filler composition produce cluster lattices having a wide range of properties.

However, the structure of these new objects has not been studied in sufficient detail. The most important structural characteristics of opal lattices include the porosity and the degree of filling of the voids and channels by incorporated substances. The author has used measurements of the absorption of x-rays propagating through these objects to determine these parameters.

X-ray absorption porosimetry was performed using a standard x-ray source, and suitable collimation of the x-rays allowed the measurements to be made for a portion of the sample defined by the beam size.

The measurements were made using monochromatic CuK_{α1} radiation with a beam cross section of 0.05 × 1 mm. Particular attention was paid to the stability of the incident intensity *I*₀, for which the relative measurement error was ±0.1%. The relative error in the measurements of the transmitted intensity *I* depended on the sample thickness *t* and the type of substance filling the cluster lattice, and did not exceed ±5%. The error in the micrometer measurements of the sample thickness did not exceed ±0.2%. As a result, the relative measurement error for the density and the porosity did not exceed ±5.5%.

The porosity of the initial opals, *P*_{op}, required to determine the percent filling of the pores in the opal,

$$P_{x(\text{por})}(\%) = \frac{P_{x(\text{op})}}{P_{\text{op}}} \times 100, \quad (1)$$

was determined previously⁴ by x-ray absorption porosimetry and showed negligible difference between single-crystal (42.35%) and polycrystalline (42.50%) opals.

In formula (1)

$$P_{x(\text{op})}(\%) = \frac{\rho_x^{\text{ef}}}{\rho_x} \times 100 \quad (2)$$

gives the percent filling of the opal with substance *x*. Here, ρ_x (g/cm³) is the density of the filler substance and the effective densities ρ_x^{ef} (g/cm³) of the substances *x* = In, Te, or HgSe incorporated in the opal were obtained from measurements of the x-ray absorption by opals incorporating fillers:

$$\rho_x^{\text{ef}} = \frac{\ln(I_0/I) - (\mu/\rho)^{\text{aSiO}_2} \times \rho_{\text{op}}^{\text{ef}} \times t}{(\mu/\rho)_x \times t}. \quad (3)$$

Here *t* (cm) is the sample thickness, *I*₀ and *I* are the incident and transmitted x-ray intensities (counts/s), respectively, $(\mu/\rho)^{\text{aSiO}_2}$ (cm²/g) is the mass absorption coefficient of amorphous SiO₂, $\rho_{\text{op}}^{\text{ef}}$ (g/cm³) is the density of the initial opal, which is 1.28 g/cm³ according to the measurements made in Ref. 4, $(\mu/\rho)_x$ (g/cm³) is the x-ray mass absorption coefficient of a substance *x* having the density ρ_x (g/cm³) filling the pores in the opal. Values of $(\mu/\rho)^{\text{aSiO}_2} = 34.67$ cm²/g and $\rho^{\text{aSiO}_2} = 2.22$ g/cm³ were obtained by measuring the absorption of x-rays propagating through a fused (amorphous) quartz plate. The values of $(\mu/\rho)_x$ for *x* = In, Te, and HgSe and ρ_x for In and Te were taken from Ref. 5. Since the density of HgSe differs for the sphalerite and wurtzite phases, an x-ray diffraction pattern was obtained for opal containing HgSe. This revealed that the HgSe in the opal crystallizes in the form of a polycrystalline material with a sphalerite lattice. Thus, the value $\rho_{\text{HgSe}} = 8.26$ g/cm³ (Ref. 6) was used for the calculations.

The results of measurements of the degree of filling of the pores in opals with indium, tellurium, and mercury selenide are given in Table I. The filling was accomplished by immersing the opals in a solution of filler salts or by immersion in a melt (including under pressure).

It can be seen from Table I that the method of filling from a Te melt under pressure (sample No. 5) gives a degree of filling three times higher than immersing the opal in a solution of Te salts followed by reducing the salts to elemental Te (sample No. 4). The percent filling of the pores achieved by immersing the opal in a solution of In salts was higher: for sample No. 3, *P*_{In} = 23.87% of the entire pore volume was achieved. If the In content in this opal is taken relative only to the volume of the large pores (26% of the opal volume), their percent filling as reported here (38.82%) shows good agreement with the results of liquid porosimetry (40% as reported by D. A. Kurdyukov).

TABLE I. Effective density ρ_x^{ef} ($x = \text{In, Te, HgSe}$), degree of opal filling $P_{x(\text{op})}$, and filling of opal pores $P_{x(\text{por})}$.

Sample No.	$\rho_x^{\text{ef}}, \text{g/cm}^3$	$P_{x(\text{op})}, \%$	$P_{x(\text{por})}, \%$	Remarks
1. Opal+In	0.32	4.36	10.30	Filling from solution of In salts
3. Opal+In	0.74	10.10	23.87	As above
4. Opal+Te	0.15	2.38	5.60	From solution of Te salts
5. Opal+Te	0.47	7.58	17.83	At high pressure from melt
6. Opal+HgSe	0.83	10.08	23.70	From gas phase

Thus it is subsequently advisable to use combined measurements of the integrated porosity (x-rays) and the volume of the open pores (liquid porosimetry) to distinguish between the closed and open pores. The values of the integrated porosity obtained from optical measurements of the refractive index may be distorted by foreign substances adsorbed on the surface of the pores during synthesis of the opals, and by residual gases in closed pores.

It is also interesting to study the distribution profile of the incorporated substance over the thickness of the opal wafers. The initial sample No. 1 comprised a 2 mm thick wafer. Under the assumption that the In distribution profile is symmetric relative to $t = (1/2)t_{\text{op}}$, the sample was ground on one side to $(1/2)t_{\text{op}}$ and measurements of the transmitted x-ray intensity were made as the sample thickness was reduced from the outside in steps of several tens of micrometers. The linear dependence $\ln I \sim f(t)$ indicated that there was no In concentration gradient in the sample.

To sum up, x-ray porosimetry can be used to measure the degree of filling of cluster lattices in synthetic opals. Various fillers (In, Te, and HgSe) have been used to show

that the degree of filling of the pores depends on the method of filling, and it has been demonstrated that the filler distribution profile over the sample thickness can be determined.

The author would like to thank D. A. Kurdyukov for supplying the samples and L. M. Sorokin for useful discussions.

The work was supported by the Russian Fund for Fundamental Research (No. 96-02-16948a).

¹V. G. Balakirev, V. N. Bogomolov, V. V. Zhuravlev *et al.*, *Kristallografiya* **38**(3), 111 (1993) [*Crystallogr. Rep.* **38**, 348 (1993)].

²V. N. Bogomolov, S. A. Kitorov, D. A. Kurdyukov *et al.*, *JETP Lett.* **61**, 753 (1995)].

³V. N. Bogomolov, D. A. Kurdyukov, A. V. Prokof'ev *et al.*, *JETP Lett.* **63**, 520 (1996)].

⁴V. V. Ratnikov, *Fiz. Tverd. Tela* (St. Petersburg) **39**, (1997) [*Phys. Solid State* **39**, 1997] (in press).

⁵A. Guinier, *Théorie et Technique de la Radiocristallographie* (Dunod, Paris, 1956) [Russ. transl., Fizmatgiz, Moscow, 1961].

⁶H. Hamilton, *Semicond. Prod. Solid State Technol.* **7**(7), 15 (1954).

Translated by R. M. Durham

Investigation of implanted layers in silicon carbide by a modulation photoreflexion method

H. G. Walther, H. Karge, K. L. Muratkov, A. V. Suvorov, and I. O. Usov

Institut für Optik und Quantenelektronik, Friedrich-Schiller Universität, Jena, Germany;

Jena Wave Engineering and Consulting, Jena, Germany;

A. F. Ioffe Physicotechnical Institute, Russian Academy of Sciences, St. Petersburg;

Cree Research Inc., Durham, NC, 27713, USA

(Submitted March 4, 1997)

Pis'ma Zh. Tekh. Fiz. **23**, 11–20 (July 12, 1997)

The possibility of using a modulation photoreflexion method for diagnostics of ion-implanted layers in silicon carbide is considered. It is shown that the photoreflexion method can be used to determine the layer thickness and also the variation in the optical parameters of the layer as a function of the implanted ion dose. © 1997 American Institute of Physics.

[S1063-7850(97)00307-8]

Serious attention has recently been paid to studying the possibilities of using photothermal methods for diagnostics of semiconductor materials.¹ The most commonly used method for this purpose is a photoreflexion method^{1–4} capable of providing high sensitivity and good spatial resolution, and also of performing nondestructive measurements. The photoreflexion method has been successfully tried out on various materials such as Si (Refs. 4–11) and GaAs (Refs. 1, 12, and 13).

In addition, increasing attention has recently been paid to the applications and development of methods of diagnostics for wide-gap semiconductors,¹⁴ particularly silicon carbide. A characteristic feature observed when the photoreflexion method is used to study these semiconductors is the deep penetration of the pump and probe radiation into the material. This behavior is not typical of semiconductors such as Si and GaAs and occurs because the photon energies of the pump and probe lasers are substantially lower than the band gap. In this context, it is interesting to examine the characteristics of using the photoreflexion method for diagnostics of wide-gap semiconductors.

Here we examine the possibility of using the photoreflexion method for diagnostics of ion implantation processes in silicon carbide. We used a modified version of the photoreflexion method described in detail in Ref. 15, where the photoreflexion signal was excited and recorded at the same wavelength. The radiation source in this photoreflexion microscope was a semiconductor laser with a power of approximately 10 mW at 785 nm. The laser radiation was focused onto the surface of the object in a spot of around 2 μm . The modulation frequency of the radiation varied between 100 kHz and 12 MHz.

The experiments were carried out using 6H-SiC samples grown by the Lely method, implanted with 37 keV He⁺ ions. Samples implanted with three ion doses were studied: 10^{14} cm^{-2} , 10^{15} cm^{-2} , and $5 \times 10^{15} \text{ cm}^{-2}$. One of the samples contained a boundary between an unimplanted zone and a zone implanted with a dose of $5 \times 10^{15} \text{ cm}^{-2}$. The implantation of comparatively low-energy, light, He⁺ ions caused little change in the optical properties of the samples

and allowed a better assessment of the limiting capabilities of the method.

The results of an investigation of the photoreflexion signal as a function of the modulation frequency for silicon carbide samples implanted with different doses of He⁺ ions are plotted in Fig. 1. The measurements were made at fixed modulation frequencies, which were gradually increased from 94 kHz to 12 MHz. It can be seen from these results that the degree of implantation has a strong influence on the photoreflexion signal. A characteristic feature of using the photoreflexion method under these conditions is the highly nonmonotonic dependence of the signal on the implantation dose. For a silicon carbide sample with a dose of $5 \times 10^{15} \text{ cm}^{-2}$, the signal phase is shifted by 180° relative to samples with doses of 10^{14} cm^{-2} and 10^{15} cm^{-2} . This behavior of the photoreflexion signal for silicon carbide differs substantially from that of silicon and GaAs, for which the signal increases fairly monotonically with implantation dose.¹

For a more detailed study of the characteristics of formation of the photoreflexion signal in silicon carbide, we investigated its behavior on transition from the implanted to the unimplanted zone. Figure 2 gives results of measurements of the optical reflection coefficient, amplitude, and phase of the photoreflexion signal when the sample is swept perpendicular to the interface between these zones. Over the sweep, the depth of the implanted layer remains constant since the ion energy is fixed at 3 keV. At the same time, sections with doses ranging from $5 \times 10^{15} \text{ cm}^{-2}$ to completely unimplanted zones are sequentially passed through. This nonmonotonic behavior of the optical reflection coefficient during sweeping indicates that a thin optical layer is formed on the surface of the sample as a result of implantation. The position of the photoreflexion signal maximum does not coincide with the maximum of the optical reflection coefficient and is observed at a dose substantially lower than $5 \times 10^{15} \text{ cm}^{-2}$. Note also that, as can be seen from the data plotted in Fig. 2, the phase of the photoreflexion signals in the zone with an ion dose of $5 \times 10^{15} \text{ cm}^{-2}$ differs by 180° from the zones with doses of 10^{14} cm^{-2} and 10^{15} cm^{-2} . In

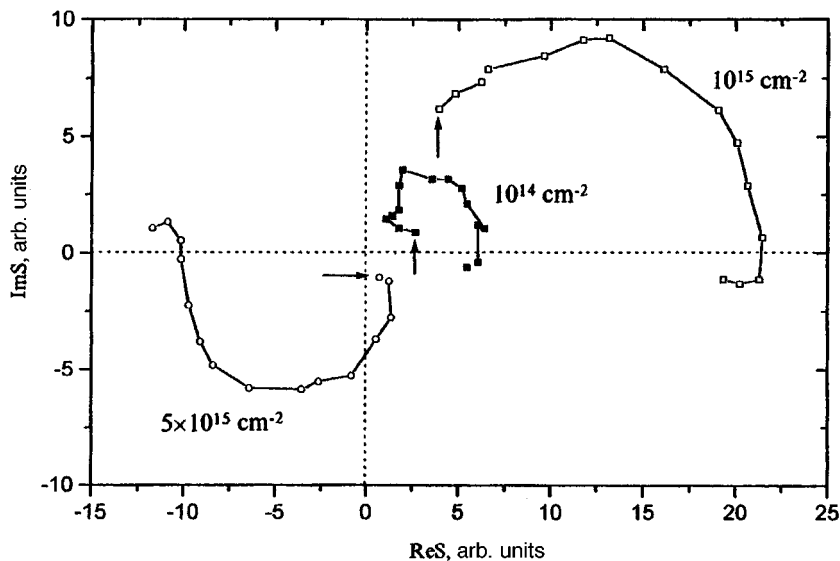


FIG. 1. Behavior of the real and imaginary parts of the photoreflection signal as functions of the modulation frequency for three silicon carbide samples implanted with 37 keV He⁺ ions. The measurements were made at frequencies of 0.094, 0.125, 0.200, 0.300, 0.500, 0.750, 1.00, 1.60, 2.50, 3.00, 4.00, 6.00, 8.00, 10.00, and 12.00 MHz. The arrows indicate the photoreflection signal corresponding to a frequency of 12 MHz.

addition, as can be seen from Fig. 2, the amplitude of the recorded photoreflection signal does not decrease to zero on crossing the boundary between the implanted and unimplanted zones, although a zone with a clearly defined reduction in signal amplitude is observed. There is no one position where the photoreflection signal vanishes during sweeping because the size of the laser radiation spot on the surface of the sample, 2 μm , was not sufficiently small.

We shall now briefly consider a model capable of explaining the main experimental results. In accordance with Refs. 1–4, the photoreflection signal may be generally expressed as

$$S = A \left(\frac{\partial R}{\partial T} \Delta T + \frac{\partial R}{\partial N} \Delta N \right), \quad (1)$$

where A is a proportionality factor, R is the coefficient of reflection from the object for the optical radiation intensity, ΔT are the fluctuations in the surface temperature of the sample, and ΔN is the change in the concentration of free carriers generated by the radiation.

Since the photon energy of the radiation used in the photoreflection experiments is less than the band gap of silicon carbide, no free carriers are generated directly by the light. Thus, the photoreflection signal in this case is only associated with the excitation of thermal waves in the object and is described by the first term in expression (1).

The optical and thermophysical properties of the implanted layer must be taken into account to determine the photoreflection signal from the implanted silicon carbide. It was shown in Ref. 16 that a three-layer optical model can be used to describe the characteristics of formation of the photoreflection signal over a wide range of implantation doses allowing for amorphization of the semiconductor material. One of these layers is used to describe the layer of amorphized material. In our case, the implantation of comparatively low-energy, light, He⁺ ions caused no amorphization of the material, so we used a single-layer model to model the optical properties of the implanted layer.

In accordance with the results of Ref. 17, the change in the refractive index of completely amorphized silicon carbide is approximately 30% of the value for the unimplanted material. Thus, at doses significantly lower than the amorphization threshold, it may be assumed that the changes in the real and imaginary parts of the permittivity caused by implantation are small compared with the permittivity of the unimplanted SiC. The concentration of defects induced in the semiconductor by implantation at doses below the amorphization threshold is approximated by a dependence proportional to the implanted ion dose.¹⁸ In the present case, it can therefore be assumed that the changes in the real and imaginary parts of the permittivity are also proportional to the implanted ion dose. Then, using the relation between the refractive index and the permittivity components, one can show that the changes in the refractive index and the absorption coefficient should also be linear functions of the dose.

Known methods of calculating the reflection of optical radiation from thin layers can be used to determine the coefficient of reflection from SiC with an implanted layer.¹⁹ For our particular case it should be assumed that the change in the refractive index at the interface between the implanted and unimplanted SiC is small, almost no 785 nm light is absorbed in the unimplanted SiC,²¹ and the condition $\alpha d \ll 1$ is satisfied (α is the coefficient of absorption of radiation in the implanted layer and d is the thickness of the implanted layer).

To determine the photoreflection signal as given by expression (1), we need to know the temperature fluctuations at the surface of the object, which should be calculated assuming that light is absorbed and thermal waves are excited predominantly in the implanted layer. For typical implanted layer thicknesses and thermal wavelengths in SiC up to frequencies of 1 MHz, we can assume that the generation of thermal waves is purely a surface process. Confining ourselves to this frequency range, we immediately obtain the final result for the photoreflection signal

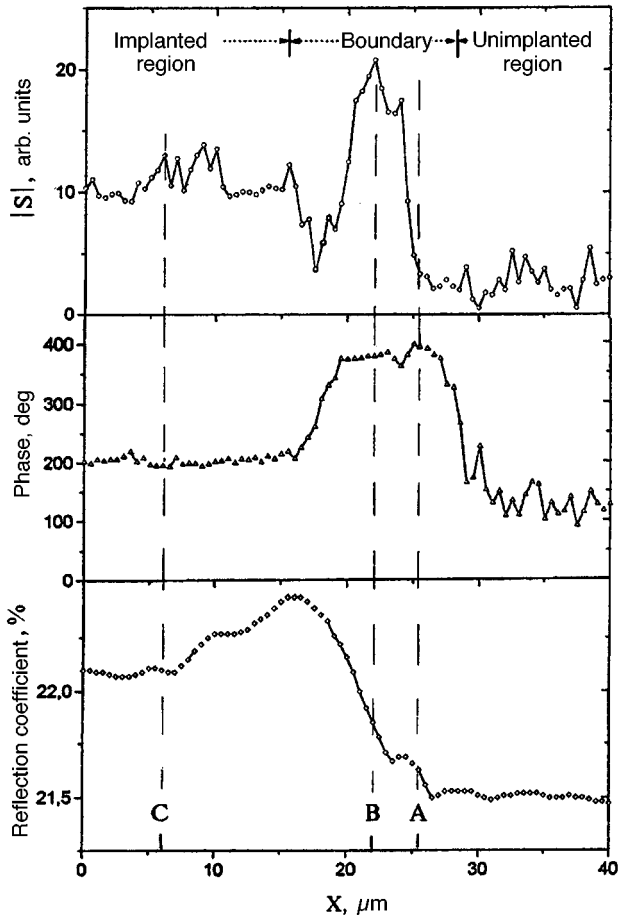


FIG. 2. Behavior of the photoreflection signal and the reflection coefficient when the interface between the implanted and unimplanted zones is swept. The implantation dose in the implanted zone was $5 \times 10^{15} \text{ cm}^{-2}$, the sweep step was $0.5 \mu\text{m}$, and the modulation frequency was 1 MHz. The letters A, B, and C refer to sections with implantation doses of 10^{14} , 10^{15} , and $5 \times 10^{15} \text{ cm}^{-2}$.

$$S = adA' \left\{ n_0 - 1 + \frac{1 + 3n_0 - 2n_0^2}{n_0(n_0 + 1)} \Delta n + \left[\alpha d(n_0 - 1) + 2 \frac{n_0 - 2}{n_0 + 1} \Delta n \right] \cos \frac{4\pi nd}{\lambda} + 2 \left[\frac{\alpha \lambda}{4\pi} \frac{1 + n_0 - n_0^2}{n_0(n_0 + 1)} + (n_0 - 1) \frac{2\pi d}{\lambda} \Delta n \right] \sin \frac{4\pi nd}{\lambda} \right\}, \quad (2)$$

where $A' = A (32I_0/qK) [n_0/(1+n_0)^5] (\partial n_0/\partial T)$, I_0 is the optical radiation intensity, $q = \sqrt{i\omega/k}$, $\omega = 2\pi f$, f is the modulation frequency, K and k are the thermal conductivity and the thermal diffusivity, respectively, n_0 is the refractive index of the unimplanted material, Δn is the change in the refractive index caused by implantation, and $(\partial n_0/\partial T)$ is the variation in the refractive index of silicon carbide with temperature.

Expression (2) can be used to determine the photoreflection signal for different implantation doses provided that the thickness of the implanted layer and the dose dependences of Δn and α are known. In accordance with the results of Ref. 18, we shall assume that for this particular case, the dependences of Δn and α on the He^+ ion implantation dose D are

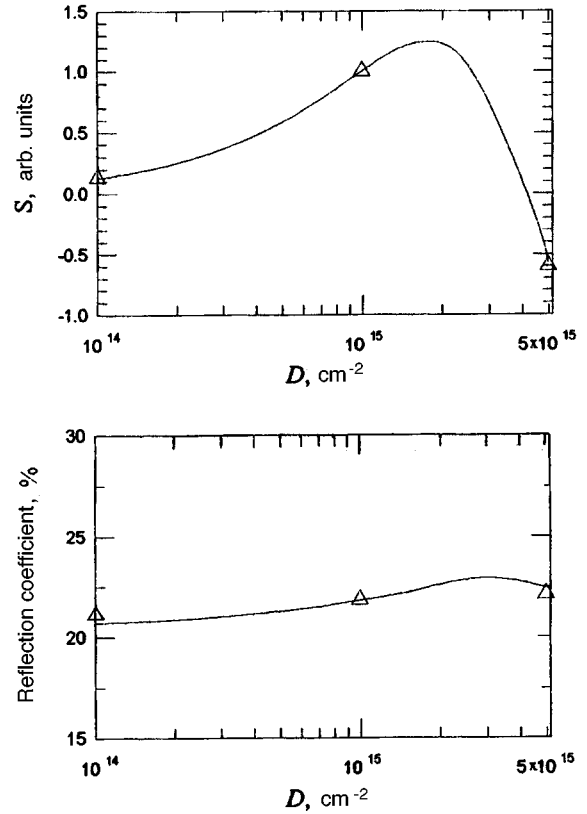


FIG. 3. Theoretical results of calculating the reflection coefficient and the photoreflection signal as a function of the implantation dose. The triangles give the experimental data.

described by the linear functions $\Delta n = \gamma_1 D$ and $\alpha = \gamma_2 D$ (γ_1 and γ_2 are proportionality factors). The refractive index n_0 for 6H-SiC at $\lambda = 785 \text{ nm}$ is between 2.61 and 2.64 (Ref. 21). Experimental data on the reflection coefficient and the photoreflection signal for various implantation doses may be used to determine the parameters of the implanted layer. Here, a similar problem was solved by simultaneously minimizing the rms error for the deviations between the theoretical and experimental data obtained for the reflection coefficient and the photoreflection signal. The results of these calculations are plotted in Fig. 3. When the refractive index of silicon carbide was taken as $n_0 = 2.64$, the following values were obtained for the other parameters: $\gamma_1 = 6.48 \times 10^{-17} \text{ cm}^{-2}$, $\gamma_2 = 1.10 \times 10^{-12} \text{ cm}$, and $d = 243 \text{ nm}$. On the basis of these data, the change in the refractive index at the maximum implantation dose of $5 \times 10^{15} \text{ cm}^{-2}$ is 12% of the value for the unimplanted material and the absorption coefficient is $6.5 \times 10^3 \text{ cm}^{-1}$. Thus these results indirectly support the assumption that silicon carbide does not undergo complete amorphization under these conditions. Then, in accordance with procedures developed to determine the parameters of implanted layers,²² the depth of the implanted layer for 37 keV He^+ ions is 220 nm. Hence the thickness of the implanted layer determined by the photoreflection method shows good agreement with the known value.

To sum up, these results have shown that the photoreflection method using incident radiation within the transpar-

ency band of the semiconductor can be used to determine not only the thickness of the implanted layer but also its optical characteristics. An important advantage of the photoreflexion method compared with the optical method is the significantly stronger dependence of the photoreflexion signal on the implantation dose. This factor can be utilized to improve substantially the accuracy of determining the optical and geometric parameters of implanted layers.

In conclusion, the authors would like to thank A. L. Glazov for assisting with the numerical calculations. One of the authors (K. L. Muratkov) would like to thank DAAD for the opportunity to carry out some of the work in Germany.

¹A. Rosencwaig, in *Photoacoustic and Thermal Wave Phenomena in Semiconductors*, edited by A. Mandelis (Elsevier, New York, 1987), pp. 97–135.
²J. Opsal, A. Rosencwaig, and D. L. Willenborg, *Appl. Opt.* **22**, 3169 (1983).
³A. Rosencwaig, J. Opsal, W. L. Smith, and D. L. Willenborg, *Appl. Phys. Lett.* **46**, 1013 (1985).
⁴J. Opsal and A. Rosencwaig, *Appl. Phys. Lett.* **47**, 498 (1985).
⁵T. Hara, H. Hagiwara, R. Ichikawa, S. Nakashima, K. Mizoguchi, W. L. Smith, C. Welles, S. K. Hahn, and L. Larson, *IEEE Electron. Dev. Lett.* **EDL-11**, 485 (1990).
⁶C. Christofides, I. A. Vitkin, and A. Mandelis, *J. Appl. Phys.* **67**, 2815 (1990).
⁷I. A. Vitkin, C. Christofides, and A. Mandelis, *J. Appl. Phys.* **67**, 2822 (1990).

⁸M. Nesteros, B. C. Forget, A. Christofides, and A. Seas, *Phys. Rev. B* **51**, 14 115 (1995).
⁹A. Seas and C. Christofides, *Appl. Phys. Lett.* **66**, 3346 (1995).
¹⁰B. C. Forget, I. Barbereau, D. Fournier, S. Tuli, and A. B. Battacharyya, *Appl. Phys. Lett.* **69**, 1107 (1996).
¹¹G. Benedetto, L. Boarino, and R. Spagnolo, *Phys. Status Solidi A* **146**, 777 (1994).
¹²T. Sawada, Y. Gohshi, T. Watanabe, and K. Furuga, *Jpn. J. Appl. Phys.* **24**, L938 (1985).
¹³N. Uchitomi, H. Mikami, N. Toyoda, and R. Nii, *Appl. Phys. Lett.* **52**, 30 (1988).
¹⁴G. Pensl and R. Helbig, *Adv. Solid State Phys.* **30**, 133 (1990).
¹⁵H. D. Geiler, H. Karge, and A. Kluge, *Surf. Sci. Coatings Technol.* **66**, 265 (1994).
¹⁶J. Opsal, *Photoacoustic and Photothermal Phenomena II*, Springer Series in Optical Sciences, Vol. 62 (Springer-Verlag, Berlin, 1990), pp. 140–145.
¹⁷E. Wendler, A. Heft, U. Zammit, E. Glaser, M. Marinelli, and W. Wesch, *Nucl. Instrum. Methods. Phys. Res. B* **116**, 398 (1996).
¹⁸V. S. Vavilov, *Effects of Radiation on Semiconductors* (Consultants Bureau, New York, 1965) [Russ. original, Fizmatgiz, Moscow, 1963].
¹⁹M. Born and E. Wolf, *Principles of Optics*, 4th ed. (Pergamon Press, Oxford, 1969) [Russ. transl. Nauka, Moscow, 1973].
²⁰G. Derst, C. Wilbertz, K. L. Bhatia, W. Krätschmer, and S. Kalbitzer, *Appl. Phys. Lett.* **54**, 1722 (1989).
²¹P. T. B. Shaffer, *Appl. Opt.* **10**, 1034 (1971).
²²J. P. Biersack and L. G. Haggmark, *Nucl. Instrum. Methods* **174**, 257 (1980).

Translated by R. M. Durham

Amorphous silicon and germanium films for uncooled microbolometers

T. A. Erukova, N. L. Ivanova, Yu. V. Kulikov, V. G. Malyarov, and I. A. Khrebtov

S. I. Vavilov State Optical Institute, All-Russian Science Center, St. Petersburg

(Submitted February 17, 1997)

Pis'ma Zh. Tekh. Fiz. **23**, 21–26 (July 12, 1997)

The possibility of using amorphous silicon and germanium films prepared by magnetron sputtering as components in uncooled microbolometers has been analyzed experimentally and results are presented. Amorphous silicon and germanium films having activation energies of 0.135 and 0.2 eV, and resistivities of 50 and 0.4 k Ω ·cm, respectively, were fabricated. © 1997 American Institute of Physics. [S1063-7850(97)00407-2]

Developments of uncooled multielement detectors, and particularly microbolometer arrays, have recently been at the forefront of infrared technology programs currently being undertaken.^{1–4} These arrays have a sensitivity in the 8–14 μm wavelength range close to that of cryogenic arrays and their lower cost and better operating characteristics means they have great potential.

One of the main problems involved in developing high-sensitivity, uncooled microbolometers for an infrared array is the fabrication of a thin-film heat-sensitive element having dimensions between 40×40 and $100 \times 100 \mu\text{m}$, a resistance of 5–30 k Ω , a low noise level, and a high temperature coefficient of resistance at room temperature (1–3%/K). In addition, the technology used to fabricate this component should be compatible with modern silicon microcircuit technology. Amorphous silicon and germanium films show promise in meeting these requirements.^{2,4}

The two most widely used types of structure for the sensing element of a microbolometer are planar (slit) and sandwich structures.^{1,2} In the former structure, a heat-sensitive film is placed in a planar gap between two sections of metallic film which function as electrodes, while in the latter structure, a heat-sensitive layer is formed between upper and lower thin-film electrodes. For the planar type of microbolometer the heat-sensitive film should have a resistivity ρ of the order of 1–10 Ω ·cm at room temperature. Films with $\rho = 5$ –50 k Ω ·cm are required for sandwich-structure microbolometers. Amorphous silicon and germanium (*a*-Si and *a*-Ge) films fabricated by magnetron sputtering were used in our investigation.

Films of *a*-Si $\sim 1 \mu\text{m}$ thick were prepared by sputtering a KÉF silicon target, having a resistivity of 60 Ω ·cm, using a planar dc magnetron in an argon atmosphere. Prior to each sputtering process, the vacuum chamber was evacuated to 7×10^{-7} Torr and the Ar working pressure was maintained by means of a sorption pump, which was evacuated together with the chamber before the sputtering process. Because of the lack of cooling, the substrate temperature could rise to 80–200 °C during the sputtering process (~ 1 h), depending on the discharge power. The films were deposited on pyroceramic substrates with deposited planar platinum electrodes and simultaneously on silicon wafers with an insulating SiO₂ layer. In the latter variant, removable copper-nickel masks were used to obtain eight $100 \times 100 \mu\text{m}$ sandwich

structures per sputtering process. The electrodes in these samples were titanium films.

The properties of the samples were assessed by measuring the temperature dependence of the resistance and the noise spectra. The temperature dependence of the resistance was measured at a direct current of 1–5 μA . The noise spectra were investigated in the frequency range between 10 Hz and 1 kHz using a low-noise preamplifier and an SK4-56 spectrum analyzer.

The properties of the heat-sensitive films depended on the Ar pressure and the discharge power. The magnetron source operated stably at pressures between 1×10^{-2} and 3×10^{-3} Torr. The resistivity of the deposited films varied between 10^9 and $10^6 \Omega$ ·cm. However, films with $\rho = 10^6 \Omega$ ·cm obtained at low pressures could peel off in air because of strong compressive internal stresses. The optimum pressure was found to be 1×10^{-2} Torr. Films with $\rho = 10^6 \Omega$ ·cm could be obtained by increasing the discharge current from 50 to 100–120 mA. Any further increase in the discharge current did not reduce the resistivity.

The resistance and the conduction activation energy E_t of the *a*-Si films also depend on the degree of doping of the target material.⁵ A KÉS silicon target with a resistivity of 0.02 Ω ·cm was used to achieve a further reduction in ρ . Films with $\rho = 90$ –50 k Ω ·cm and $E_t = 0.135$ eV (the temperature coefficient of resistance was 1.8%/K at 25 °C) were obtained with this target, in a planar electrode configuration which would be satisfactory for sandwich-structure microbolometers provided that the films possessed no anisotropic properties. However, the value of ρ for sandwich structures was an order of magnitude or more higher than that for planar structures obtained in a single sputtering process. The resistances of sandwich samples in the same batch differed by a factor of 10–20 at a measuring current of $\sim 1 \mu\text{A}$ and depended on the magnitude and direction of the current.

Figure 1 shows the temperature dependence of the resistance for one of the sandwiches (sample No. 4–1) for different directions of the $\sim 2 \mu\text{A}$ measuring current. For one direction we find $E_t = 0.295$ eV and for the other, $E_t = 0.051$ eV (the temperature coefficient of resistance at 25 °C is 3.8 and 0.7%/K, respectively). We postulate that this effect may occur because of the influence of asymmetric situation with the Ti-TiO-Si barrier contacts on one side, and Si-SiO-Ti contacts on the other side of the sandwich structure. This

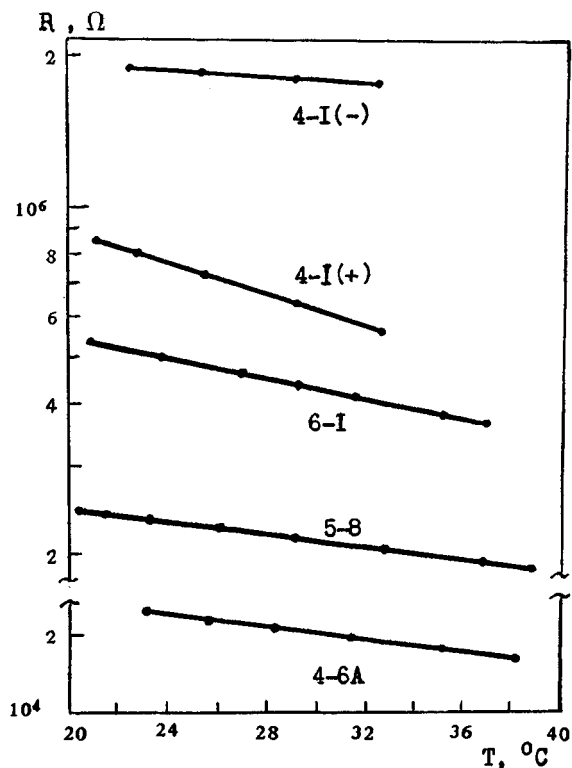


FIG. 1. Temperature dependence of the resistance of *a*-Si and *a*-Ge (Sample No. 6-1) film samples. Sample Nos. 4-1, 5-8, and 4-6A have a sandwich configuration with an area of 0.01, 0.01, and 0.9 mm², respectively; sample No. 6-1 has a planar configuration and an 8 mm² working area of heat-sensitive film. The (+) and (-) signs indicate the different directions of the measuring current.

supposition was confirmed by measurements of the current-voltage characteristics of the structures.

In sandwich sample No. 4-6A (Fig. 1), having an area of 0.9 mm², we used a Wood's metal electrode instead of the upper deposited Ti electrode. The activation energy of this sample (0.13 eV) was close to E_t for a planar sample but the room-temperature resistance was 20 k Ω higher than that calculated using ρ for a planar sample, although it remained almost the same when the direction of the measuring current was reversed. This behavior also supported the assumption of asymmetric barrier effects. It is significant that foreign researchers who observed similar effects, used single-chamber sputtering of sandwich structures without breaking vacuum.² The noise spectra of sample No. 4-6A at different currents are shown in Fig. 2. The noise is clearly of current origin and depends on frequency as $1/f^{1.1}$. At these currents the measured noise voltage was two orders of magnitude greater than the thermal noise voltage of the resistance and was caused, in our opinion, by the non-Ohmic property of the contacts.

In order to reduce the influence of oxides at the metal-semiconductor interface, the substrate and the Ti electrode were lightly etched in an Ar glow discharge plasma before deposition of the *a*-Si film. The surface of the *a*-Si film was also cleaned in Ar (sample No. 5-8, Fig. 1) in another apparatus before depositing the upper Ti electrode. The resistances of this batch of samples differed by no more than a

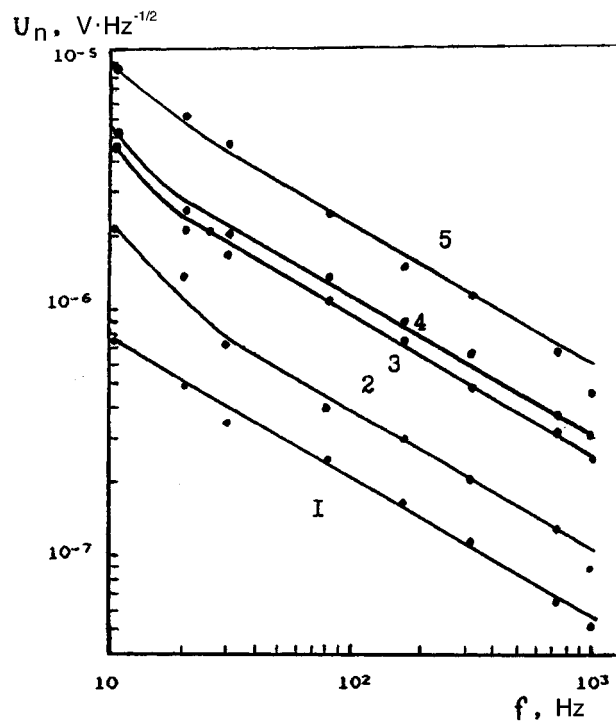


FIG. 2. Noise voltage spectra of sample No. 4-6A at different currents: 1 — 1.1 μ A, 2 — 2.2 μ A, 3 — 4.4 μ A, 4 — 6.7 μ A, and 5 — 11.1 μ A.

factor of 2.5 and the activation energy was $E_t=0.12$ eV, i.e., almost the same as for sample No. 4-6A. The change in the resistance when the direction of the current was reversed was 5-9%.

The composition of the residual atmosphere in the vacuum chamber and the purity of the argon must be carefully monitored to obtain amorphous silicon films of lower resistivity, down to 10 $\Omega \cdot$ cm, under our experimental conditions. If hydrogen, oxygen, and water vapor are present in the chamber, these gases may passivate broken bonds in the amorphous silicon, resulting in the deposition of a film of amorphous hydrogenated silicon, a material with different electrical and optical properties.⁶

When germanium is used as the sputtered target, the same values of E_t can be achieved as for silicon, but with a lower resistivity and noise level.⁴ This was confirmed by the results of sputtering a single-crystal GMO-grade germanium target with a resistivity of 50 $\Omega \cdot$ cm under the same conditions as those used to obtain *a*-Si films. The films were deposited on a pyroceramic substrate with a planar electrode configuration. For $\rho=4 \times 10^2$ $\Omega \cdot$ cm, this sample (No. 6-1) had an activation energy $E_t=0.2$ eV. The resistivity of the *a*-Ge film only differed from that of the target by a factor of eight (for silicon this difference was four orders of magnitude). This indicates that Ge is less sensitive to residual gases than silicon. In addition, for germanium hydrogen passivation of broken bonds is desirable to obtain the optimum resistivity. For example, it was shown in Ref. 7 that films of amorphous hydrogenated germanium obtained by adding 10% H₂ to Ar, have resistivities ρ up to 10⁵ $\Omega \cdot$ cm and $E_t=0.42$ eV. Another promising technique is to obtain *a*-Si_xGe_{1-x} films by combined sputtering of silicon and ger-

manium. By altering the ratio of Si and Ge in the sputtered target, films with a wide range of ρ and E_t combinations can be obtained.

To sum up, magnetron sputtering has been used to obtain a -Si and a -Ge films having a temperature coefficient of resistance between 1.6 and 2.6%/K at 25°, which is consistent with that of microbolometers in uncooled arrays developed by foreign researchers.¹⁻⁴ The required resistivity and activation energy are easier to achieve for a -Ge films than for a -Si films. The technology used to obtain low-noise Ohmic contacts between these heat-sensitive films and electrodes requires further development.

- ¹R. A. Wood and N. A. Foss, *Laser Focus World*, **29**(6), 101 (1993).
- ²M. H. Unewisse, B. I. Craig, R. J. Watson, and K. C. Liddiard, *Proc. SPIE* **2254**, 43 (1995).
- ³C. Marshall, N. Butler, R. Blackwell, R. Murphy, and T. Breen, *Proc. SPIE* **2746**, 23 (1996).
- ⁴M. H. Unewisse, K. C. Liddiard *et al.*, *Proc. SPIE* **2552**, 77 (1995).
- ⁵W. T. Pawlewicz, *J. Appl. Phys.* **49**, 5595 (1978).
- ⁶N. L. Ivanova, V. V. Nikitin, and A. P. Onokhov, *Opt. Zh. No. 7*, 45 (1993).
- ⁷Nguyen Van Dong and Tran Quoc Hai, *Phys. Status Solidi B* **88**, 355 (1978).

Translated by R. M. Durham

Low-temperature radiation-stimulated gettering of impurities and defects in silicon by layers of porous silicon

A. V. Kulikov, V. A. Perevoshchikov, V. D. Skupov, and V. G. Shengurov

Physicotechnical Scientific-Research Institute at the N. I. Lobachevskii State University, Nizhniĭ Novgorod
(Submitted February 18, 1997)

Opticheskiĭ Zhurnal **23**, 27–31 (July 12, 1997)

Experimental results are presented for the low-temperature gettering of impurities and defects in semiconductor silicon wafers by layers of porous silicon followed by argon ion irradiation.

It is shown that the gettering effect is caused by the simplest mobile point defects (vacancies) and elastic waves. © 1997 American Institute of Physics. [S1063-7850(97)00507-7]

It has been established¹ that layers of porous silicon effectively getter impurities and cluster-type defects from single-crystal silicon substrates when these structures undergo high-temperature annealing in a gaseous medium or vacuum. In addition, the results of layer-by-layer mass-spectrometric analysis of porous silicon–single-crystal-silicon structures presented in Ref. 2 indicate that impurities are gettered, albeit weakly, at room temperature during the electrochemical formation of porous silicon layers and subsequent holding of the samples under normal conditions. Our aim in this study was to investigate the possibilities for enhancement of low-temperature gettering by irradiating layers of porous silicon with moderate-energy ions.

We investigated structures formed by anodic treatment of KDB-0.005 (111) silicon crystals in a HF:H₂O:C₂H₅OH = 1:1:2 solution (parts by volume) at an anode current density of 10 mA·cm⁻². Layers of porous silicon, 1, 3, and 10 μm thick, with a porosity of ~35%, were formed. The structures were then irradiated on the porous silicon side by 40 and 100 keV argon ions to a dose of 1×10¹⁶ cm⁻². After irradiation, the porous silicon was placed in a 15% KOH solution and on the side of the substrates in contact with the porous silicon we made layer-by-layer measurements of the surface electrical resistivity at temperatures of 77–375 K, and of the microdefect density using patterns of chemical selective etching in an HF (48%):H₂O 1:2 (parts by volume) solution.

The experiments showed that as a result of the anodic treatment and subsequent irradiation of the porous silicon with Ar⁺ ions the surface resistivity of the single-crystal substrate is reduced near the interface with the porous silicon, and these changes are more clearly defined, the greater the thickness of the porous silicon and the higher the energy of the implanted ions (Fig. 1). At the same time that the surface-averaged resistivity decreases, the variance of R_s also decreases: after anodic treatment and etching of the porous silicon, the variance decreased by 9–10%, and after irradiation and removal of the porous silicon, it decreased by 25–30%. This indicates enhanced uniformity of the distribution of the impurity–defect components in the surface layer of the single crystal. The temperature dependences of the surface resistivity of the unirradiated and irradiated porous-silicon–single-crystal-silicon structures did not reveal any characteristic features distinguishing them from those of the initial substrates, within measurement error. This may indi-

cate that first, the anodization and subsequent ion irradiation of the porous silicon does not appreciably alter the energy level spectrum in the band gap typical of the initial silicon and second, the reduction in the surface resistivity is mainly caused by increased carrier mobility as a result of a decrease in the total concentration of scattering centers in the single crystal near the interface with the porous silicon. The depth to which the change in the surface resistivity after anodic etching and irradiation can be traced by layer-by-layer etching of the silicon substrates increases as the thickness of the porous silicon and the ion energy increase. Table I gives the depths at which the electrical resistivity agrees with R_s for the initial silicon substrates within a ±3% confidence interval (with a 0.95 confidence), i.e., the effective gettering depth.

The results of a layer-by-layer determination of the microdefect density in the surface zone, revealed in the patterns of selective chemical etching in the form of flat-bottomed etch pits, correlate with the electrical measurement data. By way of illustration, Fig. 2 gives the microdefect density as a function of the etched layer depth for structures with a po-

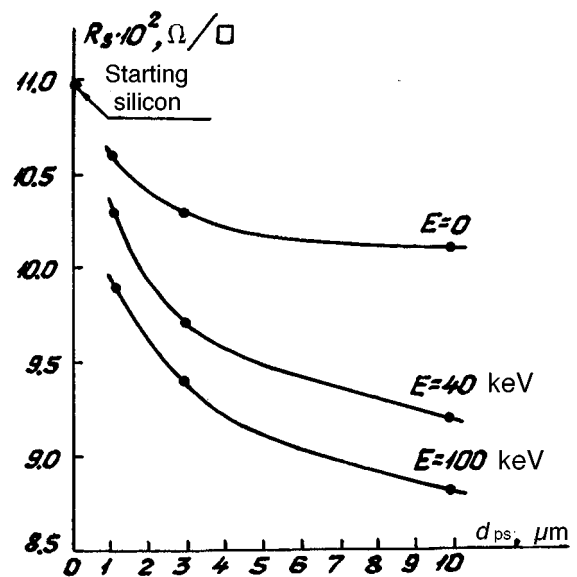


FIG. 1. Change in the surface resistivity of a single-crystal substrate after argon ion irradiation of porous silicon layers of varying thickness with a dose of 1×10¹⁶ cm⁻².

TABLE I. Effective gettering depth in porous-silicon–single-crystal-silicon structures for various argon ion energies.

Thickness of porous silicon, μm	Irradiation ion energy, keV	Gettering depth, μm
1	0	4–6
1	40	8–10
1	100	16–18
3	0	8–10
3	40	13–15
3	100	18–20
10	0	17–20
10	40	22–24
10	100	25–28

porous silicon layer 10 μm thick. As the thickness of the porous silicon decreases, the region of reduced microdefect density approaches the interface between the porous silicon and the single-crystal silicon.

These results may be explained using concepts of low-temperature gettering of impurities and defects in the single-crystal silicon by layers of porous silicon, whereby fluxes of nonequilibrium intrinsic point defects, predominantly vacancies, are injected into the surface zone of the substrate during the electrochemical formation and subsequent ion irradiation of the porous silicon.^{2,3} These point defects are formed at the stage of local dissolution of the silicon near micropores during the anodic treatment, during the subsequent active, low-temperature oxidation of the porous silicon in air,¹ and under irradiation. The ion irradiation intensifies the relaxation processes taking place in the thermodynamically nonequilibrium porous-silicon–single-crystal-silicon system, such as redistribution of impurities and dissolution of microdefects after anodization and during oxidation. Since the thickness of the porous silicon layers in these structures is much greater than the argon ion path (with allowance for the lower density of the porous silicon, the path of 100 keV ions is

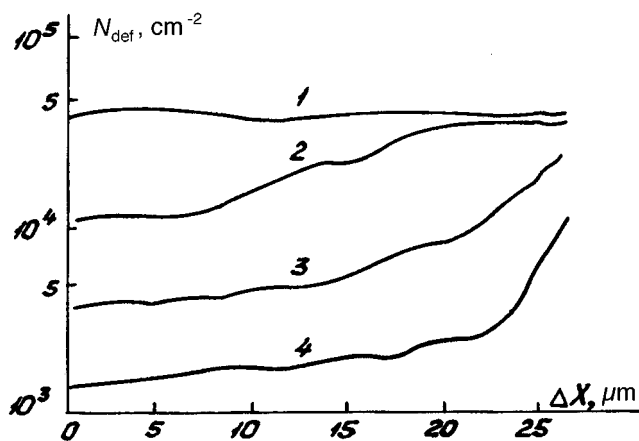


FIG. 2. Density of microdefects versus distance from porous-silicon–single-crystal-silicon interface for initial crystals (1), after the formation of porous silicon (2), and after irradiation of the porous silicon with 40 keV (3) and 100 keV (4) argon ions.

$0.43 \pm 0.04 \mu\text{m}$), it is assumed that the observed enhanced gettering is caused by the simplest mobile point defects and elastic waves generated in the ion stopping zone, which is localized in the porous silicon.⁴ Further research is planned to identify specific laws governing the influence of the anodizing and irradiation conditions on the efficiency of radiation-stimulated gettering by porous silicon layers.

¹V. A. Labunov, V. P. Bondarenko, and V. E. Borisenko, *Zarub. Élektron. Tekh.* No. 15, 3 (1978).

²V. A. Perevoshchikov, V. D. Skupov, and V. G. Shengurov, *Élektron. Tekh. Ser. 7*, 1(182), 10.

³V. A. Perevoshchikov and V. D. Skupov, *Characteristic Features of the Abrasive and Chemical Treatment of Semiconductor Surfaces* [in Russian], Nizhniĭ Novgorod State University Press, Nizhniĭ Novgorod, (1992).

⁴P. V. Pavlov, Yu. A. Semin, V. D. Skupov, and D. I. Tetel'baum, *Fiz. Khim. Obrab. Mater.* No. 6, 53 (1991).

Translated by R. M. Durham

Intensity and phase of reflected radiation in a vanadium dioxide structure with surface plasmons

V. F. Nazvanov and D. I. Kovalenko

Saratov State University

(Submitted February 20, 1997)

Pis'ma Zh. Tekh. Fiz. **23**, 32–36 (July 12, 1997)

Results of theoretical calculations are presented for the angular dependences of the reflection coefficient and phase of reflected p -polarized radiation at wavelengths of 6328 Å and 11 500 Å in vanadium dioxide layered structures with surface plasmons. Results of calculations are presented for the two phases of the vanadium dioxide films — semiconducting and metallic.

© 1997 American Institute of Physics. [S1063-7850(97)00607-1]

Vanadium dioxide, VO_2 , exhibits a first-order semiconductor–metal phase transition at a critical temperature of around 68 °C, which is accompanied by rearrangement of the crystal structure and changes in the electrical and optical properties,^{1–3} and which allows this material to be used in electronics and optoelectronics. In particular, VO_2 films are widely used in optoelectronics for modulation of visible, infrared, and millimeter radiation, in robot eye devices, coherent information processing systems, holography, and other devices.^{3–17} All these applications rely not so much on the values *per se* of the optical constants of the VO_2 films as on changes in them accompanying a phase transition near the critical temperature, which for VO_2 films can be reduced to 47 °C by means of suitable technology.¹¹ The data obtained in Ref. 11 led the authors to conclude that the modulation of 6328 Å radiation by a VO_2 film is predominantly phase modulation, whereas at 11 500 Å the contributions of the amplitude and phase components become comparable.

Here we report the first results of theoretical calculations of the behavior of the amplitude reflection coefficient and the phase of reflected p -polarized radiation in a layered structure formed by vanadium oxide films with surface plasmons using Kretschmann's scheme,¹⁸ as a function of the angle of incidence of the radiation for two wavelengths, 6328 and 11 500 Å.

As in Ref. 19, we used a matrix method for the calculations and we investigated glass (prism)–gold-layer– VO_2 film structures. For the calculations at 6328 Å, the refractive indices (dielectric constants) of the glass and the gold (410 Å thick) were taken to be $n = 1.52$ and $\epsilon = -12.4 + i \cdot 1.43$, respectively. The optical coefficients for the VO_2 films at these wavelengths were obtained from Ref. 10. The thickness of the VO_2 films in these structures was taken to be infinite.

The results of the calculations are plotted in Figs. 1 and 2. Figure 1a gives the amplitude reflection coefficient R of 6328 Å radiation as a function of the angle of incidence θ for a structure with a VO_2 film at two temperatures: 20 °C (semiconducting VO_2 phase) and 80 °C (metallic phase). Figure 1b gives the corresponding results of calculations of the phase of the reflected radiation for the same parameters. It can be seen from Figs. 1a and 1b that the changes in $R(\theta)$ are greater than the changes in the phase $\varphi(\theta)$.

Figures 2a and 2b give the angular dependences of the amplitude reflection coefficient and the phase of 11 500 Å reflected radiation at the same temperatures: 20 and 80 °C. It

can be seen from the data plotted in Fig. 2 that the VO_2 phase transition is accompanied by a substantial change in the angular dependences $R(\theta)$ and $\varphi(\theta)$, where the changes in $R(\theta)$ and $\varphi(\theta)$ are comparable.

To sum up, we have reported the first results of theoretical calculations of the angular dependences of the amplitude reflection coefficient and phase of reflected radiation at two wavelengths, 6328 and 11 500 Å, in layered structures with surface plasmons, and consisting of two phases of vanadium dioxide films — semiconducting and metallic. The results

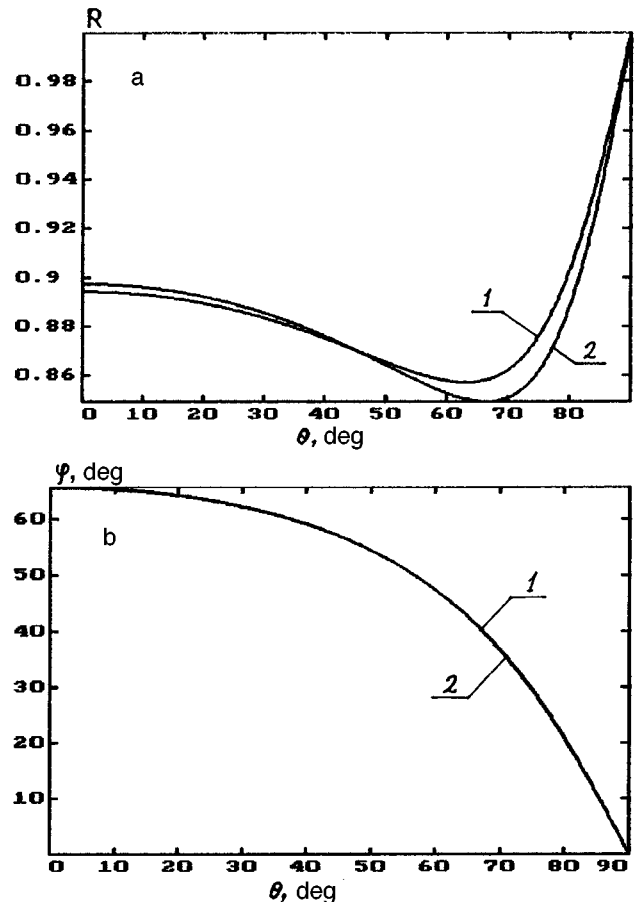


FIG. 1. a — Energy reflection coefficient versus angle of incidence ($\lambda = 6328$ Å). The curves are plotted for different temperatures: 1 — 20 °C, 2 — 80 °C; b — phase shift between the p - and s -polarized components of the reflected radiation versus angle of incidence ($\lambda = 6328$ Å). The curves are plotted for different temperatures: 1 — 20 °C, 2 — 80 °C.

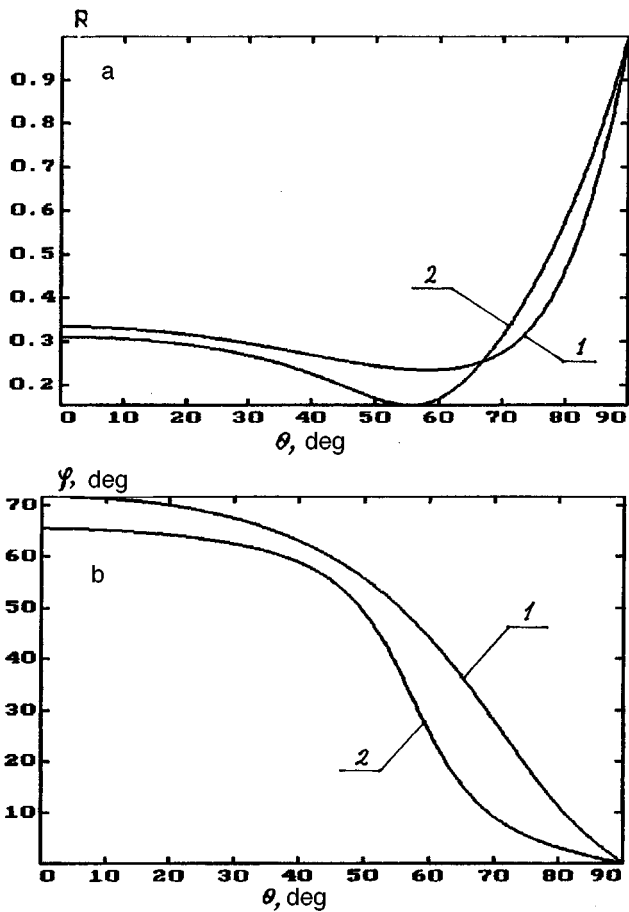


FIG. 2. a — Energy reflection coefficient versus angle of incidence ($\lambda = 11500 \text{ \AA}$). The curves are plotted for different temperatures: 1 — 20 °C, 2 — 80 °C; b — phase shift between the p - and s -polarized components of the reflected radiation versus angle of incidence ($\lambda = 11500 \text{ \AA}$). The curves are plotted for different temperatures: 1 — 20 °C, 2 — 80 °C.

may be useful for the development of optical radiation modulators, temperature gauges, and other devices utilizing VO_2 films with surface plasmons.

- ¹F. J. Morin, *Phys. Rev. Lett.* **3**, 34 (1959).
- ²J. B. Goodenough, *J. Solid State Chem.* **3**, 490 (1971).
- ³A. A. Bugaev, B. P. Zakharchenya, and F. A. Chudnovskii, *Metal-Semiconductor Phase Transition and Its Applications* [in Russian], (Nauka, Moscow 1979).
- ⁴B. S. Borisov, S. T. Koretskaya, V. G. Mokerov, A. V. Rakov, and S. G. Solov'eva, *Fiz. Tverd. Tela (Leningrad)* **12**, 2209 (1970) [*Sov. Phys. Solid State* **12**, 1763 (1970)].
- ⁵F. A. Chudnovskii, *Zh. Tekh. Fiz.* **45**, 1561 (1975) [*Sov. Phys. Tech. Phys.* **20**, 999 (1975)].
- ⁶Yu. M. Gerbshtein, T. V. Smirnova, E. I. Terukov, and F. A. Chudnovskii, *Fiz. Tverd. Tela (Leningrad)* **18**, 503 (1976) [*Sov. Phys. Solid State* **18**, 290 (1976)].
- ⁷M. E. Guchukova, A. G. Zhdan, and M. I. Elinson, *Mikroelektronika* **5**, 558 (1976).
- ⁸D. I. Bilenko, O. A. Belobrovaja, E. A. Zharkov *et al.*, *Fiz. Tverd. Tela (Leningrad)* **18**, 503 (1976) [*Sov. Phys. Solid State* **18**, 1153 (1976)].
- ⁹L. A. Beresneva, L. L. Vasil'eva, S. F. Devyatova *et al.*, *Pis'ma Zh. Tekh. Fiz.* **3**, 420 (1977) [*Sov. Tech. Phys. Lett.* **3**, 170 (1977)].
- ¹⁰A. A. Gur'yanov, I. A. Khakhaev, and F. A. Chudnovskii, *Zh. Tekh. Fiz.* **61**(10), 76 (1991) [*Sov. Phys. Tech. Phys.* **36**, 1120 (1991)].
- ¹¹F. C. Case, *J. Vac. Sci. Technol. A* **5**, 1762 (1987).
- ¹²S.-J. Jiang, C.-B. Ye, S. R. Kan, and C.-G. Granqvist, *Appl. Opt.* **30**, 847 (1991).
- ¹³F. C. Case, *Appl. Opt.* **30**, 4119 (1991).
- ¹⁴F. A. Egorov, Yu. Sh. Temirov, A. A. Sokolovskii *et al.*, *Pis'ma Zh. Tekh. Fiz.* **17**(22), 85 (1991) [*Sov. Tech. Phys. Lett.* **17** 817 (1981)].
- ¹⁵H. Jerominek, F. Picard, and D. Vincent, *Opt. Eng.* **32**, 2092 (1993).
- ¹⁶I. Lujan, *Proc. SPIE* **715**, 82 (1987); **940**, 160 (1988).
- ¹⁷O. B. Danilov, O. P. Konovalova, A. N. Sidorov, and N. N. Shaganov, *Prib. Tekh. Eksp.* No. 4, 121 (1995).
- ¹⁸E. Kretchman, *Z. Physik.* **241**, 313 (1971).
- ¹⁹V. F. Nazvanov and D. I. Kovalenko, *Pis'ma Zh. Tekh. Fiz.* **21**(14), 60 (1995) [*Tech. Phys. Lett.* **21**, 565 (1995)].

Translated by R. M. Durham

Influence of the ionizing and displacing components of proton irradiation on structural changes in boron nitride

V. A. Stepanov and P. A. Stepanov

State Scientific Center of the Russian Federation, Institute of Energy Physics, Obninsk
(Submitted February 4, 1997)

Pis'ma Zh. Tekh. Fiz. **23**, 37–41 (July 12, 1997)

Raman spectroscopy has been used to study structural changes in pyrolytic boron nitride irradiated by 7 MeV protons. It is shown that the ionizing component of the proton irradiation effectively reduces the number of grain boundaries while the displacing component induces the formation of stacking faults in the boron nitride structure. © 1997 American Institute of Physics. [S1063-7850(97)00707-6]

The influence of the ionizing and displacing components of radiation on structural changes in solids is an important topic in solid-state radiation physics. The mechanisms for this influence, particularly for ceramic insulators, have not yet been studied. The different components of the radiation can be separated experimentally when materials are irradiated with high-energy particles. In this case, the displacing component is observed predominantly at the end of the particle tracks in the materials while most of the track section is characteristic of the ionizing component. In this investigation Raman spectroscopy is used to make a structural analysis of areas of proton-irradiated pyrolytic boron nitride corresponding to different sections of the ion tracks.

A stack of eight thin (60 μm) samples were irradiated by protons (energy 7 MeV, intensity $2.5 \times 10^{12} \text{ cm}^{-2} \text{ s}^{-1}$, dose $5.2 \times 10^{15} \text{ cm}^{-2}$) whose projected in boron nitride is $\sim 350 \mu\text{m}$. For each sample, measurements were made of the Raman line profile of the high-frequency E_{2g} vibrations.¹ Raman spectra of samples from the irradiated stack are shown in Fig. 1. It can be seen that while the position of the maximum remains the same (1365–1367 cm^{-1}), the Raman line width gradually decreases with increasing sample number (distance along the tracks) and then increases substantially at sample 6 (at a distance of 300–360 μm). A comparison with calculations made using the Kinchin–Pease model (TRIM-90 program) allows us to relate the ionizing and damaging components of the proton irradiation to the Raman line width (Fig. 2). As the ionizing component increases, the Raman line width decreases. The region of maximum damaging action and hydrogen accumulation corresponds to a broad Raman line (the calculated proton range was 356.5 μm with a variance of 6.2 μm). A decrease in the line width compared with the initial value is also observed for deeper regions which were exposed to the ionizing action of the gamma bremsstrahlung.

When interpreting these results, it must be borne in mind that pyrolytic boron nitride is a nanocrystalline material with a specific structural hierarchy.² Aggregates of up to 2000 nm consist of ~ 100 nm grains, which in turn consist of slightly misoriented crystals of 30–60 nm. The large number of intergranular and intercrystallite boundaries have an appreciable influence on the Raman line profile which, in boron nitride materials, is determined by a set of frequencies shifted relative to the fundamental vibrational frequency.¹

The shifts of the fundamental frequency are caused either by damping of vibrations at the surface of the crystals, or by local vibrations at boundaries associated with impurities (hydrogen, halogen ions), or they are caused by changes in the force constants of the atomic bonds at boundaries. For $\lambda/2$ damping at the surface, the complex frequency of the atomic vibrations in the surface zone is expressed in terms of the fundamental vibration frequency ω_0 (Ref. 3):

$$\omega = i\lambda/2 + \omega_0 - a\lambda^2/\omega_0, \quad (1)$$

where a is a numerical coefficient (~ 1). A shift of the vibration frequencies by $\Delta\omega \sim 10 \text{ cm}^{-1}$ in boron nitride is observed for $\lambda = 100 \text{ cm}^{-1}$. In the presence of local vibrations at the frequency ω_s which differs from the natural frequency

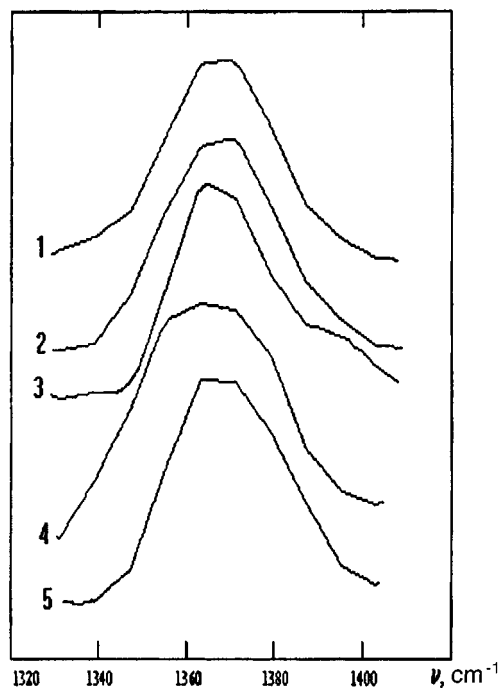


FIG. 1. Raman spectra of boron nitride samples from proton-irradiated stack. 1 — sample No. 1 (0–60 μm section of track), 2 — sample No. 3 (120–180 μm), 3 — sample No. 5 (240–300 μm), 4 — sample No. 6 (300–360 μm), and 5 — sample No. 7.

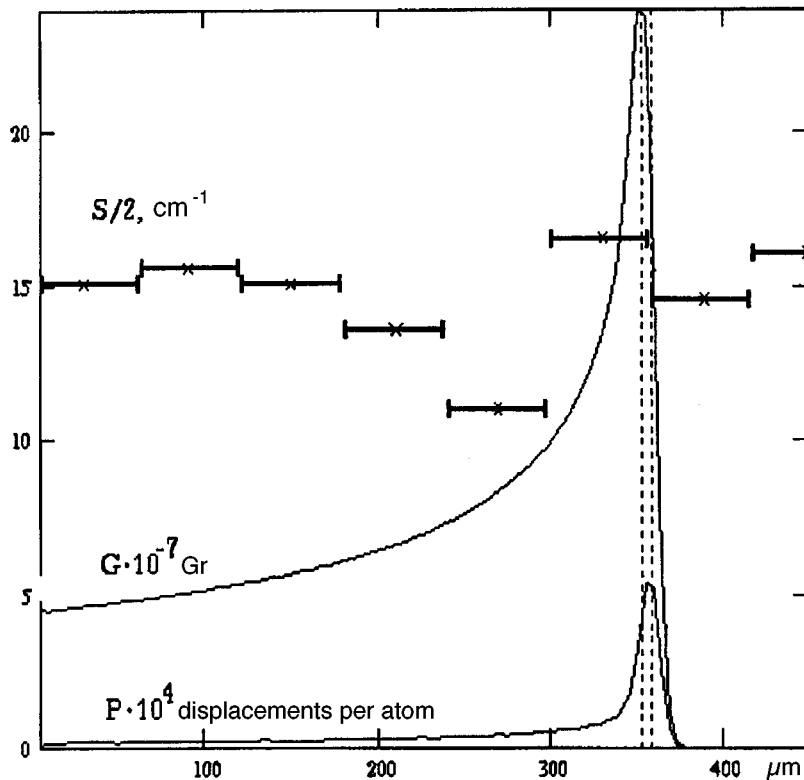


FIG. 2. Half-width of Raman scattering peak ($S/2$) versus proton range compared with calculated curves of ionization losses (G) and atomic displacements (P). The dashed curve indicates the hydrogen saturation region.

ω_0 , the decrease in the amplitude of the atomic vibrations at the frequency ω_s with increasing atomic number n is described by:⁴

$$s_n = s_0 \left\{ \frac{1 - \varepsilon}{1 + \varepsilon} \right\}^n, \quad (2)$$

where $1 - \varepsilon = (\omega_0 / \omega_s)^2$. Assuming that the broadening of the Raman line to 25 cm^{-1} is caused by a spectrum of local vibrations at the surface of the crystallites, we find that a shift of the natural vibration frequencies takes place at distances of up to 5 nm from the surface of boron nitride crystallites. For crystallite sizes of 30–60 nm, up to 30% of the atoms have vibration frequencies differing from ω_0 .

A decrease in the Raman line width is associated with a decrease in the fraction of atoms having shifted vibration frequencies or with a decrease in the number of boundaries in the material. A reduction in the number of boundaries under ionizing irradiation may be caused by free carrier relaxation processes of radiation origin at the boundaries. As a result of a release of energy at crystallite boundaries, chemical bonds with impurities may be broken and partial recrystallization may occur.

As the fraction of the displacing component in the irradiation increases, the Raman line is broadened considerably (Fig. 2). This broadening is caused by radiation defects and hydrogen impurities accumulating in the bulk of the crystallites and along the grain boundaries. The asymmetric broadening of the Raman line in the low-frequency range (spectrum 4 in Fig. 1) indicates that stacking faults are formed in the hexagonal structure of the boron nitride.¹

The authors would like to thank B. N. Sharupin for kindly supplying the boron nitride samples and L. M. Kryukova for discussions of the results.

¹ V. A. Stepanov and P. A. Stepanov, *Opt. Spektrosk.* **78**, 431 (1995) [*Opt. Spectrosc. J.* **78**, 387 (1995)].

² V. S. Dedkov, Yu. F. Ivanov, V. V. Lopatin, and B. N. Sharupin, *Kristallografiya* **38**(2), 217 (1993) [*Crystallogr. Rep.* **38**, 248 (1993)].

³ S. Ya. Vetrov and V. F. Shabanov, *Vibrational Spectroscopy of Disproportionate Crystals* [in Russian] (Nauka, Novosibirsk, 1991).

⁴ O. Madelung, *Festkörpertheorie III. Lokalisierte Zustände* (Springer-Verlag, Berlin, 1973).

Translated by R. M. Durham

Determination of the average size and concentration of air bubbles in water by nuclear magnetic resonance

B. G. Emets

Kharkov State University

(Submitted February 13, 1997)

Pis'ma Zh. Tekh. Fiz. **23**, 42–45 (July 12, 1997)

Nuclear magnetic resonance has been used to determine the mean radius of air bubbles in distilled water that has stood for a long time and the volume concentration of these “reduced to mean radius” bubbles. It is shown that the kinetics of the change in the concentration of these bubbles can be observed from the change in the spin-spin relaxation time. © 1997 *American Institute of Physics*. [S1063-7850(97)00807-0]

For many applications in liquid-state physics, such as determining the tensile strength of a liquid, it is important to know the size and volume concentration of stable gas bubbles contained in the liquid. In the literature dealing with distilled water that has stood for a long time there are discrepancies in the estimates of these parameters. In Ref. 1, for instance, the author reports the observation of bubbles having radii of 10^{-7} – 10^{-3} cm with a volume concentration of bubbles of all sizes of 10^6 – 10^7 cm $^{-3}$. The authors of Ref. 2 obtained 3×10^{-5} cm for the maximum stable gas bubble radius in water, while the authors of Ref. 3 observed ultrasmall bubbles of 1.8×10^{-7} cm radius with a concentration of 10^{11} cm $^{-3}$. The aim of this investigation was to determine the mean radius of air bubbles in water and the volume concentration of these “reduced to mean radius” bubbles.

A pulsed nuclear magnetic resonance (NMR) method was used to measure the spin-lattice and spin-spin nuclear magnetic relaxation times, T_1 and T_2 (Ref. 4). This technique uses the fact that the time T_2 for the nuclei of liquids, measured by the Carr-Purcell method,⁵ depends on the sizes of inclusions if any are present in the liquid. This procedure gives the spin echo amplitude at time t :

$$h(t) = h(0) \exp(-t/T_2) \exp(-1/3 \gamma^2 \Gamma^2 D \tau^2 t). \quad (1)$$

Here γ is the gyromagnetic ratio of the resonant nucleus, Γ is the magnetic field gradient, D is the diffusion coefficient of the liquid molecules containing resonant nuclei, τ is the time interval between the 90° and 180° pulses, and $h(0)$ is the amplitude of the echo signal at “zero” time. Usually, knowing the nonuniformity (Γ) of the field of their NMR relaxometer magnet and the diffusion coefficient of the sample molecules, experimentalists select a small interval τ such that the diffusion term in Eq. (1) may be neglected. The authors of Ref. 6 followed this procedure and from the results of their measurements, they derived empirical formulas linearly relating the rates of relaxation of the water protons, T_1^{-1} and T_2^{-1} , to the number N of oxygen molecules dissolved per cm 3 of water:

$$\begin{aligned} T_1^{-1}(N) &= 0.284 + \tilde{T}_1^{-1}(N) = 0.284 + 4.65 \times 10^{-19} \cdot N, \\ T_2^{-1}(N) &= 0.455 + \tilde{T}_2^{-1}(N) = 0.455 + 5.25 \times 10^{-19} \cdot N. \end{aligned} \quad (2)$$

The results described by the formulas (2) were confirmed in the experiments carried out by the author. The degree of increase in the relaxation rates is determined by the increase in the concentration of paramagnetic centers dissolved in the water, such as oxygen molecules.

It follows from the theory of nuclear magnetic relaxation^{4,7-9} that the second terms in the formulas (2), $\tilde{T}_1^{-1}(N)$ and $\tilde{T}_2^{-1}(N)$, caused by the presence of dissolved paramagnetic centers, should be the same, but in these formulas (2), they are dissimilar. This disparity may be explained by the fact that the authors of Ref. 6, having measured T_2 by the Carr-Purcell technique, neglected the presence of air microbubbles in the water, near whose surfaces a substantial magnetic field gradient exists

$$\bar{\Gamma} \approx \pi H_0 (\chi_{v,s} - \chi_{v,m}) \cdot 1/\bar{R}. \quad (3)$$

(Here H_0 is the external magnetic field strength, $\chi_{v,s}$ is the volume magnetic susceptibility of air, $\chi_{v,m}$ is the volume magnetic susceptibility of water, and \bar{R} is the mean radius of the bubbles. Expression (3) is the result of solving the Poisson equation $H = \nabla \phi$ for the scalar potential ϕ when analyzing the field distribution for a sphere in a medium situated in the field H_0 (Ref. 10)).

In this situation the diffusion term in Eq. (1) cannot be neglected since the gradient $\bar{\Gamma}$ may be fairly large. For example, in the present case ($H_0 = 6.58 \times 10^3$ G, $\chi_{v,s} = 3 \times 10^{-8}$, and $\chi_{v,m} = -7.2 \times 10^{-7}$), at the surface of a bubble of radius 10^{-4} cm the gradient is $\bar{\Gamma} = 149$ G·cm $^{-1}$. The need to allow for the diffusion term in measurements of T_2 by the Carr-Purcell method in liquids containing small ($\bar{R} = 10^{-3}$ cm) glass spheres was convincingly demonstrated in Ref. 11. According to Eq. (1), water molecules diffusing in the gradient $\bar{\Gamma}$ undergo rapid relaxation, which leads to this severe reduction in the observed time T_2 relative to the time T_1 , which is completely insensitive to the magnetic field gradient.

When these facts are taken into account, the contribution to the total rate of spin-spin relaxation caused by the presence of dissolved paramagnetic centers in the water is given by:

$$\tilde{T}_2^{-1}(N) = \tilde{T}_1^{-1}(N) \times (1 - \alpha) + 1/3 \gamma^2 \bar{\Gamma}^2 D \tau^2 \alpha. \quad (4)$$

Here α is the fraction of the time spent by each proton in the layer of water directly in contact with the surface of each bubble (in the zone of the gradient $\bar{\Gamma}$) and $(1-\alpha)$ is the fraction of the time spent by each proton in contact with the paramagnetic centers (oxygen molecules), whose concentration is N . (In the absence of any bubbles, α should be set to zero and then $\bar{T}_1^{-1}(N) = \bar{T}_2^{-1}(N)$, i.e., the above requirement of relaxation theory that the paramagnetic centers dissolved in the water should make the same contributions to the rates $T_1^{-1}(N)$ and $T_2^{-1}(N)$ is satisfied).

Assuming that the thickness of the water layer in contact with the surface of a bubble is equal to the diameter of a water molecule, $\delta = 1.54 \times 10^{-8}$ cm, and introducing the volume concentration ν of bubbles of ‘‘averaged’’ radius \bar{R} , we obtain $\alpha = 4\pi\bar{R}^2\delta\nu$. Substituting α into formula (4) indicates that the change in the concentration ν may be monitored continuously by measuring $\bar{T}_2^{-1}(N)$ in the sample (since $\bar{\Gamma} \sim 1/\bar{R}$). Substituting into formula (4) the values of $\bar{T}_1^{-1}(N)$ and $\bar{T}_2^{-1}(N)$ from the empirical formulas (2) for the concentration N corresponding to the solubility of oxygen in water at 25 °C (Ref. 12) and $\bar{\Gamma}$ from Eq. (3), and also assuming that the measurements were made for water protons ($\gamma = 2.68 \times 10^4$ rad·s⁻¹·G⁻¹ and $D = 2.5 \times 10^{-5}$ cm²·s⁻¹)

for $\tau = 2 \times 10^{-3}$ s, we obtain $\bar{R} = (1.8 \pm 0.2) \times 10^{-5}$ cm and $\nu = (9 \pm 1) \times 10^9$ cm⁻³ $\approx 10^{10}$ cm⁻³.

- ¹L. R. Gavrilov, *Content of Free Gas in Liquids and Methods of Measurement*, in *Physical Principles of Ultrasound Technology*, edited by L. D. Rosenberg [in Russian] (Nauka, Moscow, 1970), pp. 395–426.
- ²V. K. Makarov and N. V. Chulkova, *Akust. Zh.* **35**, 175 (1989) [*Sov. Phys. Acoust.* **35**, 108 (1989)].
- ³N. F. Bunkin, A. V. Lobelev, O. I. Vinogradova, T. G. Movchan, and A. I. Kuklin, *JETP Lett.* **62**, 685 (1995).
- ⁴A. Abragam, *The Principles of Nuclear Magnetism* (Clarendon Press, Oxford, 1961) [Russ. transl. IL, Moscow, 1963].
- ⁵H. J. Carr and E. M. Purcell, *Phys. Rev.* **94**, 630 (1954).
- ⁶R. Hausser and F. Noak, *Z. Naturforsch. A* **20**, 1668 (1965).
- ⁷A. Carrington and A. D. McLachlan, *Introduction to Magnetic Resonance with Application to Chemistry and Chemical Physics* (Harper & Row, New York, 1967) [Russ. transl. Mir, Moscow, 1970].
- ⁸A. A. Vashman and I. S. Pronin, *Nuclear Magnetic Relaxation Spectroscopy* [in Russian] (Énergoatomizdat, Moscow, 1986).
- ⁹V. I. Chizhik, *Nuclear Magnetic Relaxation* [in Russian] (Leningrad State University Press, Leningrad, 1991).
- ¹⁰I. E. Tamm, *Principles of the Theory of Electricity* [in Russian] (Nauka, Moscow, 1976), or D. Menzel, *Fundamental Formulas of Physics* (Prentice-Hall, New York, 1955), p. 315.
- ¹¹J. A. Glasel and K. H. Lee, *J. Am. Chem. Soc.* **96**, 970 (1974).
- ¹²G. W. C. Kaye and T. H. Laby, *Tables of Physical and Chemical Constants and Some Mathematical Functions*, 16th ed. (Longman, New York, 1959) [Russ. transl. of earlier ed., Fizmatgiz, Moscow, 1962].

Translated by R. M. Durham

Integrated-optics detectors with recording of the reflection coefficient in a prism excitation system

I. U. Primak, A. B. Sotskiĭ, and A. V. Khomchenko

Institute of Applied Optics, Belarus Academy of Sciences, Mogilev

(Submitted July 24, 1996)

Pis'ma Zh. Tekh. Fiz. **23**, 46–51 (July 12, 1997)

Detectors whose operating principle is based on recording the energy reflection coefficient in a prism waveguide excitation system are proposed for measuring physical quantities. The possibilities of maximizing the sensitivity of these devices is determined. An experimental investigation was made of a detector for the ammonia concentration in the atmosphere. © 1997 American Institute of Physics. [S1063-7850(97)00907-5]

A considerable number of detectors to measure the physical parameters of media based on planar optical waveguides have now been proposed.^{1,2} The operating principle of these detectors is usually based on recording the angles of resonant excitation of the modes. However, the changes in these angles accompanying external influences on the waveguide are extremely small, so that the analysis of the measurement results presents some difficulties. In addition, these angles are only related to the real parts of the mode propagation constants and do not provide any information about the imaginary parts, which are also subject to variation under external influences.

Here we propose detectors which record the integrated intensity of a light beam reflected by a prism coupling system at a fixed angle of incidence. The intensity depends on the variations of the real and imaginary parts of the mode propagation constant. These detectors provide appreciable differential amplification of the effects of external influences and have a convenient rugged construction for measurement purposes. Aspects of maximizing the detector sensitivity are analyzed and a detector for atmospheric ammonia was investigated experimentally.

The apparatus is shown schematically in Fig. 1. We assume that the waveguide is excited by a beam whose field at the base of the prism is given by $\psi = \psi_0(x/W, z\sin(\alpha)/W)\exp(-i\beta_0 z)$, where ψ is the component of the E_x field for the TE modes or the H_x field for the TM modes, W is a scale factor characterizing the beam dimensions, α is the angle between the beam axis and the base of the prism, $\beta_0 = k_0 \cos(\alpha)(\epsilon_p)^{0.5}$, $k_0 = 2\pi/\lambda_0$ is the wave number in vacuum, and ϵ_p is the relative permittivity of the prism. Then using the results of Ref. 3 we can derive the following expression for the energy coefficient of reflection of the beam from the base of the prism:

$$R = 1 - 4p_2(1 + p_2p_1^{-1})\text{Re}(f), \quad (1)$$

$$f = N^{-1} \int_{-\infty}^{\infty} d\xi \int_{-\infty}^{\infty} d\zeta \psi_0^*(\xi, \zeta) \int_{-\infty}^{\xi} \psi_0(\xi, \zeta')$$

$$\times \exp[t(\zeta' - \zeta)] d\zeta',$$

$$t = ip_3 - p_1, \quad p_1 = m \text{Im } \bar{h},$$

$$p_2 = 2\delta |\Delta h| m(1 + \delta^2)^{-1},$$

$$p_3 = m(\text{Re } \bar{h} - \beta_0), \quad m = W(\sin(\alpha))^{-1},$$

$$\delta = k_{yg}(k_{yp})^{-1} [\epsilon_p \epsilon_g^{-1}]^\rho,$$

$$\Delta h = \bar{h} - h = - \frac{\exp(-2k_{yg}g)(1 + i\delta)k_{yg}}{(1 - i\delta)\text{Re } h}$$

$$\times \left[\int_{-\infty}^{\infty} Y^2(\epsilon_g(\text{Re } \epsilon_w)^{-1})^\rho dy \right]^{-1},$$

$$k_{yg,p} = \sqrt{(\text{Re } h)^2 - k_0^2 \epsilon_{g,p}},$$

$$N = \int_{-\infty}^{\infty} d\xi \int_{-\infty}^{\infty} d\zeta |\psi_0(\xi, \zeta)|^2.$$

Here h is the propagation constant of the excited mode, \bar{h} is the propagation constant of the outgoing mode of the waveguide–prism structure, ϵ_g and ϵ_w are the permittivities of the buffer layer and the waveguide, $Y(y)$ is the distribution of the mode field, $\rho = 1$ for TM modes and $\rho = 0$ for TE modes. The value of R depends on three dimensionless parameters p_1 , p_2 , and p_3 , which may vary under external influences. However, under the usual conditions $k_0 m \gg 1$, $\exp(-2k_{yg}g) \ll 1$, and the variations δp_2 are negligible compared with the variations δp_1 and δp_3 caused by the increments $\delta(\text{Re } h)$ and $\delta(\text{Im } h)$. With allowance for this factor, formula (1) yields the following expressions to determine the corresponding reflection coefficient increment

$$\delta R = \delta S F, \quad F = (p_1 + p_2) \left(\frac{\partial R}{\partial p_1} + D \frac{\partial R}{\partial p_3} \right). \quad (2)$$

We initially assume that the values of $\delta S = \delta(\text{Im } h)/\text{Im } h$ and $D = \delta(\text{Re } h)/\delta(\text{Im } h)$, characterizing the waveguide, are fixed. Then, maximizing the detector sensitivity reduces to searching for the maximum of the function $|F(p_1, p_2, p_3)|$, which is equivalent to determining the optimum beam width W , the optimum detuning of the angle α from the resonant value $\alpha_r = \arccos[\text{Re } \bar{h}(k_0^2 \epsilon_p)^{-0.5}]$, and the optimum buffer layer thickness g . To search for the extrema of F , it is convenient to cast the variables in the form $u = p_2/p_1$, $v = p_3/p_1$, and $H = 1/p_1$. We assume that $\psi_0^* = \psi_0 \exp(i\varphi)$, where φ is a constant (the beam is focused at the base of the prism). Then for $H \rightarrow 0$ we can obtain the asymptotic expansion

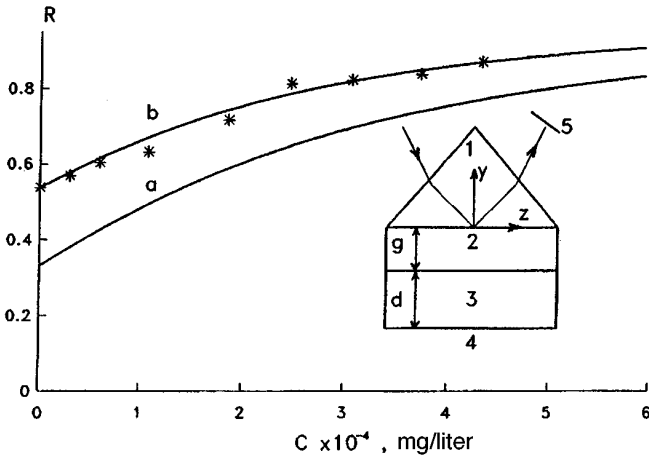


FIG. 1. Reflection coefficient versus ammonia concentration and schematic diagram of detector: 1 — prism, 2, 3 — buffer layer and waveguide of thickness g and d , respectively, 4 — substrate, and 5 — photodetector.

$$F = F_0 + \frac{4H^2 u(u+1)}{N} \left[\text{Im} \left(\frac{3D(u+1)}{(1-iv)^4} \right) + \text{Re} \left(\frac{4u+3-ivu}{(1-iv)^4} \right) \right] \int_{-\infty}^{\infty} d\xi \int_{-\infty}^{\infty} d\zeta \left| \frac{\partial \psi_0}{\partial \zeta} \right|^2 + O(H^3),$$

$$F_0 = 4u(u+1)(1+v^2)^{-2} [v^2 - 2u - 1 - 2Dv(u+1)],$$

from which it follows that the extremum F_0 of the function F is attained at $H=0$, i.e., in the plane-wave limit. The solution of the system $\partial F_0 / \partial u = 0$, $\partial F_0 / \partial v = 0$ is given by

$$u = -\frac{3F_0}{9F_0+2}, \quad v = \frac{2D}{9F_0+2}, \quad F_0 = \pm \frac{2}{3} \sqrt{\frac{D^2+1}{3}}. \quad (3)$$

From this it follows that there are two optimum sets of parameters u and v , which give equivalent sensitivity of the detector.

We investigated the deviations of the solution of the optimized problem from the limiting solution obtained for real bounded beams. Figure 2 gives results of numerical calculations of the extrema of the function F , and also of the corresponding parameters u and v as a function of the parameter H for the excitation of the waveguide by a Gaussian beam [$\psi_0(\xi, \zeta) = \exp(-\xi^2 - \zeta^2)$]. It can be seen that almost

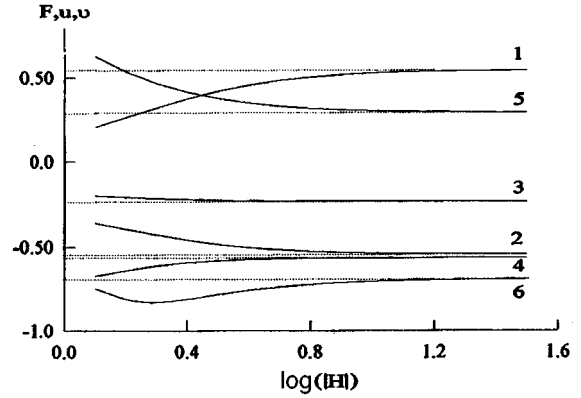


FIG. 2. Extreme values of F (curves 1 and 2) and optimum values of u (3, 4) and v (5, 6) as functions of H for $D=1$. Curves 3 and 5 correspond to curve 1 and curves 4 and 6 correspond to curve 2. The dashed curves give the limiting solutions (3).

complete agreement is achieved between these curves and the limiting solutions (3) for $|H| < 0.2$.

We now discuss some aspects relating to the choice of waveguide films. First we note that, in accordance with Eq. (2), the sensitivity of the detector increases monotonically with decreasing mode losses. However, the results obtained above indicate that the overall dimensions of the detector must also increase. We subsequently analyze TE-polarized modes (the results for the TM modes are basically similar) and confine ourselves to detectors for impurity components in liquids or gases located in the region $y < -g-d$ (Fig. 1). Either porous or solid waveguide films may be used in these detectors.¹ In the first case, the presence of impurities induces a change in the complex permittivity of the film ϵ_w . In the second case, the detector either records a change in the complex permittivity ϵ_s of the region $y < -g-d$ or the presence of a layer of molecules of thickness Δ and permittivity ϵ_a deposited on the film. The values of δS and D can be determined by analyzing the differential equation describing the mode field. From this it follows that the relations $D = \delta(\text{Re } \epsilon_w) / \delta(\text{Im } \epsilon_w)$ and $\delta S = \delta(\text{Im } \epsilon_w) / \text{Im } \epsilon_w$ are satisfied for the variations of ϵ_w , i.e., the sensitivity of the detector does not depend on the thickness of the deposited layer but is determined by its composition. For the variations of ϵ_s we have $D = \delta(\text{Re } \epsilon_s) / \delta(\text{Im } \epsilon_s)$,

$$\delta S = \frac{\delta(\text{Im } \epsilon_s)(\epsilon'_w - \epsilon'_g)[k_0^2 \epsilon'_w - (\text{Re } h)^2]}{k_{ys}[k_0^2 d(\epsilon'_w - \epsilon'_g)(\epsilon'_w - \epsilon'_s) + k_{yg}(\epsilon'_w - \epsilon'_s) + k_{ys}(\epsilon'_w - \epsilon'_g)] \text{Im } \epsilon_w}, \quad (4)$$

where $k_{ys} = \sqrt{(\text{Re } h)^2 - \epsilon'_s k_0^2}$ and $\epsilon'_{s,w} = \text{Re}(\epsilon_{s,w})$. For the case of practical importance where an adsorbed layer of thickness $\Delta \ll k_0^{-1}$ and low absorption ($d \rightarrow \infty$) is formed, expression (2), with allowance for Eq. (3), yields

$$\delta R = \frac{\pm 4(\epsilon_a - \epsilon'_s)(\epsilon'_w - \epsilon'_g)[k_0^2 \epsilon'_w - (\text{Re } h)^2] \Delta}{3\sqrt{3}[k_0^2 d(\epsilon'_w - \epsilon'_g)(\epsilon'_w - \epsilon'_s) + k_{yg}(\epsilon'_w - \epsilon'_s) + k_{ys}(\epsilon'_w - \epsilon'_g)] \text{Im } \epsilon_w}. \quad (5)$$

Calculations performed using expressions (4) and (5) with allowance for the dispersion equations for planar waveguides⁴ have shown in particular that the values of $|\delta S[\delta(\text{Im } \varepsilon_s)]^{-1}|$ and $|\delta R[(\varepsilon_a - \varepsilon'_s)k_0\Delta]^{-1}|$ have maxima for critical thicknesses of the waveguide film, and decrease with increasing mode number. For comparison, we note that in conventional detectors, where the angles of resonant excitation of the modes are recorded, the optimal thicknesses of the waveguide films differ from the critical values.¹ Their values correspond to the maxima of $|\partial \text{Re } h / \partial \varepsilon'_s|$ and $|\partial \text{Re } h / \partial \Delta|$, i.e., they are selected using different criteria.

These results were used to fabricate a detector to measure the ammonia concentration in the atmosphere. The waveguide structure was prepared by rf sputtering of a buffer layer of silicon dioxide ($\varepsilon_g = 2.19$ and $g = 0.13 \mu\text{m}$) on a glass prism ($\varepsilon_p = 3.06145$) followed by the deposition of a porous waveguide film ($d = 4.98 \mu\text{m}$, $\varepsilon'_w = 2.3173$) of polymethylmethacrylate activated with methyl red. The radiation source was a single-mode helium–neon laser ($\lambda_0 = 0.6328 \mu\text{m}$). The measurements were made by placing the detector in a transparent closed container, filled with air with a known concentration C of ammonia. The complex propagation constant of the dominant mode was first measured by the waveguide method³ for a Gaussian beam of radius $W = 91 \mu\text{m}$. As a result, we obtained $k_0^{-1} \text{Re } h|_{C=0} = 1.52072$, $k_0^{-1} \text{Im } h|_{C=0} = -3.07 \times 10^{-4}$, $p_1|_{C=0} = -0.694$, and $p_2 = 0.127$ and we plotted $\text{Re } h$ and $\text{Im } h$ as functions of C .

Interpolating these curves for $C < 4.3 \times 10^{-4}$ mg/liter yielded $k_0^{-1} \partial(\text{Re } h) / \partial C = -1.32$ liter/mg, $k_0^{-1} \partial(\text{Im } h) / \partial C = -0.135$ liter/mg, and $D = 9.81$. This value of D corresponds to the optimum curve $R(C)$ plotted in Fig. 1a, which was calculated with expressions (1) and (3) for $F_0 > 0$, $W = 870 \mu\text{m}$ ($H = -0.126$) using the given values of the parameters. For our waveguide structure, $u = -0.183$ differed significantly from the optimum $u = -0.315$ ($g = 0.052 \mu\text{m}$) and thus the detector was optimized only by increasing the beam radius to $W = 870 \mu\text{m}$ and selecting the angle α from the condition $\partial F_0 / \partial v = 0$. The corresponding calculated curve $R(C)$ is plotted in Fig. 1, curve b. The asterisks represent the experimental data obtained after taking into account the coefficients of propagation of the beam through the side faces of the prism.

The authors wish to thank A. V. Tomov for assistance with fabricating the waveguides.

¹K. Tiefenthaler and W. Lukosz, J. Opt. Soc. Am. B **6**, 209 (1989).

²A. K. Nikitin, A. A. Tishchenko, and A. I. Chernyaĭ, Zarub. Radioelektron. No. 10, 14 (1990).

³A. B. Sotskiĭ, A. V. Khomchenko, and L. I. Sotskaya, Opt. Spektrosk. **78**, 502 (1995) [Opt. Spectrosc. J. **78**, 453 (1995)].

⁴D. Marcuse, *Integrated Optics* (IEEE Press, New York, 1973) [Russ. transl., Mir, Moscow, 1974].

Translated by R. M. Durham

Normal zone propagation velocity in a superconducting wire with a copper-aluminum stabilizing matrix

V. V. Lysenko and O. P. Anashkin

“Kurchatov Institute” Russian Scientific Center, Moscow

(Submitted December 19, 1996)

Pis'ma Zh. Tekh. Fiz. **23**, 52–57 (July 12, 1997)

Results of measurements of the normal zone propagation velocity in superconducting wires with a copper-aluminum stabilizing matrix are presented. The measurements were made using test coils which reproduce the structure of real, compound and noncompound, magnets. One-dimensional propagation of the normal zone in the winding was simulated by means of a special coil design. © 1997 American Institute of Physics. [S1063-7850(97)01007-0]

The propagation of the resistive zone to a considerable extent determines the quench behavior of a superconducting magnet undergoing a transition to the normal state. A knowledge of the propagation velocities of the normal zone allows us to predict the maximum temperature and electrical voltages in the winding and to design a protection system. The strong dependence of this velocity on the electrical and thermophysical properties of the conductor, the insulating materials, and the liquid helium content in the winding makes it fairly difficult to use calculation methods.

The propagation of the normal zone boundary along a transport-current-carrying superconductor has been studied experimentally for single conductors washed with boiling helium,^{1,2} and also for ideal thermally insulated conductors.³ These conditions differ substantially from the situation inside tightly wound magnets, where the heated part of the conductor inside the winding is cooled by thermal contact with neighboring turns and, in noncompound windings, by heat transfer to the boiling helium, some of which may be located in the voids. Three-dimensional propagation of the normal zone in adiabatic (compound) magnets has been studied experimentally by various authors,⁴ whereas the dynamics of the normal zone in closely packed noncompound windings has barely been touched upon. In addition, the conditions for non-steady-state cooling by boiling helium in narrow channels are almost unknown.

Here we present results of measurements of the normal zone propagation velocity in conductors having a stabilizing matrix of technical-grade aluminum jacketed by with a thin layer of copper.⁵ The experiments were carried out using small test coils reproducing the structure of real superconducting magnets in terms of cooling conditions. To facilitate the analysis of the experimental results, we simulated the one-dimensional propagation of the normal zone along the conductor by using a special design of test coil. The conductor measured 3.5×2 mm and the thickness of the copper jacket was around $50 \mu\text{m}$. Composite superconducting wire, 0.7 mm in diameter, made of a niobium-titanium alloy, was soldered in a groove in the matrix. The conductor was insulated with polyimide film, the total thickness of the insulation being 0.12 mm. The measurements were made using two grades of conductor having different matrix materials: A5E technical-grade aluminum and A995 relatively high-purity aluminum. Aluminum has conventionally been used

as a stabilizing material to achieve steady-state stability, for which the purest possible aluminum was used. These conductors do not possess such high electrical conductivity and are designed for use in magnets which are not steady-state stabilized.

The experiments were carried out using compound and noncompound coils in order to study the influence of liquid helium possibly contained in the winding. The coils were impregnated with ED20 epoxy compound by the “wet” winding method. For the unimpregnated coils our estimates indicated that the voids did not occupy more than 3% of the total volume, bearing in mind that the winding was close packed. The test coils were wound onto Textolite formers and had an inner diameter of 58 mm, an outer diameter of 110 mm, and a length of 80 mm. There were 12 layers in the winding. Measurements were made on the fifth layer, which was the only one to which current was supplied. The other layers provided the boundary conditions simulating the structure of a real magnet. The fifth layer was wound with two parallel wires. For the measurements the current was supplied to one of the wires in the layer and the second wire functioned as a heat insulator for the turns of the first. Estimates have shown that this design sharply reduces the influence of the transverse diffusion of heat on the longitudinal propagation of the normal zone while maintaining the cooling conditions of the normal zone characteristic of the winding. A Manganin heater was placed at one end of the wire. Potentials were recorded by five internal taps situated at 0.5 m intervals along the coil. The first of these potential taps was approximately 0.7 m from the heater. The point where the wire emerged from the coil served as the sixth tap. An external magnetic field was generated by a superconducting solenoid with a 120 mm diameter aperture, fitted with a superconducting short. The measurements were made with a “frozen” external field. The entire assembly was placed in a test cryostat having an inner diameter of 240 mm.

During the experiments, the conductor was supplied with a current of given magnitude, a normal zone was initiated by the heater and the voltages were recorded at five consecutive sections using a loop oscilloscope. The transport current in the sample and the external magnetic field were constant in time. The velocity of the normal zone in each section was defined as the ratio of the length of the section to the time interval between the onset of voltage in that section and in

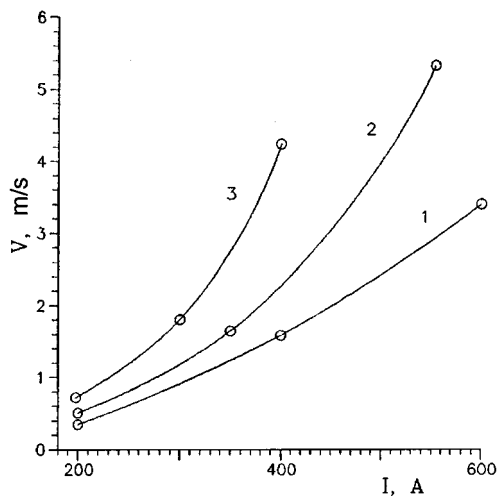


FIG. 1. Propagation velocity of the normal zone as a function of current in a conductor stabilized with A5E aluminum. External magnetic field: 0 T (1), 2 T (2), and 4 T(3). Compound winding.

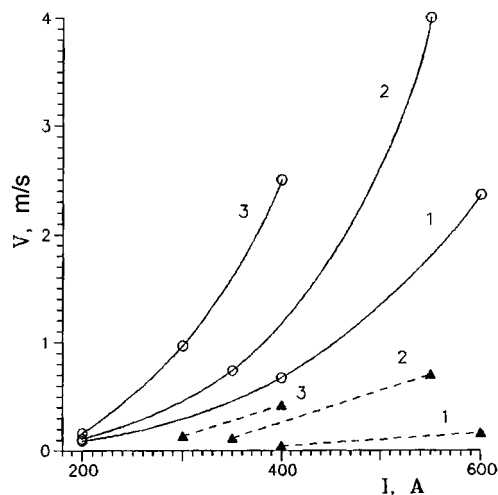


FIG. 2. Propagation velocity of the normal zone as a function of current. Conductor stabilized with A5E aluminum (circles) and A995 aluminum (triangles). External magnetic field: 0 T (1), 2 T (2), and 4 T(3). Noncompound winding.

the subsequent one. Thus, the velocity could be calculated for four sections and then the average velocity could be calculated for the two inner sections. According to our estimates, the error in determining the velocity for each section did not exceed 15% for most points.

The experimentally determined values of the voltage for the section of wire completely transferred to the normal state could be used to determine the residual resistivity (averaged over the cross section). For the wire with a stabilizing matrix of A5E aluminum in a transverse magnetic field of 0, 2, and 4 T, this resistivity was 1.0×10^{-9} , 1.2×10^{-9} , and $1.4 \times 10^{-9} \Omega \cdot m$ and for the wire stabilized with A995 aluminum, the residual resistivity was 1.3×10^{-10} , 2.9×10^{-10} , and $3.7 \times 10^{-10} \Omega \cdot m$, respectively. The critical currents for both conductors were similar, 800 and 540 A in magnetic fields of 2 and 4 T, respectively.

Figure 1 gives the results of measurements for a compound winding of A5E aluminum-stabilized wire. A comparison between the experimental values of the velocity and the results of the numerical calculations (performed by a finite-difference method, using real temperature dependences of the specific heat of the conductor and other parameters) revealed that the propagation of the normal zone is appreciably influenced by cooling of the conductor through contact with neighboring turns. The experimental values were 1.2–3 times lower than the velocities calculated in the adiabatic approximation. The rates of cooling correspond to effective coefficients of heat transfer in the range $40\text{--}120 \text{ W} \cdot \text{m}^{-2} \text{ K}^{-1}$.

Figure 2 gives experimental results for noncompound windings. In this case, for a conductor with a stabilizing matrix of A5E aluminum, the velocities were 1.4–3 times lower than those for the compound coil, which may be attributed to the presence of liquid helium in the winding. This difference is smaller, the higher the velocity of the normal zone and the weaker the influence of the helium cooling. It can be seen from Fig. 2 that the velocity of the normal zone in a conductor with an A995 aluminum stabilizing matrix is

considerably lower than that in the first type of conductor (under the same cooling conditions). This difference ranges between approximately a factor of 15 in the self-field to a factor of 5 at maximum currents in fields of 2 and 4 T. Note that the theory⁶ indicates that the velocities of the normal zone in these conductors should be approximately equal under adiabatic conditions. Thus, a small amount of liquid helium contained in the winding (up 3% by volume) drastically alters the dynamics of the normal zone.

Such a low normal zone propagation velocity in the A995 aluminum-stabilized conductor may pose a serious hazard from the point of view of the protection of large superconducting magnets. The extremely nonuniform dissipation of the stored energy may lead to damage to the winding by overheating. One method of solving this problem is to use conductors with a stabilizing matrix of high residual resistivity in these windings.

An additional advantage of these conductors is their substantially improved mechanical properties.

This work was supported by the Scientific Council on High-Temperature Superconductivity (Project N 93172).

¹Z. J. J. Stekly and E. Hoag, *J. Appl. Phys.* **34**, 1376 (1963).

²L. Dresner, *Cryogenics* **16**, 675 (1976).

³C. H. Joshi and Y. Iwasa, *Cryogenics* **29**, 157 (1989).

⁴A. V. Gavrilin, A. A. Konyukhov, and V. A. Malginov, *IEEE Trans. Magn.* **32**, 2990 (1996).

⁵O. P. Anashkin, Yu. P. Ipatov, V. E. Keřlin *et al.*, *Élektrotehnika* No. 3, 17 (1991).

⁶M. Wilson, *Superconducting Magnets* (Oxford University Press, London, 1983) [Russ. transl. Mir, Moscow, 1985].

Translated by R. M. Durham

Structural and noise characterization of VO₂ films on SiO₂/Si substrates

M. V. Baïdakova, A. V. Bobyl', V. G. Malyarov, V. V. Tret'yakov, I. A. Khrebtov,
and I. I. Shaganov

St. Petersburg State Technical University
(Submitted January 17, 1997)

Pis'ma Zh. Tekh. Fiz. **23**, 58–65 (July 12, 1997)

Multi-technique structural and electrophysical investigations of VO₂ films on SiO₂/Si substrates are carried out to study the microscopic nature of fluctuator defects — sources of low-frequency flicker noise. It is established that the noise intensity is determined by the magnitude of the microstress fluctuations $\langle \varepsilon \rangle = \{ \langle (\delta c/c)^2 \rangle \}$, where c is the lattice parameter along the c -axis parallel to [011] direction in the blocks of which the film is formed. The dimensions of the blocks were determined in the direction of the c -axis ($t_c \sim 1000$ Å). The suggestion is put forward that the samples contain two types of fluctuator defects: 1) V atoms jumping between the two nearest interstitial sites and 2) V atoms jumping between these interstitial sites near lattice defects. © 1997 American Institute of Physics. [S1063-7850(97)01107-5]

Interest has been shown in VO₂ films because of the possibility of using the abrupt temperature dependence of their properties in various practical applications,^{1–7} and also in connection with studying the physics of the corresponding structural phase transition.^{1–10} Low-frequency flicker noise may indicate random changes in the microstructure of the sample, and also so-called fluctuator defects,^{10–12} and may therefore provide an effective criterion for technological monitoring of these changes.

With the aim of studying the microscopic nature of these fluctuator defects, we made a multi-technique structural and electrophysical investigations of VO₂ films on SiO₂/Si substrates prepared by magnetron sputtering. These investigations included x-ray structural phase analysis, x-ray spectral microanalysis, scanning microscopy, and measurements of the flicker noise intensity, the resistance, and its temperature dependence. It was established that the flicker noise intensity is determined by the microstress fluctuations $\langle \varepsilon \rangle = \{ \langle (\delta c/c)^2 \rangle \}$, where c is the lattice parameter in the [011] direction) in the blocks of which the film is made. The dimensions of the blocks were determined in the direction of the c -axis ($t_c \sim 1000$ Å). The results allowed us to put forward a hypothesis as to the microscopic nature of these fluctuator defects.

Table I gives the parameters of the magnetron sputtering process and the thickness of the SiO₂ sublayer deposited on a KÉF4.5 Si:P substrate. The sublayer thickness as well as the composition and thickness of the VO₂ film were determined using a Camebax x-ray spectral microanalyzer and a specially developed program which took into account the multilayer nature of the region of formation of the recorded signal.¹³ This method of microanalysis did not provide highly accurate absolute values of the oxygen content of the films, and thus Table I gives the values normalized to the content in sample No. 4.

An examination made using a CamScan scanning electron microscope revealed no inclusions or roughness of dimensions $>0.1 \mu\text{m}$ on the surface of the films.

Structural phase analyses of the sublayer and the films were made using a Rigaku single-crystal x-ray diffractometer

with a rotating copper anode. The results are presented in Table I and plotted in Fig. 1.

It is known⁷ that for VO₂ films grown on SiO₂/Si substrates, the preferential direction of growth of the blocks is in the [011] direction. Data from Ref. 14 confirms that the diffraction pattern (Fig. 1) contains VO₂ peaks ((011), (022), (012), and (021)) and a series of low-intensity peaks. The latter may be associated with reflections from a particular set of planes in V₂O₄, which cannot be identified since the structure of V₂O₄ has not been worked out.¹⁴ The interplanar spacing for the VO₂ (011) planes was calculated from the position of the diffraction peaks and it was found that within measurement error this spacing agrees with that for free VO₂, as was to be expected in the presence of an amorphous SiO₂ sublayer. The structural perfection of the blocks is not good: the width of the rocking curve being $>6^\circ$ for the (011) peak.

Thus these results confirm that, to a high degree of accuracy the films have a stoichiometric VO₂ composition and both phases have a block-mosaic structure.¹⁵ A considerable fraction of the blocks have a VO₂ phase composition, while the interblock sections have a V₂O₄ phase composition. Using the line widths given in Table 1, we can use the model to estimate the dimensions t_c of the blocks along the c -axis and the microstress fluctuations $\langle \varepsilon \rangle$. It is known¹⁵ that in the block model, the line width $\omega_{2\nu}$ consists of two component and depends as follows on the Bragg angle ν_{Br} :

$$\omega_{2\nu}^2 = \omega_{\langle \varepsilon \rangle}^2 + \omega_c^2 = (2\langle \varepsilon \rangle \tan \nu_{\text{Br}})^2 + \left(\frac{\lambda}{2t_c \cos \nu_{\text{Br}}} \right)^2, \quad (1)$$

where ω_c and $\omega_{\langle \varepsilon \rangle}$ are the widths caused by the presence of the blocks and by microstress fluctuations in these blocks, respectively, and λ is the wavelength of the x-rays. The results of the calculations are also presented in Table I.

For the electrophysical measurements, we prepared bridges with the dimensions given in Table I, which had in contacts with the Ti sublayer. The resistance R of the samples had a semiconducting temperature dependence, with the activation energies E_{act} given in Table I. For the noise intensity measurements we used a metal cryostat and an am-

TABLE I.

Sample No.	Process parameters			Film composition (relative to stoichiometric)		Bridge dimensions
	Pressure in growth chamber, mTorr		SiO ₂ sublayer	V	O	
	O	Ar+O	Thickness Å			Length-width-thickness, μm
4	0.21	2.0	4110	1.009	1	750-2100-0.36
5	0.21	1.9	600	1.011	1.001	40-100-0.33
6	0.23	2.1	1750	1.011	1.002	30-100-0.37
7	0.21	1.9	6500	0.995	0.998	30-100-0.34

TABLE I. (Continued.)

Sample No.	Electrophysical parameters of bridges			X-ray line widths ω _{2γ}		Parameters of blocks	
	R, kΩ 300 K	E _{act} , eV	Hooqe parameter at 10 Hz	(011) deg	(022) deg	t _c , Å	⟨ε⟩ × 10 ⁻³
4	3.1	0.20	6	0.164	0.35	900	5.2
5	74.3	0.21	90	0.191	0.41	1200	7.3
6	12.1	0.16	60	0.188	0.428	1100	7.1
7	6.2	0.13	25	0.190	0.415	1200	7.4

plifier with a special low-noise input transistor. The dimensionless Hooqe parameter¹⁶ α was used to characterize the noise properties of the samples. The parameter α was calculated assuming that the volume of a unit cell was 37 Å³ (Refs. 17 and 18) and allowance was made for the energy gap between the *d*-levels of the valence band and the *p*-levels of the conduction band,¹⁹ which was taken to be 2E_{act}. The values of α obtained at a frequency of 10 Hz are

also given in Table I and the corresponding frequency dependences are plotted in Fig. 2.

In the coordinates used in Fig. 2, a 1/*f* frequency dependence of the noise intensity would be a horizontal line (i.e., $\alpha = \text{const}$). The experimentally observed dependence $\alpha(f)$ was first described in Ref. 5, and may be explained in terms of the fluctuator defect model mentioned previously, i.e., by using the concept of the distribution of fluctuator defects over the energy spectrum *E*, whose scale is also plotted in Fig. 2 and which is determined from the relation

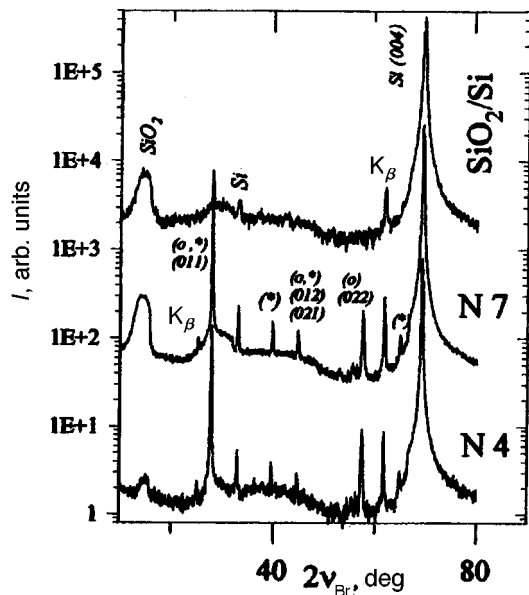


FIG. 1. X-ray diffraction pattern for a substrate with a sublayer and two samples (the numbering corresponds to that in Table I). CuK_α radiation ($\lambda = 1.541$ Å). The diffraction peaks of the structures are indicated: o — VO₂, * — V₂O₄ according to data from Ref. 14, Cards No. 9-142 and 19-1398, respectively. The Miller indices are given for VO₂.

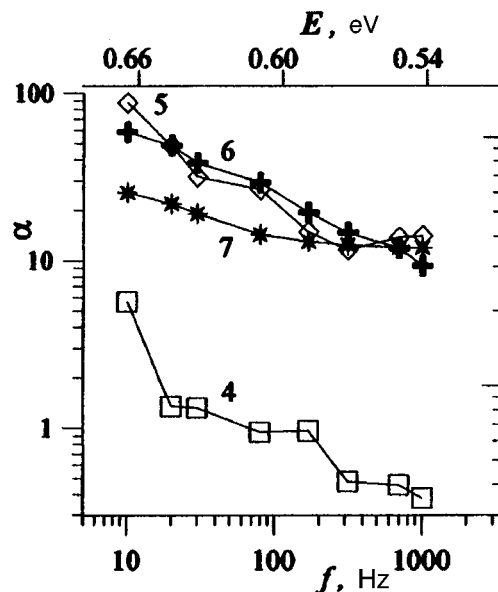


FIG. 2. Hooqe parameter versus frequency and energy calculated using Eq. (2). The curves are numbered as in Table I.

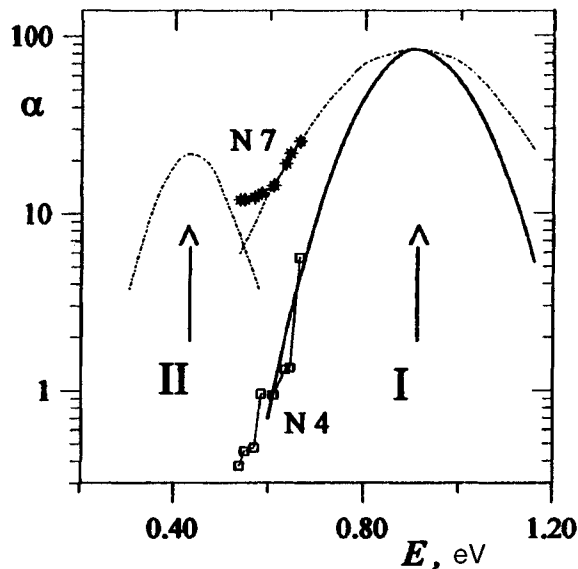


FIG. 3. Model of spectrum of two types of fluctuator defects (I and II) for two samples; the corresponding experimental points are plotted.

$$E = -kT \ln 2\pi f \tau_D, \quad (2)$$

where $(\tau_D)^{-1}$ is the Debye frequency ($\sim 10^{-13} \text{ s}^{-1}$).

Before discussing the possible form of the spectral curve $\alpha(E)$ and the fluctuator defect micromodel, we need to identify the strongest correlation between structure and noise. Comparing the structural results obtained for different samples with the Hooge parameter, we can conclude that this is the dependence $\alpha(\langle \varepsilon \rangle)$ which was observed previously in studies of high-temperature superconducting $\text{YBa}_2\text{Cu}_3\text{O}_7$ films.¹² It was found that the intensity of the flicker noise depends exponentially on the value of $\langle \varepsilon \rangle$ in the blocks forming the film. This dependence has the form

$$\ln \alpha \sim \langle \varepsilon \rangle^2 \quad (3)$$

and is observed for VO_2 films, as may be confirmed using the data given in Table I and plotted in Fig. 2. The behavior (3) may be obtained using the following model of fluctuator defects. The lattice atoms perform random, thermally activated jumps to empty sites in the unfilled sublattice (or between interstitial sites). The random fields of microstresses lead to corresponding fluctuations in the barrier height of the double-well potential across which the atoms jump, and to differences between the minimum energies.

To interpret the results plotted in Fig. 2, we need to hypothesize that two types of fluctuator defects exist. Their spectrum of fluctuator defects is shown schematically in Fig. 3, where it is assumed that the fluctuator defects have a Gaussian energy distribution. The approximate energy of a type I maximum is $\sim 1 \text{ eV}$. Approximately the same estimate may be obtained from the results of Ref. 20, where internal friction was studied in VO_2 powders. The following assumption may be made in relation to the model of type I fluctuator defects. First, it should be noted that the energy of defect formation in oxides is considerably higher than these values ($\sim 2\text{--}3 \text{ eV}$ (Ref. 21)). However, it was recently observed that in rutile structures, particularly in TiO_2 oxides,²² consid-

erable anisotropic diffusion of cation lattice atoms between interstitial sites with substantially lower energies of $\sim 1.4 \text{ eV}$ is observed in the presence of substitutional impurities. Thus, it may be hypothesized that the type I fluctuator defects are V atoms jumping between two neighboring interstitial sites, and the substitutional impurities can either be accidental impurities or other valence states of the V atoms. It may be postulated that the type II fluctuator defects are also jumps of V atoms between interstitial sites situated near lattice defects, or V atoms of different valence.²¹

The authors would like to thank V. S. Vikhnin, A. I. Morozov, R. A. Suris, and F. A. Chudnovskii for many useful comments.

This work was supported by the Russian Fund for Fundamental Research, Grant No. 9602-18563.

- ¹A. A. Bugaev, B. P. Zakharchenya, and F. A. Chudnovskii, *The Metal-Semiconductor Phase Transition and Its Applications* [in Russian] (Nauka, Moscow, 1979).
- ²N. Tsuda, K. Nasu, A. Yanase, and K. Siratori, Springer Series in Solid-State Sciences, Vol. 94 (Springer-Verlag, Berlin, 1991).
- ³M. P. Shaw, V. V. Mitin, E. Scholl, and H. L. Grubin, *The Physics of Instabilities in Solid-State Electron Devices* (Plenum Press, New York, 1992).
- ⁴A. Fujimori and Y. Tokura, *Spectroscopy of Mott Insulators and Correlated Materials*, Springer Series in Solid-State Sciences, Vol. 119 (Springer-Verlag, Berlin, 1995).
- ⁵V. N. Andreev, B. P. Zakharchenya, Yu. S. Kapshin, V. A. Noskin, and F. A. Chudnovskii, Zh. Éksp. Teor. Fiz. **79**, 1353 (1980) [Sov. Phys. JETP **52**, 684 (1980)].
- ⁶V. S. Vikhnin, I. N. Goncharuk, V. Yu. Davydov, F. A. Chudnovskii, and E. B. Shadrin, Fiz. Tverd. Tela (St. Petersburg) **37**, 3580 (1995) [Phys. Solid State **37**, 1971 (1995)].
- ⁷P. Jin and S. Tanemura, Jpn. J. Appl. Phys. **33**, Part. 1, 1478 (1994); **34**, Part. 1, 2459 (1995).
- ⁸R. M. Wentzcovitch, W. W. Schulz, and P. B. Allen, Phys. Rev. Lett. **72**, 3389 (1994).
- ⁹T. M. Rice, H. Launois, and J. P. Pouget, Phys. Rev. Lett. **73**, 3043 (1994).
- ¹⁰Sh. M. Kogan and K. É. Nagaev, Fiz. Tverd. Tela (Leningrad) **24**, 1921 (1982) [Sov. Phys. Solid State **24**, 1921 (1982)].
- ¹¹Y. M. Galperin, V. G. Karpov, and V. I. Kozub, Adv. Phys. **38**, 669 (1989).
- ¹²A. V. Bobyl, M. E. Gaevskii, S. F. Karmanenko, R. N. Kutt, R. A. Suris, I. A. Khrebtov, A. D. Tkachenko, and A. I. Morosov, J. Appl. Phys. (1997), in press.
- ¹³S. V. Kazakov, S. G. Konnikov, and V. V. Tretyakov, X-Ray Spectrosc. **19**, 269 (1990).
- ¹⁴JCPDS International Center for Diffraction Data, Swarthmore, PA.
- ¹⁵B. E. Warren and B. L. Averbach, J. Appl. Phys. **21**, 595 (1950).
- ¹⁶F. N. Hooge, T. G. M. Kleinpenning, and L. K. L. Vandamme, Rep. Progr. Phys. **44**, 479 (1981).
- ¹⁷M. Gupta, A. J. Freeman, and D. E. Ellis, Phys. Rev. B **16**, 3338 (1977).
- ¹⁸F. Gervais and W. Kress, Phys. Rev. B **31**, 4809 (1985).
- ¹⁹M. Abbate, F. M. F. de Groot, J. C. Fuggle, Y. J. Ma, C. T. Chen, F. Sette, A. Fujimori, Y. Ueda, and K. Kosuge, Phys. Rev. B **43**, 7263 (1991).
- ²⁰J. X. Zhang, Z. H. Yang, and P. C. W. Fung, Phys. Rev. B **52**, 278 (1995).
- ²¹L. L. Odynets and V. M. Orlov, *Anodic Oxide Films* [in Russian], Nauka, Leningrad (1990).
- ²²K. Ruebenbauer, U. D. Wdowik, and M. Kwater, Phys. Rev. B **54**, 4006 (1996).

Translated by R. M. Durham

Physical model of the transition from a hexagonal to a cubic structure during growth of boron nitride under nitrogen and argon ion irradiation

Yu. V. Trushin

A. F. Ioffe Physicotechnical Institute, Russian Academy of Sciences, St. Petersburg
(Submitted January 17, 1997)

Pis'ma Zh. Tekh. Fiz. **23**, 66–70 (July 12, 1997)

A model based on original experimental data is proposed to describe the transition of the structure from hexagonal to cubic during the growth of boron nitride layers. It is postulated that boron and nitrogen ions entering the growing layer form additional atomic planes parallel to the (*ab*) planes of the hexagonal structure or complete existing dislocations in the growing crystal, causing the boron nitride to undergo a transition to a cubic structure. © 1997 American Institute of Physics. [S1063-7850(97)01207-X]

It has been established experimentally^{1–3} that when thin boron nitride (BN) layers are grown by ion-beam assisted deposition using N_2^+ and Ar^+ ions with energies between 0.5 and 1.5 keV, hexagonal BN grows on a silicon substrate with the *c* axis parallel to the surface. Under this irradiation, nitrogen ions enter the growing material and boron is “driven in” by interaction between the boron atmosphere and Ar^+ ions at the surface of the growing sample. As a result, a transition is observed from hexagonal boron nitride (*h*-BN) to the cubic phase (*c*-BN).

Let us consider a physical model for the transition from a hexagonal to a cubic BN structure during the growth of *h*-BN layers under nitrogen and argon ion irradiation. We make the following assumptions:

- 1) Nitrogen and boron ions entering the *h*-BN are in the form of interstitial atoms (*i*N and *i*B) during irradiation and are distributed between the (*ab*) planes in the hexagonal BN.
- 2) Interstitial *i*N and *i*B atoms diffuse to an external sink (the surface, Λ) and to internal sinks, such as dislocations (*D*), which are always present in growing crystals.
- 3) Mobile nitrogen and boron atoms (*i*N and *i*B) may form BN molecules which will nucleate new additional boron nitride planes between the existing (*ab*) planes in the hexagonal structure.

We write the following equations for the concentrations of interstitial nitrogen and boron atoms (C_{iN} and C_{iB}) and implanted argon (C_{Ar}):

$$\frac{\partial C_{iN}(r,t)}{\partial t} = g_{iN}^h(E, r, t) + \text{div} J_{iN}(r, t) - \alpha_{BN}(D_{iN} + D_{iB})C_{iN}C_{iB} - D_{iN}C_{iN}(S_D + S_F + S_\Lambda), \quad (1)$$

$$\frac{\partial C_{iB}(r,t)}{\partial t} = g_{iB}^h(E_{Ar}, r, t) + \text{div} J_{iB}(r, t) - \alpha_{BN}(D_{iN} + D_{iB})C_{iN}C_{iB} - D_{iB}C_{iB}(S_D + S_F + S_\Lambda), \quad (2)$$

$$\frac{\partial C_{Ar}(r,t)}{\partial t} = g_{Ar}^h(E_{Ar}, r, t) + \text{div} J_{Ar}(r, t) - D_{Ar}C_{Ar}S_\Lambda. \quad (3)$$

Here $g_j^h(E, r, t)$ is the rate of generation of interstitial nitrogen and boron atoms and also argon atoms ($j = iN, iB, Ar$) in *h*-BN; E and E_{Ar} are the energies of the impinging nitro-

gen and argon ions, respectively; $J_j(r, t)$ is the flux density of *j*th particles at point r and time t ; $S_D + S_F$ and S_Λ are the strengths of the internal sinks (D — dislocations and F — new additional BN planes in *c* directions) and of the external surface sink (Λ); D_j is the carrier diffusion coefficient where $j = iN, iB$, and Ar ; and $\alpha_{BN} = 4\pi l_{BN}$, where l_{BN} is the B and N capture distance for the formation of a BN molecule.

The balance of particles (B, N, Ar) in the material (*h*-BN) per unit volume at time t may be written as follows:

$$\rho_{nc}(t) = \rho_{nc}^h + C_{iB}(t) + C_{iN}(t) + C_{Ar}(t) + N_F(t) + N_D(t). \quad (4)$$

Here $C_j(t)$ is the average volume concentration, where $j = iN, iB$, and Ar , $\rho_{nc}(t)$ is the nuclear density of the material at time t , ρ_{nc}^h is the nuclear density of the hexagonal BN, $N_F(t)$ is the number of N and B atoms per cm^3 which have formed additional F planes in *h*-BN by time t , and $N_D(t)$ is the number of N and B atoms per cm^3 lost to internal sinks in the form of dislocations by the time t .

Let us assume that t_1 is the time taken for growth of hexagonal BN in the experiments^{1–3} (approximately 30 min). Then, by this time we have:

- a) $\rho_{nc}^h(t_1) = \rho_{nc}^c$ (nuclear density of cubic BN),
- b) $C_{Ar}(t_1) = 4\% \rho_{nc}^h$ (see Ref. 3),
- c) $C_{iN}(t_1) = C_{iB}(t_1) = 0$ (all mobile nitrogen and boron atoms are situated only at sinks).

Using Eq. (4) and the conditions (5), we obtain

$$\rho_{nc}^c - 0.96\rho_{nc}^h = N_F(t_1) + N_D(t_1). \quad (6)$$

The following expressions may be written for $N_F(t)$ and $N_D(t)$ (see Refs. 4–6):

$$N_F(t) = S_F \int_{t_0}^t [D_{iN}C_{iN}(t') + D_{iB}C_{iB}(t')] dt', \quad (7)$$

$$N_D(t) = S_D \int_{t_0}^t [D_{iN}C_{iN}(t') + D_{iB}C_{iB}(t')] dt', \quad (8)$$

where t_0 is the time for the onset of hexagonal BN growth. The strengths of the internal sinks can be written as (see Refs. 4–6, for example):

$$S_D = \alpha_D \rho_D, \quad S_F = \alpha_F C_F R_F, \quad (9)$$

where ρ_D is the dislocation density, C_F and R_F are the concentration and mean "radius" (in the adiabatic approximation, see Refs. 6–8) of the additional new plane fragments F in h -BN, and α_D and α_F are the adsorption parameters for the dislocations and the new planes (of the order ≈ 1).

To estimate the total strength of the internal sinks ($S_D + S_F$) and the external sinks S_Λ , we assume that the interstitial nitrogen and boron atoms (iN and iB) have the same migration activation energies $\varepsilon_{iN}^m = \varepsilon_{iB}^m \approx 0.1$ eV and therefore about the same diffusion coefficients $D_{iN} = D_{iB} = D$. Then, the average concentrations are $C_{iB}(t) = C_{iN}(t) = C(t)$ and thus, expressions (7) and (8) have the form

$$N_F(t) \approx 2DS_F \int_{t_0}^t C(t') dt', N_D(t) \approx 2DS_D \int_{t_0}^t C(t') dt'. \quad (10)$$

Solving Eq. (3) for the average argon ion concentration with allowance for their experimental rate of generation³ and condition (5b), we can obtain the following estimate for the surface sink strength

$$S_\Lambda \approx 4 \times 10^2 / \omega \approx 4 \times 10^{n+2} \text{ cm}^{-2}, \quad (11)$$

where $\omega \approx 10^{-n}$ is the probability of energy transfer from argon ions to boron atoms ($n > 1$).

Using Eqs. (1) and (2) with Eqs. (4) and (10), the volume-averaged concentrations at time t_1 can also be given by:

$$N_F(t_1) + N_D(t_1) \approx 2g^h \Delta t \frac{S_D + S_F}{S_D + S_F + S_\Lambda}. \quad (12)$$

Using condition (6), expression (12) gives

$$S_D + S_F \approx 1.43 \times 10^{-3} S_\Lambda, \quad (13)$$

and allowing for the estimate (11), we obtain

$$S_D + S_F \approx 6 \times 10^{n-1}. \quad (14)$$

It should be noted that the exponent n is not too large and thus (see expression (9)), the density of the dislocations in the growing sample will not be too great, as has been established by electron microscopic analyses during the growth of SiC layers by similar methods.

To sum up, it has been shown that by assuming that in the growth of layers of hexagonal boron nitride additional atomic planes are formed between the existing (ab) planes along the c axis during the growth process under nitrogen and argon ion irradiation in a boron atmosphere, the physical conditions derived from the balance of particles impinging on the surface of initially hexagonal and then cubic BN can be maintained. The incipient new additional planes also cause a gradual transition from h -BN to c -BN as a result of changes in the interatomic spacings in the growing boron nitride. These results are estimates which serve to demonstrate qualitatively the efficacy of the proposed physical model. The next stage will involve calculations of the spatial distributions of mobile nitrogen and boron atoms during the growth of h -BN where condition (4) is satisfied.

The author would like to thank colleagues at the Forschungszentrum Rossendorf, Prof. Möller, Dr. A. Kolitsch, Dr. V. Fukarek, and M. Plass, for supplying experimental data and for fruitful discussions.

This work was supported by the Russian Fund for Fundamental Research, Grant No. 96-02-17952.

¹M. F. Plass, W. Fukarek, A. Kolitsch, and U. Kreissig, *Surf. Coatings Technol.* **84**, 383 (1996).

²M. F. Plass, W. Fukarek, A. Kolitsch, M. Mader, and W. Möller, *Phys. Status Solidi A* **155**, K1 (1996).

³M. F. Plass, W. Fukarek, S. Mändl and W. Möller, *Appl. Phys. Lett.* **69**, 46 (1996).

⁴Yu. V. Trushin, *J. Nucl. Mater.* **185**, 279 (1991)

⁵Yu. V. Trushin, *Tech. Phys.* **39**, 564 (1993).

⁶Yu. V. Trushin, *Theory of Radiation Processes in Metal Solid Solutions* (Nova Science Publishers, New York, 1996).

Translated by R. M. Durham

Fractal structure and some physical properties of carbon deposits obtained by sputtering of graphite in an electric arc

I. V. Zolotukhin and Yu. V. Sokolov

Voronezh State Technical University

(Submitted March 11, 1997)

Pis'ma Zh. Tekh. Fiz. **23**, 71–75 (July 12, 1997)

New experimental results are presented to show that when graphite is sputtered in an electric arc, a carbon deposit having a fractal structure is formed on the cathode. The superior microhardness and high microporosity indicate that this fractal carbon deposit may have applications in engineering. © 1997 American Institute of Physics. [S1063-7850(97)01307-4]

When fullerenes are prepared by the electric arc method, some of the evaporated graphite (up to 40% of the rod mass) is deposited on the cathode in the form of soot which has been called "carbon deposit."¹ This deposit is formed because of the nonequilibrium conditions (temperature and atomic concentration gradient) present when an electric arc burns. A carbon deposit obtained in He, Ar, and CH₄ atmospheres was studied in Ref. 2 and nanotubes, nanoparticles, and amorphous carbon were observed. In argon and helium atmospheres, nanotubes were formed at gas pressures above 20 and 50 Torr, respectively. Nanoparticles were formed at lower argon and helium pressures. Some physicochemical properties of carbon deposits obtained under roughly the same conditions as in Ref. 2, were studied in Ref. 3. It was established that compared with graphite, the carbon deposit possesses superior microhardness caused by the presence of local microdistortions and finely disperse zones, possibly incorporating accumulations of nanotube bundles.

These data do not provide any definite indication as to the structure and mechanisms of formation of these carbon deposits. Our aim in the present paper is to answer some of the questions relating to the structure and mechanisms of formation of carbon deposits during the sputtering of graphite in an electric arc.

A carbon deposit was obtained by sputtering a graphite rod in an arc discharge with the following parameters: current 180 A and voltage 15–20 V. The sputtered graphite was deposited at an argon pressure $P = 10$ Torr on the plane surface of a polished graphite cathode. The deposition time was 30 s and the thickness of the carbon deposit was $\sim 500 \mu\text{m}$. The deposit was removed from the cathode and its outer surface was analyzed in a scanning electron microscope and a scanning tunneling microscope. The microhardness was measured using a PMT-3 device, with a relative error of 14%, the density was measured by hydrostatic weighing, with a relative error of 0.8%, and the electrical resistivity was measured by a four-probe method, with a relative error of 9%.

The carbon deposit is a fairly hard structure with a microhardness of 5.95 GPa as compared with 0.22 GPa for graphite. The density of our carbon deposit was 1.32 g/cm^3 which provides evidence of its porosity (for comparison, the density of graphite is 2.3 g/cm^3). The electrical resistivity of the deposit was $1.4 \times 10^{-4} \Omega \cdot \text{m}$ whereas that of graphite is $1.5 \times 10^{-5} \Omega \cdot \text{m}$. Thus, the resistivity of the carbon deposit is

almost an order of magnitude higher than that of graphite, which also indicates its fairly porous structure.

The surface structure of the carbon deposit is shown in Fig. 1a. Fairly large ($4\text{--}8 \mu\text{m}$) cloud-like formations can be identified and these consist of smaller ($0.3\text{--}0.6 \mu\text{m}$) rounded accumulations. An examination of the initial stages of nucleation of the carbon deposit with a scanning tunneling microscope revealed that the structure consists of 6–8 nm carbon clusters, which serve as the base material for the formation

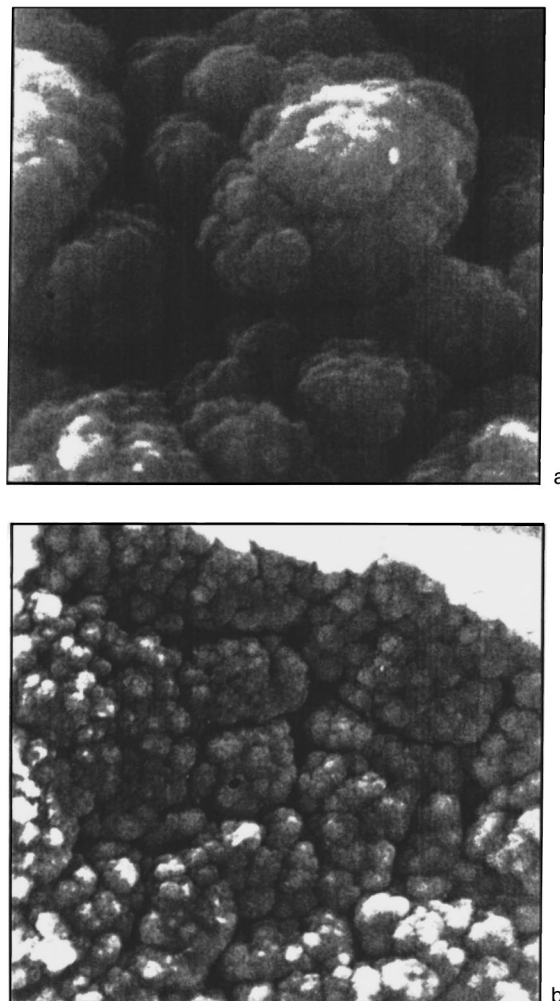


FIG. 1. Surface structure of carbon deposit: a — $\times 5300$, b — $\times 580$.

of 0.3–0.6 μm aggregates. During the deposition process, the aggregates form into macroscopic cloud-like formations having dimensions of 4–8 μm , which then form a structure reminiscent of a “cauliflower head” (see Fig. 1b). A similar surface structure is observed for dust particles obtained in a helium plasma with graphite electrodes in a 15 MHz rf discharge at a pressure of 1 Torr (Ref. 4).

The density of our carbon deposit is 57% of that of graphite whereas the microhardness is 27 times higher. These results indicate that the structure of the carbon deposit comprises a fairly rigid framework with an appreciable porous volume. This structure is typical of aerogels, whose fractal nature has been established beyond doubt. Thus, the experimental data convince us that the carbon deposit has a fractal structure.

To calculate the fractal dimension we use the model of fractal aggregates consisting of clusters of radius r_0 and having the density of graphite ρ_0 (Ref. 5). If the radius of a fractal aggregate is $R \gg r_0$, the number of clusters in it is given by:

$$N(r) = (R/r_0)^D, \quad 1 < D < 3, \quad (1)$$

where D is the fractal dimension. Formula (1) yields an expression to determine the density of material in a sphere of radius R :

$$\rho = \rho_0 (r_0/R)^{3-D}, \quad (2)$$

where ρ is the density of the carbon deposit. For $\rho = 1.32 \text{ g/cm}^3$, $\rho_0 = 2.3 \text{ g/cm}^3$, $r_0 = 4 \times 10^{-7} \text{ cm}$, and $R = 4.5 \times 10^{-5} \text{ cm}$, we obtain $D = 2.88$.

The formation of structures similar to carbon deposits may be represented in the same way as the formation of “dust particles” in a microwave plasma during etching.⁶ Initially, graphite is sputtered in the electric arc plasma with the formation of 2–6 nm charged carbon clusters. Some of these clusters collide in the plasma and, interacting by way of diffusion-limited aggregation, form fractal aggregates of up to 1 μm . Each of these fractal aggregates acquires a negative charge which may reach $Z_a = 10^4$ (Z_a is the charge of a fractal aggregate in units of electrical charge).⁶ Fluxes of positively charged argon ions recombine at fractal aggregates (dust particles). At high dissipation energies, conditions are satisfied for self-organization and for the formation of fairly stable, fractal carbon structures, which are formed according to the laws of formation of long-lived dust structures.⁶

To conclude, we should like to thank V. P. Ievlev and D. S. Dolgikh for assistance with the scanning electron microscope and scanning tunneling microscope examinations.

¹V. P. Bubnov, I. S. Krainskiĭ, and E. É. Laukhina, *Izv. Akad. Nauk Ser. Khim.* No. 5, 173 (1994).

²A. Yoshinori, *Fullerene Sci. Technol.* **2**(2), 173 (1994).

³Yu. S. Grushko, V. M. Egorov, I. N. Zimkin *et al.*, *Fiz. Tverd. Tela (St. Petersburg)* **37**, 1838 (1995) [*Phys. Solid State* **37**, 1001 (1995)].

⁴A. Jarscadden *et al.*, *Plasma Sources Sci. Technol.* **3**, 239 (1994).

⁵B. M. Smirnov, *Usp. Fiz. Nauk.* **152**, 133 (1987) [*Sov. Phys. Usp.* **30**, 420 (1987)].

⁶V. N. Tsytovich, *Usp. Fiz. Nauk.* **167**, 57 (1997).

Translated by R. M. Durham

Method of determining dynamic adiabatic compression curves of powders

V. V. Ivanov and A. A. Nozdrin

Institute of Electrophysics, Urals Branch of the Russian Academy of Sciences, Ekaterinburg

(Submitted February 14, 1997)

Pis'ma Zh. Tekh. Fiz. **23**, 76–80 (July 12, 1997)

A method is described for investigating the dynamic adiabatic compression curves of powders by measuring of the pulsed pressure in a powder pressed uniaxially by an elastic instrument.

The instantaneous powder density is determined by numerical solution of a pulsed spectral problem using the pressing pressure pulse and the known characteristics of the pressing instrument and the external force. © 1997 American Institute of Physics. [S1063-7850(97)01407-9]

Increasing interest has recently been shown in dynamic methods of compaction because pulsed compression is preferable for compacting some of the new types of powder materials. In particular, the dynamic compression of solid nanosize powders ($d = 5\text{--}100\text{ nm}$) can effectively overcome the adhesive coupling forces of the particles and can achieve higher pressing densities compared with static methods at the same pressure level.^{1–3} In view of the wide variety of powder materials, there is a need to develop a real-time method of studying their dynamic compressibility as a function of phase composition, dispersion, and particle shape.

We propose principles for the experimental determination of the dynamic adiabatic curves of powders using soft pulsed compression waves. A pulsed pressure is generated in the powder by accelerating a pressing instrument with a strong pulsed magnetic field and then stopping it with a powder target, and has typical rise and decay times of around $100\ \mu\text{s}$. Here, the pulse shape is determined by three factors: the accelerating force, the elastic properties of the pressing instrument, and the compressibility of the powder. Using the experimentally measured pressing pressure pulse $P(t)$, the elastic properties of the pressing instrument, determined by calibration, and the accelerating magnetic force $f(t)$, the method allows us to calculate the instantaneous powder density $\gamma(t)$.

The powder density is determined from the approach velocity of the plane surfaces of two punches in the cylindrical channel of a die block (Fig. 1):

$$\gamma(t) = \frac{\gamma_0 h_0}{h_0 - \int_0^t V(\xi) d\xi},$$

where γ_0 and h_0 are the initial density and filling height of the powder. The upper punch is moved by an impactor to which an external accelerating force $f(t)$ is applied. The lower, fixed punch rests on a rigid support. The volume of the powder being compressed between the punches is so small that the pressure near the boundaries of punches A and B can be considered to be the same (quasi-steady-state condition). The impactor and the punches have a single common degree of freedom x along which they move and undergo forced oscillations at natural frequencies. When the external force is such that the mechanical stresses in the pressing instrument are within the range of linear elasticity of the material (for P-18 steel $\sigma_T \leq 2\text{ GPa}$), the displacement of the punch boundaries is a linear function of the conditions at the boundaries, as has been verified experimentally. Then the

velocity of approach of the boundaries of punches A and B is expressed by the difference between the two linear operators of the accelerating and stopping actions:

$$V = V_A - V_B = L[f(t)] - L_{AB}[P(t)].$$

It is known from solving problems of forced oscillations of rods and slabs^{4,5} used to describe the behavior of punches and an impactor, that these operators have the form of simple convolutions linear with respect to a variable boundary condition. Thus, the Fourier transforms of the unknown velocity and constraints at the boundaries are linked by the simple linear relation:

$$V^F(\omega) = f^F(\omega) \cdot S(\omega) - P^F(\omega) \cdot S_{AB}(\omega),$$

which contains the frequency characteristics of the pressing instrument, S_ω and $S_{AB}(\omega)$, determined experimentally in two calibrating situations. Here the superscripts ‘‘F’’ indicate direct Fourier transformation.

In the first situation, there is no powder in the die block and the surfaces of the punches are brought into contact. Under the influence of an external force $f_1(t)$, the pressure $P_1(t)$ develops at the A–B contact interface but there is no relative displacement of surfaces A and B ($V(t) \equiv 0$). In the second situation, under the action of the force $f_2(t)$, the im-

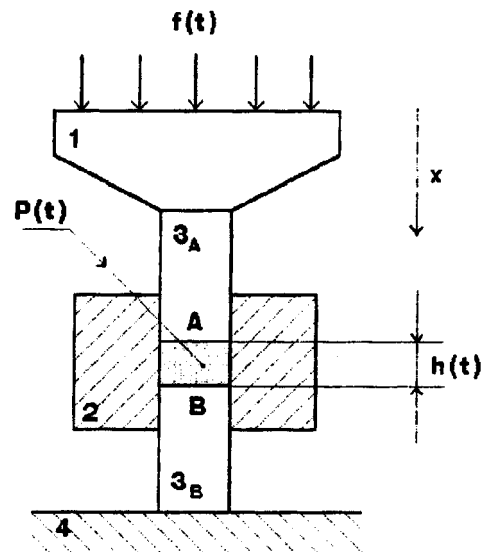


FIG. 1. Diagram of experiment to study dynamic compression of powders: 1 — impactor, 2 — die block, 3_A and 3_B upper and lower punches, and 4 — rigid support.

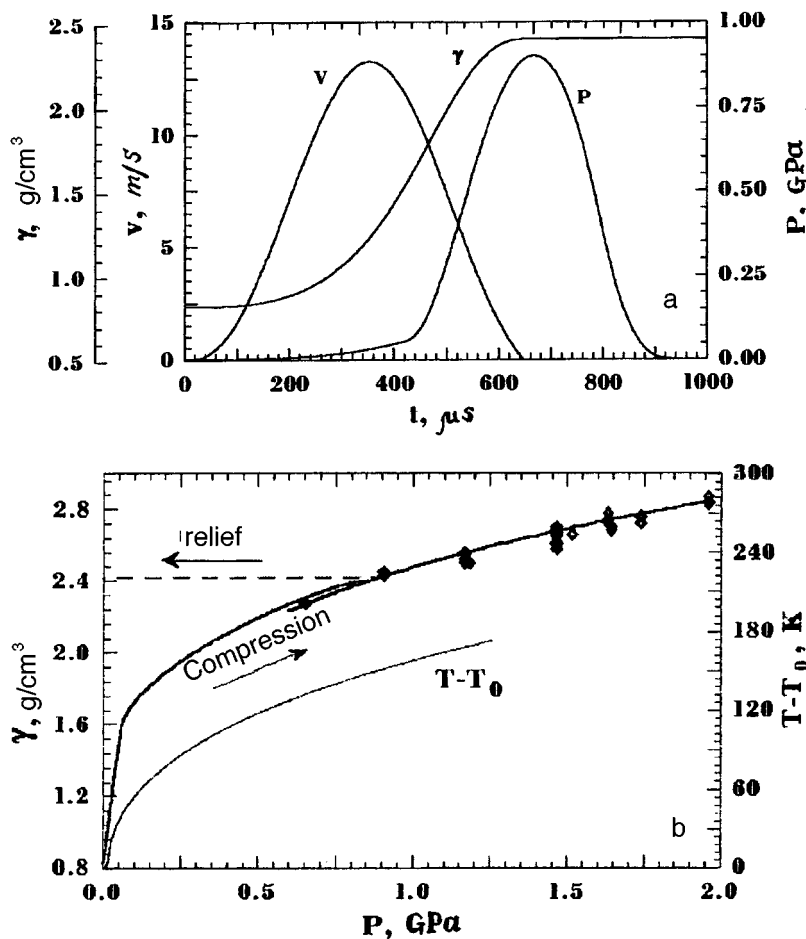


FIG. 2. Characteristics of uniaxial dynamic compression of Al_2O_3 nanopowder: a — time dependences of pressing pressure $P(t)$, punch approach velocity $V(t)$, and powder density $\gamma(t)$ in a single compression process; b — dynamic adiabatic curve of powder: solid curve — compression; dashed curve — pressure relief. The symbols give the points obtained in various tests. The curve $(T - T_0)$ gives the heating of the sample under adiabatic compression.

pactor and the upper punch undergo free acceleration ($P(t) \equiv 0$), and the punch velocity $V_2(t)$ is monitored. As a result, the unknown approach velocity of the punches as the powder is compressed is expressed as the inverse Fourier transform of a combination of spectral densities of two functions ($P(t)$ and $f(t)$), describing this process and four calibration functions ($f_1(t)$, $P_1(t)$, $f_2(t)$, $V_2(t)$) characterizing the instrument:

$$V(t) = F^{-1} \left\{ V_2^F \times \left[\frac{f^F}{f_2^F} - \frac{f_1^F \times P^F}{f_2^F \times P_1^F} \right] \right\}.$$

This method was used to investigate the dynamic compression of nanosize Al_2O_3 powder ($d = 20$ nm) obtained by electrical explosion in the laboratory of Yu. A. Kotov, Corresponding Member of the Russian Academy of Sciences (Institute of Electrophysics, Ural Branch of the Russian Academy of Sciences, Ekaterinburg). Figure 2a shows typical time dependences of the pressing pressure, punch approach velocity, and powder density for a single powder compression process. It can be seen that compaction of the powder is completed near the maximum of the pressure pulse and the pressure is relieved with almost no change in density. The instantaneous density and pressure determine parametrically the dynamic adiabatic curve of the powder $\gamma(P)$, which is given in explicit form in Fig. 2b. The solid curve gives the compression branch and the dashed curve gives the pressure relief branch. Satisfactory agreement is observed

between the compression adiabatic curve and the experimental points $\{P, \gamma\}$ (symbols) obtained in many separate tests on the pressure pulse amplitude and the final pressing density. The pulsed heating of the powder ($c_p = 775$ J/kg·K) was estimated from the adiabatic compression curve in the isentropic approximation:

$$\Delta T = \frac{1}{c_p} \cdot \int_{\gamma_0}^{\gamma_1} P \gamma^{-2} d\gamma,$$

and is given by the curve $(T - T_0)$ in Fig. 2b.

The proposed method can be recommended for studying the mechanisms of dynamic compaction of various types of powders and for real-time selection of their pressing conditions.

¹ V. Ivanov, Y. A. Kotov, O. H. Samatov, R. Boehme, H. U. Karow, and G. Schumacher, *Nanostruct. Mater.* **6**, 287 (1995).
² V. V. Ivanov, S. N. Pararin, A. N. Vikharev, R. Boehme, and G. Schumacher, in *Proceedings of the Fourth European Conference on Ceramics*, Italy, 1995, Vol. 2, pp. 169–176.
³ A. Munitz, Z. Livne, J. C. Rawers, and R. J. Fields, in *Proceedings of the Third International Conference on Nanostructured Materials*, Hawaii, 1996, p. 140.
⁴ V. Gol'dsmit, *Impact: Theory and Physical Properties of Impacting Bodies* [in Russian] (Construction Literature Publishers, Moscow, 1965).
⁵ O. Yu. Zhar'ii and A. F. Ulitko, *Introduction to the Mechanics of Nonsteady-State Oscillations and Waves* [in Russian] (Vysshaya Shkola, Kiev, 1989).

Translated by R. M. Durham

Nonequilibrium structural transitions as a mechanism of turbulence

O. B. Naïmark

Institute of Continuous Media Mechanics, Urals Branch of the Russian Academy of Sciences, Perm
(Submitted February 4, 1997)
Pis'ma Zh. Tekh. Fiz. **23**, 81–88 (July 12, 1997)

A possible mechanism for turbulence is proposed and substantiated for the first time, whereby turbulence is considered as a nonequilibrium transition in ensembles of defects of the microscopic shear type, which are treated as real defects in the molecular structure of liquids. A statistical foundation is given for the evolution equations for the tensor order parameter, which characterizes an ensemble of such defects and has the meaning of nonequilibrium fluctuations of the strain rate. The types of macroscopic fluctuation modes of the strain rate are determined as self-similar solutions of the evolution equations for this tensor order parameter under conditions of nonequilibrium transitions, and qualitative correspondences are established between these solutions and real scenarios for the transition to turbulence. The Kolmogorov scaling laws (the natures of the “viscous” and “inertial” intervals) are explained for fully developed turbulence. © 1997 American Institute of Physics.
[S1063-7850(97)01507-3]

Various experimental observations regarding the physical mechanisms for the evolution of instabilities in condensed media indicate that turbulence may be described on the basis of an analysis of nonequilibrium fluctuations, where the latter are considered as real defects in the structure of liquids. This Letter was inspired by the results reported by Yu. L. Klimontovich,^{1,2} who developed the concept of turbulence as a transition to “turbulent” order, and is also an attempt to formulate an opinion on the possible evolution of instabilities in condensed media as being a consequence of nonequilibrium transitions in ensembles of defects. These defects, being by their very nature “nonequilibrium fluctuations” of displacement (and velocity) fields in solids, are treated in liquids as real physical defects generated in the molecular structure by the collective motion of an ensemble of molecules (slip) which does not follow the usual diffusion (molecular) mechanism of momentum transfer.

Some data are presented to confirm the possibility of this treatment of velocity fluctuations induced by the dynamic instability of ensembles of molecules. One of the first to draw attention to the “solid-state” nature of liquid flow was Frenkel,³ who observed that “...the widely held view that the fluidity of liquids is caused by the absence of shear elasticity, i.e., by a zero shear modulus, is incorrect (except, possibly, for the case of liquid helium II).” The validity of this statement is confirmed by the results of measurements of the shear modulus and relaxation spectra of simple liquids,^{4,5} which yielded relaxation times $\tau \approx 10^{-5}$ s, differing by almost five orders of magnitude from the molecular (diffusion) times. The authors of Ref. 5 attribute the appearance of long-lived parts of the spectrum to coordinated displacement and reorientation of groups of molecules.

It is remarked in Ref. 2 that the approximation of a continuous medium, adopted in kinetic theory, is inadequate to describe turbulent motion in hydrodynamics. The nucleation and evolution of turbulent motion is caused by nonequilibrium fluctuations that grow as a certain transition point is approached. The statistical kinetics of an ensemble of typical

defects in solids (microcracks, microshears) was developed in Refs. 6 and 7. Microscopic shears are treated as nonequilibrium fluctuations of the strain rate in an incompressible fluid $e_{ik} = (1/2)(\partial v_i / \partial x_k + \partial v_k / \partial x_i)$, induced by cooperative displacement of groups of molecules. The microshears play the part of variables eliminating the loss of diffeomorphism (from the viewpoint of the theory of gauge fields⁸) in localized instabilities, and may be expressed as $s_{ik} = (1/2)s(\nu_i l_k + l_i \nu_k)$, where s is the shear intensity, and $\vec{\nu}$ and \vec{l} are the unit vectors of the normal to the area of shear and the direction of shear, respectively. The microscopic kinetics of s_{ik} is determined by the Langevin equation

$$\dot{s}_{ik} = K_{ik}(s_{lm}) - F_{ik}, \quad (1)$$

where $K_{ik}(s_{lm})$ and F_{ik} are the deterministic and random parts of the interaction forces, satisfying the conditions $\langle F_{ik}(t) \rangle = 0$ and $\langle F_{ik}(t') F_{ik}(t) \rangle = Q \delta(t - t')$, where Q is the correlation function of the fluctuating forces (nonequilibrium potential). The distribution function of the shear fluctuations $W(s, \vec{\nu}, \vec{l})$ corresponds to the solution of the Fokker–Planck equation

$$\frac{\partial}{\partial t} W = - \frac{\partial}{\partial s_{ik}} (K_{ik} W) + \frac{1}{2} Q \frac{\partial^2}{\partial s_{ik} \partial s_{ik}} W. \quad (2)$$

It was shown in Ref. 6 that the Lagrangian of these structural defects, modeled as dislocation pileups, may be written as

$$E = E_0 - H_{ik} s_{ik} + \alpha s_{ik}^2, \quad (3)$$

which includes the “traditional” term $H_{ik} s_{ik}$, describing the interaction in an ensemble in the “mean” field approximation⁹ ($H_{ik} = \gamma \sigma_{ik} + \lambda p_{ik}$, where σ_{ik} is the stress, $p_{ik} = n \langle s_{ik} \rangle$, n is the defect concentration, and λ and γ are parameters of the material), and the “self-action” αs_{ik}^2 , describing the energy fluctuation in the nearest neighborhood of the defect. A solution of the Fokker–Planck equation was obtained in Ref. 10 as a consequence of the hypothesis of

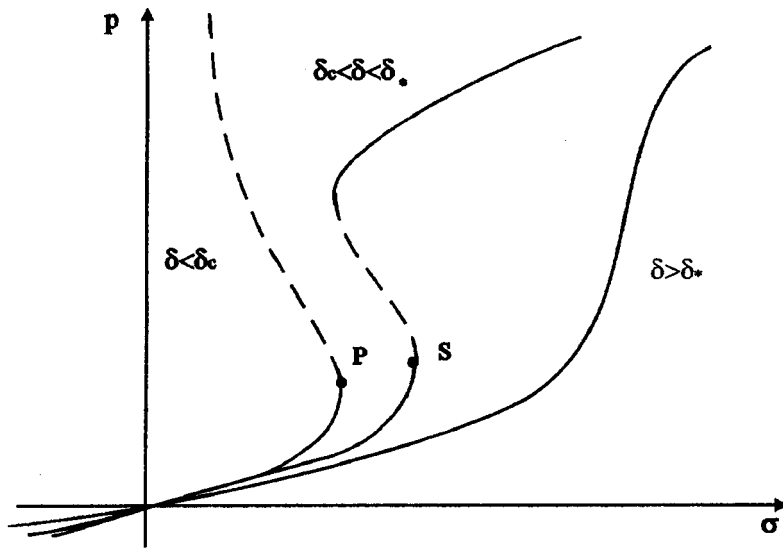


FIG. 1. Macroscopic fluctuations of the shear p versus stress σ .

statistical self-similarity (which was confirmed experimentally for an ensemble of defects in Ref. 11), which allowed the nonequilibrium distribution function to be expressed in the form $W = Z^{-1} \exp(-E/Q)$, where Z is a normalizing factor calculated as a generalized value of the partition function. The quasiequilibrium distribution function essentially reflects the view as to the nature of nonequilibrium developed by Leontovich,¹² as a sequence of equilibrium states generated under the action of effective fields, whose magnitude in this case depends on Q . The possibility of describing laminar and turbulent motion and transitions between them using a “deterministic distribution” is also discussed in Ref. 2.

The macroscopic value of the “steady-state” nonequilibrium fluctuations of the shear p_{ik} is calculated as an average,⁶

$$p_{ik} = n \int s_{ik} W(s, \vec{v}, \vec{l}) ds d^3 v d^3 \vec{l}, \quad (4)$$

and its value $p_{xz} = p$ for the case of pure shear of an infinite layer by the stress $\sigma_{xz} = \sigma$ is plotted in Fig. 1 in the form of curves for different values of the parameter $\delta = 2\alpha/\lambda n$. The quantity δ characterizes the interaction in the ensemble (λ is the interaction constant) and how the defect size is influenced by the initial “free volume” V_0 , which functions as a defect nucleus (assuming $\alpha \approx G/V_0$, where G is the shear modulus). Transitions to topologically equivalent classes of curves are determined by the parameters δ_* and δ_c , which are bifurcation points.

The nonequilibrium free energy F reflecting the entire spectrum of realizations in Fig. 1 may be expressed by the expansion⁷

$$F = 1/2A(1 - \delta/\delta_*)p_{ik}^2 + 1/3Bp_{ik}^4 + 1/4C(1 - \delta/\delta_c)p_{ik}^6 - D\sigma_{ik}p_{ik} + 1/2\mu(\nabla p_{ik})^2, \quad (5)$$

where A , B , C , and D are the expansion parameters. Assuming that the defect interaction is “polar,” the gradient term describes nonlocal effects, and μ is the nonlocality parameter. The “thermodynamic” branches correspond to minima

of F that give steady-state regimes. The coordinates $P(\sigma_p, p_p)$ and $S(\sigma_s, p_s)$ are the points of transition to the dynamic branches.

The fact that the dissipative function TP_s of a relaxing (by flow) medium with defects does not change sign¹³

$$TP_s = -\frac{1}{T}q_k \nabla_k T + \sigma_{ik} e_{ik}^v - \frac{\delta F}{\delta p_{ik}} \dot{p}_{ik} \geq 0 \quad (6)$$

(T is the temperature, q_k is the heat flux, $\delta F/\delta p_{ik}$ is a variational derivative, and e_{ik}^v is the “viscous” component of the total strain rate $e_{ik} = e_{ik}^v + \dot{p}_{ik}$) leads to a system of equations for the tensor quantities

$$\sigma_{ik} = \eta e_{ik}^v + \chi \dot{p}_{ik}, \quad -\frac{\delta F}{\delta p_{ik}} = -\chi e_{ik}^v + \zeta \dot{p}_{ik}, \quad (7)$$

where η , χ , and ζ are kinetic coefficients. Taking $e_{xz}^v = e_{xz} - \dot{p}_{xz}$ for the case of pure shear, these equations give an expression for the effective viscosity $\eta_{ef} = \eta + (\chi - \eta)\dot{p}_{xz}/e_{xz}$ and a kinetic equation for p_{xz} .

The presence of bifurcation points indicates a sudden change in the symmetry of the distribution function, caused by the appearance of various orientationally defined macroscopic modes p_{ik} during structural transitions. The influence of these modes on the evolution of nonequilibrium fluctuations of the strain rate is determined by the type of bifurcation (by the group properties of the equations in various intervals δ) and by the form of the heteroclines and their corresponding natural forms¹⁰ (Fig. 2). The interval $\delta > \delta_*$ (elliptic region S_1) corresponds to spatially periodic solutions with weakly defined orientational anisotropy which does not fundamentally alter the laminar flow pattern. Passages through the thresholds δ_* (hyperbolic region S_2) and δ_c (parabolic region S_3) lead to the evolution of nonequilibrium fluctuations of the strain rate in the form of spectra of solitary waves and dissipative structures with explosive growth kinetics (peaking regimes¹⁴) of various components p_{ik} , respectively. The peaking regimes correspond to a strange attractor region and give rise to dynamic stochastic-

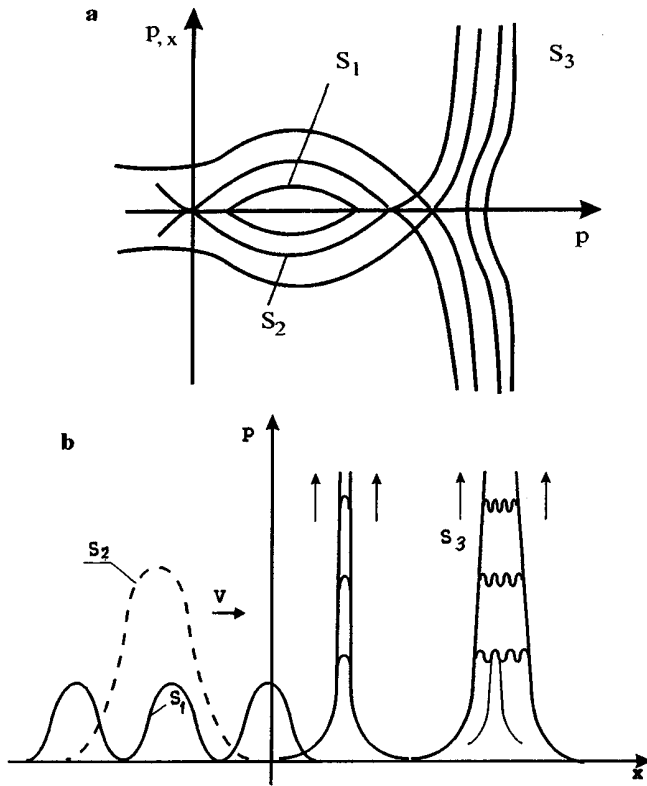


FIG. 2. Phase portrait of nonequilibrium shear fluctuations (a) and corresponding spectra of natural forms of the self-similar solutions (b).

ity effects. Intermittence effects should be observed in the region of coexistence of attractors (in the vicinity of $\delta = \delta_c$). Movement of the system to the last two types of attractors severely reduces the symmetry of the system as a result of a reduction in the number of independent variables, which are determined in this case by the spectra of natural forms of the corresponding self-similar solutions.

A resonant transition to self-similar solutions¹⁵ under conditions of nonequilibrium structural transitions is accompanied by adiabatic subjection of the corresponding tensor modes of the strain rate e_{xz} to the nonequilibrium macroscopic fluctuation \dot{p}_{xz} and thus $e_{xz} \approx \dot{p}_{xz}$, which gives the effective viscosity $\eta_{ef} = \chi$. Values of the viscosity $\eta_{ef} \approx 10^4$ P, independent of the type of condensed medium, were determined in Ref. 16 from the damping of perturbations at a shock wave front in steel, aluminum, mercury, and water at strain rates of $\sim 10^5$ s⁻¹. This surprising result is also observed in a similar range of strain rates for the impact initiation of plastic instability (adiabatic shear¹⁷). Advanced turbulence corresponds to the range $\delta < \delta_c$ to which a transition takes place from the laminar region $\delta > \delta_*$ via the

region of spatially periodic flow $\delta_c < \delta < \delta_*$, as the flow intensity increases and “defect” structures are created, renormalizing (reducing) δ . When the turbulence is fully developed, the flow is subject to the spectrum of natural forms (dissipative structures in the peaking regime) which describe the explosive growth kinetics of various tensor modes of the nonequilibrium fluctuations of the strain rate, determined by the corresponding components p_{ik} and localized on the spectrum of spatial scales (fundamental lengths¹⁴). The minimum scale corresponding to a simple structure clearly determines the lower boundary of the inertial interval (the upper boundary of the viscous interval) in accordance with the Kolmogorov hypothesis.

The author would like to thank V. A. Barannikov for supportive discussions.

¹ Yu. L. Klimontovich, *Turbulent Flow and Structure of Chaos* [in Russian] (Nauka, Moscow, 1990).

² Yu. L. Klimontovich, *Izv. Vyssh. Uchebn. Zaved. Prob. Nelin. Dinam.* 3(2), 7 (1995).

³ J. Frenkel, *Kinetic Theory of Liquids* (Clarendon Press, Oxford, 1946) [Russ. original, Nauka, Leningrad, 1975].

⁴ B. B. Badmaev, K. T. Zandanova, O. R. Budaev, B. V. Deryagin, and U. B. Bazarov, *Dokl. Akad. Nauk SSSR* 254, 381 (1980).

⁵ B. V. Derjaguin, U. B. Bazarov, K. T. Zandanova, and O. R. Budaev, *Polymer* 30, 96 (1989).

⁶ O. B. Naïmark, *Thermodynamics of Deformation and Fracture of Solids with Microcracks*, Preprint [in Russian], Institute of Continuous Media Mechanics, Urals Branch of the Russian Academy of Sciences., Perm (1982).

⁷ O. B. Naïmark, *Structural Transitions in Solids and Mechanisms of Plasticity and Failure*, Preprint, Institute of Continuous Media Mechanics, Urals Branch of the Russian Academy of Sciences, Perm (1995).

⁸ E. Kröner, *On Gauge Theory in Defect Mechanics*, Lecture Notes in Physics (Springer-Verlag, Berlin 1986), pp. 281–296.

⁹ Yu. L. Raikher and M. I. Shliomis, *Relaxation Phenomena in Condensed Matter*, Advances in Chemical Physics, Vol. LXXXVIII, edited by W. Coffey, (1994), p. 595–751.

¹⁰ O. B. Naïmark, *Kinetic Transitions in Ensembles of Defects (Microcracks) and Some Nonlinear Aspects of Fracture*, in *Proceedings of the IUTAM Symposium on Nonlinear Analysis of Fracture* (Kluwer, The Netherlands, 1995).

¹¹ L. R. Botvina and G. I. Barenblatt, *Prob. Prochnosti* No. 12, 17 (1985).

¹² M. A. Leontovich, *Introduction to Thermodynamics: Statistical Physics* [in Russian], Nauka, Moscow (1983).

¹³ O. B. Naïmark and O. V. Ladygin, *Zh. Prikl. Mekh. Tekh. Fiz.* No. 3, 121 (1993).

¹⁴ S. P. Kurdyumov, *Eigenfunctions for Combustion of a Nonlinear Medium and Design Laws for Constructing its Organization*, Preprint No. 29 [in Russian], M. V. Keldysh Institute of Applied Mathematics, Academy of Sciences of the USSR, Moscow (1979).

¹⁵ A. D. Sakharov, R. M. Zaïdel', V. N. Mineev, and A. G. Oleïnik, *Dokl. Akad. Nauk. SSSR* 9, 1091 (1961).

¹⁶ V. V. Belyaev and O. B. Naïmark, *Dokl. Akad. Nauk. SSSR* 312, 289 (1990) [*Sov. Phys. Dokl.* 35, 436 (1990)].

¹⁷ V. V. Belyaev and O. B. Naïmark, *Zh. Prikl. Mekh. Tekh. Fiz.* No. 1, 163 (1985).

Translated by R. M. Durham

Transition to chaotization and loss of self-averaging in two-dimensional two-phase media at the flow threshold

S. P. Luk'yanets, A. E. Morozovskii, and A. A. Snarskii

*Institute of Physics, Ukrainian National Academy of Sciences, Kiev;
Ukraine National Technical University—"Kiev Polytechnic Institute," Kiev*
(Submitted March 26, 1997)

Pis'ma Zh. Tekh. Fiz. **23**, 89–95 (July 12, 1997)

Giant fluctuations of the electric field recently identified experimentally in two-dimensional two-phase media at the percolation threshold are discussed. An example of a hierarchical realization of these media is used to show that for $\text{Re } \sigma_i = 0$ (where σ_1 and σ_2 are the phase conductivities) and $\text{Im } \sigma_2 / \text{Im } \sigma_1 > 0$, the hierarchy construction procedure yields the Dykhne expression $\sigma_e = \sqrt{\sigma_1 \sigma_2}$, whereas for $\text{Im } \sigma_2 / \text{Im } \sigma_1 < 0$, the procedure becomes randomized and the medium loses its property of self-averaging. © 1997 American Institute of Physics. [S1063-7850(97)01607-8]

In Ref. 1 an expression was derived for the effective conductivity σ_e of a two-dimensional two-phase medium with the average geometrically equivalent phase distribution

$$\sigma_e = \sqrt{\sigma_1 \sigma_2}, \quad (1)$$

where σ_i are the local conductivities of the phases with the concentration $p = 0.5$. In particular, these media (Dykhne media) include those at the flow threshold.

It has recently been shown in various studies²⁻⁹ that for $\text{Re } \sigma_1 = 0$ and $\text{Re } \sigma_2 \ll \text{Im } \sigma_2$ giant fluctuations of the local electric field are observed in these media. In particular, this implies that the modulus of the electric field is not averaged over dimensions of the order of the standard correlation length (see the experiment reported in Ref. 4). In Ref. 6, the authors put forward the idea that a renormalization group mapping for complex impedances with low local losses leads to a dynamic chaos scenario and a fractal dependence of the impedance for hierarchical chains.

Examples of a hierarchical construction of a medium with a geometrically equivalent phase distribution are given in Refs. 7 and 8. Using the approach adopted in Ref. 8 and considering the limiting case $\text{Re } \sigma_2 = \text{Re } \sigma_1 = 0$, we show that, depending on the sign of $h = \text{Im } \sigma_2 / \text{Im } \sigma_1$, the medium will exhibit fundamentally different properties. For $h > h_c = 0$, the medium is self-averaging and the effective conductivity is determined (as should be the case) by the Dykhne formula (1). When $h < h_c = 0$, however, the medium loses its self-averaging property and it is difficult to introduce effective kinetic coefficients.

According to Ref. 8, at the first step the medium "is assembled" from strips of equal thickness with the conductivities σ_1 and σ_2 (Fig. 1a). Making the thickness of the strips tend to zero — homogenizing the medium — we obtain a single crystal for which the principal components of the conductivity tensor are $\sigma_{\parallel}(1)$ and $\sigma_{\perp}(1)$ (Fig. 1b). Then, by cutting strips of equal thickness lengthwise and crosswise to this crystal, we collect these together to form a new single crystal (Fig. 1c) for which the principal components of the conductivity tensor are $\sigma_{\parallel}(2)$ and $\sigma_{\perp}(2)$. It is easy to show that at each stage

$$\sigma_{\perp}(n+1) = (\sigma_{\perp}(n) + \sigma_{\parallel}(n))/2,$$

$$\sigma_{\perp}(n+1) = 2\sigma_{\perp}(n)\sigma_{\parallel}(n)/(\sigma_{\perp}(n) + \sigma_{\parallel}(n)). \quad (2)$$

Note that the numerical coefficients in Eq. (2) appear as a result of normalizing to the geometric dimensions of the total conductance of a medium with a large (in the limit unbounded) number of strips. The iteration procedure (2) has the invariant:

$$\sigma_{\perp}(n)\sigma_{\parallel}(n) = \sigma_1\sigma_2 = a, \quad (3)$$

and allowing for this, formula (2) may be written as:

$$\sigma_{\perp}(n+1) = (\sigma_{\perp}(n) + a/\sigma_{\perp}(n))/2, \quad \sigma_{\parallel}(n) = a/\sigma_{\perp}(n). \quad (4)$$

It is easy to show⁸ that for real $\sigma_1 > 0$ and $\sigma_2 > 0$, when $n \rightarrow \infty$ we arrive at expression (1) for the effective conductivity of the medium.⁷ In fact, the map (4) has a fixed stable point $\sigma_{\parallel}(\infty) = \sigma_{\perp}(\infty) = \sigma_e = \sqrt{\sigma_1\sigma_2}$. For large n , $\sigma_{\perp}(n)$ has the form $\sigma_{\perp}(n) \approx \sqrt{\sigma_1\sigma_2} \cdot [1 + 0.5(\sigma_1/\sigma_2 - 1)\exp(-n)]$, which suggests that the procedure converges rapidly (Fig. 2a).

We investigate Eq. (4) for purely imaginary values of σ_1 and σ_2 and we show that under certain conditions the procedure loses the fixed points and stable cycles and the sequence $\sigma_{\parallel}(n)$ and $\sigma_{\perp}(n)$ becomes chaotic. This implies that the medium obtained by this procedure is non-self-averaging. For purely imaginary $\sigma_1 = i\tilde{\sigma}_1$ and $\sigma_2 = i\tilde{\sigma}_2$, the elements of the sequence determined by the procedure (4) will also be imaginary $\sigma_{\perp}(n) = i\tilde{\sigma}_{\perp}(n)$, $\sigma_{\parallel}(n) = i\tilde{\sigma}_{\parallel}(n)$. The iteration procedure for $\tilde{\sigma}_{\parallel}(n)$ and $\tilde{\sigma}_{\perp}(n)$ has the same form as Eq. (4) where a is now replaced by $\tilde{\sigma}_1\tilde{\sigma}_2$.

Two cases should be distinguished:

1. $\tilde{\sigma}_1\tilde{\sigma}_2 > 0$ (i.e. $\tilde{\sigma}_1$ and $\tilde{\sigma}_2$ have the same sign, for example, the elements of the first and second phases are capacitances whose resistances can be neglected). In this situation, we arrive at the same result as for real σ_1 and σ_2 . The procedure has stable fixed points and the effective conductivity is given by

$$\sigma_e = \sigma_{\perp}(\infty) = \sigma_{\parallel}(\infty) = \begin{cases} i\sqrt{\tilde{\sigma}_1\tilde{\sigma}_2}, & \tilde{\sigma}_1 > 0, \tilde{\sigma}_2 > 0 \\ -i\sqrt{\tilde{\sigma}_1\tilde{\sigma}_2}, & \tilde{\sigma}_1 < 0, \tilde{\sigma}_2 < 0. \end{cases} \quad (5)$$

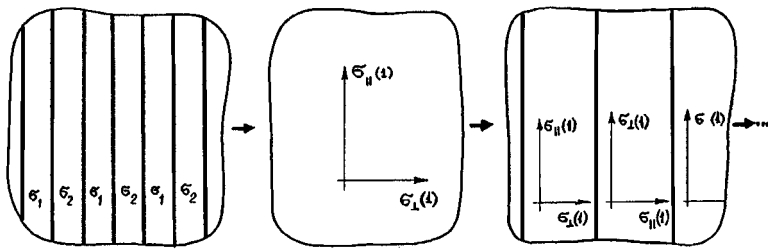


FIG. 1. Procedure for successive construction of a hierarchical Dykhne medium.

2. $\tilde{\sigma}_1 \tilde{\sigma}_2 < 0$ (i.e., $\tilde{\sigma}_1$ and $\tilde{\sigma}_2$ have different signs, the elements of the first phase are capacitances and those of the second phase are inductances whose resistances can be neglected). In this case, for the map defined by formula (4) no fixed points or stable cycles exist. It follows directly from formula (4) that for $\tilde{\sigma}_1 \tilde{\sigma}_2 < 0$ the components $\tilde{\sigma}_{\parallel}(n)$ and $\tilde{\sigma}_{\perp}(n)$ have different signs for any n . This implies that in this case, the medium does not become isotropic. For convenience we cast Eq. (4) in the dimensionless variables $x_n = \tilde{\sigma}_{\perp}(n)/|\tilde{\sigma}_1|$ and $y_n = \tilde{\sigma}_{\parallel}(n)/|\tilde{\sigma}_1|$ and then rewrite it as:

$$x_{n+1} = (x_n + h/x_n)/2, \quad y_n = h/x_n. \quad (6)$$

Here $h = \tilde{\sigma}_2/\tilde{\sigma}_1$. Now the initial value is $x_0 = \pm 1$ and the parameter defining the different media is h . The behavior of the iteration sequence (6) for different h is shown in Fig. 2. For $h > 0$, the sequence x_n converges to the fixed stable point x_{∞} (Fig. 2a). When h becomes negative the sequence ceases to converge, and as h decreases, it increasingly acquires the characteristic features of chaotic behavior (Figs. 2b, 2c, and 2d). In fact, the procedure (6) leads to chaotic dynamics; that is, for the map (4) $N(z) = (z^2 + a)/2z$ ($a = \sigma_1 \sigma_2$ is positive

and real) the Julia set J_N separating the basins of attractions of the stable fixed points $\pm \sqrt{a}$ coincides with the imaginary axis.⁹ On J_N , formula (4) induces a one-dimensional map, which converges to (6) and determines the dynamics on the Julia set. The map (4) is conjugate with the map $R(u) = u^2$ obtained by substituting $u = (z + \sqrt{a})/(z - \sqrt{a})$. Then, the imaginary axis (Julia set) is converted into a single circle on which the dynamics is defined by the map $r(\theta) = 2\theta \pmod{1}$, which is known to generate chaotic dynamics.^{9,10}

Qualitatively, the behavior of x_n as a function of n may be explained by using a graph of the mapping function $f(x) = (x + h/x)/2$, which determines the iteration procedure (Fig. 3). Figure 3a shows the iteration sequence and its convergence to the fixed stable point \sqrt{h} for $h > 0$. For fairly small negative h (Fig. 3b), the sequence x_n initially decreases monotonically to zero ($f(x) \approx x/2$, $|h| \ll |x|$), but near zero the map has a ‘‘dip’’ ($f(x) \approx -|h|/2x$, $|x| \ll |h| \ll 1$) as a result of which the sequence ceases to be monotonic, changes sign, and after a certain number of iterations, returns to the region of high (compared with $|h|$) values and again

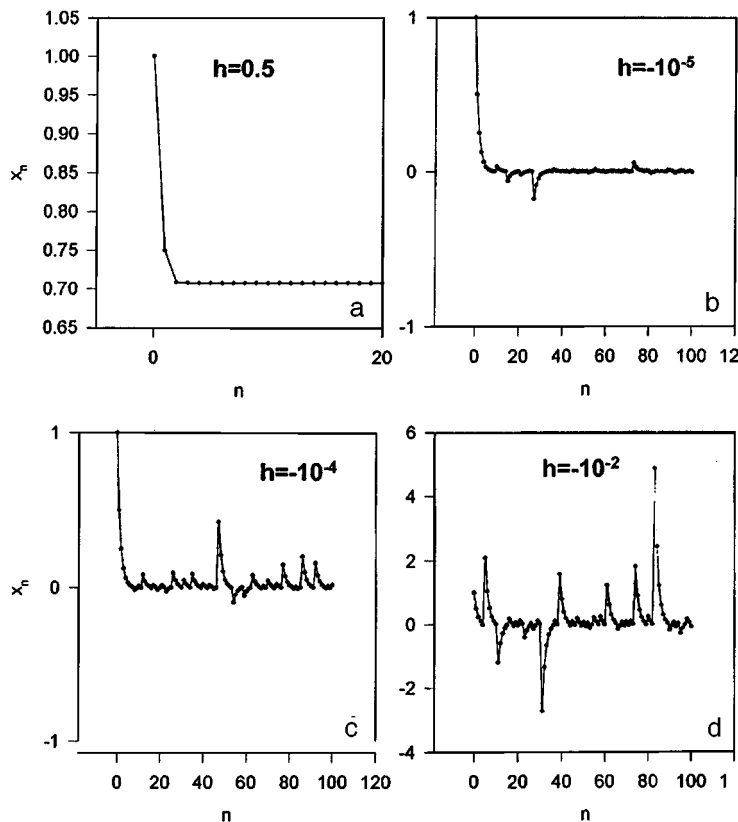


FIG. 2. Behavior of the iteration sequence (6) when the purely imaginary values of the phase conductivity have the same sign $h = \tilde{\sigma}_2/\tilde{\sigma}_1 > 0$ (a). Chaotic behavior of the iteration procedure for $h < 0$ (b, c, d).

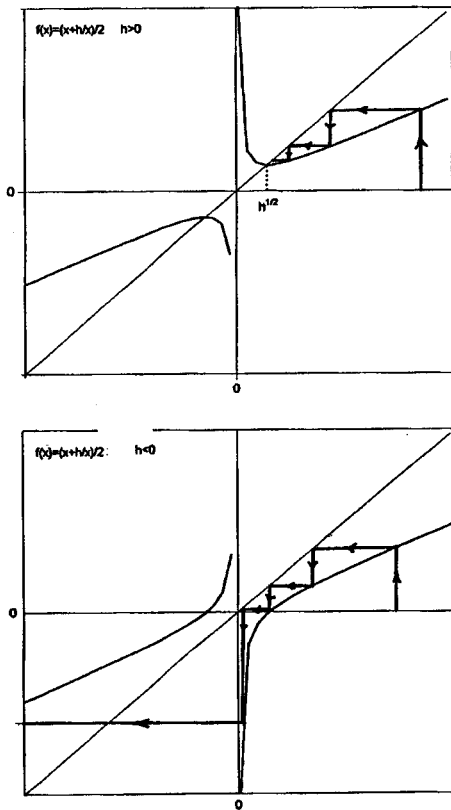


FIG. 3. Convergence of the iteration procedure with the mapping function $f(x) = (x+h/x)/2$ to the fixed stable point \sqrt{h} for $h > 0$ (a). Loss of stability of the iteration procedure for $h < 0$ (b).

begins to tend monotonically to zero. As h decreases further, the dip near zero increases, leading to a reduction in the intervals of monotonicity and an increase in the irregular regions and amplitudes of x_n .

This procedure can also be used to obtain the spectrum of resonant frequencies determined by the set of values $h = \tilde{\sigma}_2 / \tilde{\sigma}_1$, whose number increases with the iteration step n as 2^n for which the procedure (6) diverges.

To sum up, this example of one of the possible realizations of Dykhne media with a hierarchical structure has

shown that for certain values of the phase conductivities, a medium, while geometrically remaining a Dykhne medium (two-dimensional, two-phase, geometrically equivalent phase distribution), loses its property of self-averaging in terms of physical properties and thereby loses the concept of effective kinetic coefficients.

It is disputable whether other possible procedures leading to Dykhne media lose the property of self-averaging and whether the "usual" checkerboard realization of a Dykhne medium loses its property of self-averaging.

We would like to thank É. M. Baskin and M. V. Éntin for discussions on the absence of self-averaging in the effective properties of weakly absorbing media and M. V. Éntin for allowing us to become acquainted with Ref. 6 prior to publication and for fruitful discussions of this work, which improved our understanding of the issues raised. We would also like to thank V. Yarmol'nik for assistance with the numerical calculations.

This work was partially supported by grants from the Russian Fund for Fundamental Research No. 950204432 and from "Nauka-Servis" No. 1-200-96.

¹A. M. Dykhne, Zh. Éksp. Teor. Fiz. **59**, 110 (1970) [Sov. Phys. JETP **32**, 63 (1970)].

²F. Brauers, S. Blacher, and A. K. Sarychev, in *Fractal Reviews in the Natural and Applied Sciences*, edited by M. Novak (Chapman and Hall, London, 1995).

³F. Brauers, S. Blacher, N. Henriouille, and A. K. Sarychev, *Abstracts of the Fourth International Conference on Electrical Transport and Optical Properties of Inhomogeneous Media, ETOPIM4*, Moscow, 1996, p. 46 [submitted to J. Phys. A].

⁴A. N. Lagarkov, K. V. Rozanov, and A. K. Sarychev, *ibid*, p. 59.

⁵É. M. Baskin, M. V. Éntin, A. K. Sarychev, and A. A. Snarskiĭ, in press.

⁶M. V. Éntin, and G. M. Éntin, Pis'ma Zh. Éksp. Teor. Fiz. **64**, 427 (1996) [JETP Lett. **64**, 467 (1996)].

⁷K. J. Schulgaser, J. Phys. C **10**, 407 (1977).

⁸A. E. Morozovskii and A. A. Snarskiĭ, Ukr. Fiz. Zh. **28**, 1230 (1983).

⁹H. O. Peitgen and P. H. Richter, *Beauty of Fractals. Images of Complex Dynamical Systems* (Springer-Verlag, Berlin, 1985) [Russ. transl., Mir, Moscow, 1993].

¹⁰H. G. Schuster, *Deterministic Chaos* (Physik-Verlag, Weinheim, 1984) [Russ. transl., Mir, Moscow, 1988].

Translated by R. M. Durham

Use of a two-wire microwave line at the boundary of the investigated zone to measure the electron density in a low-temperature plasma

A. D. Zuev and A. G. Smolin

A. F. Ioffe Physicotechnical Institute, Russian Academy of Sciences, St. Petersburg
(Submitted September 13, 1996)

Pis'ma Zh. Tekh. Fiz. **23**, 1–7 (July 26, 1997)

A new method based on a two-wire line has been developed for noncontact diagnostics of a low-temperature plasma and its fluxes in channels with complex profiles. This method provides good spatial and time resolution. © 1997 American Institute of Physics.
[S1063-7850(97)01707-2]

The use of a two-wire microwave line can substantially improve the spatial resolution in measurements of the plasma electron density as compared with free-space methods. This property of a two-wire line was utilized in Ref. 1, where the conductors passed through a layer of plasma more than three wavelengths thick ($\lambda = 3$ cm), which allowed accurate measurements to be made in a quiescent plasma or in a plasma moving slowly relative to the conductors. However, this configuration of conductors in a two-wire line cannot be used for diagnostics of ultrasonic fluxes because of the perturbations introduced by the measuring line in the flux being investigated and because the line is deformed by the incoming flux. A diagnostic technique based on a two-wire microwave line as a probe element is proposed for diagnostics of a low-temperature plasma and its fluxes in channels of complex profile, without perturbing the flux by the elements of the measuring system. In this technique the conductors of the two-wire line run through the material of the channel walls (Teflon-4 insulator) in the direction in which the plasma parameters are uniform. According to the experiments and calculations, the spatial resolution is then approximately 1 cm (at $\lambda = 3$ cm). With this line configuration, the method can even be used when the channel walls are close together.

The proposed method was implemented, checked out experimentally, and used on an experimental apparatus comprising a disc MHD channel connected to a shock tube.² A flux of ionized plasma was generated in the shock tube and then supplied to the disc channel via a distributor nozzle. The channel walls were made of Teflon, the channel height was 1 cm, and the outer radius of the discs was 15 cm. The conductors of the microwave measuring line were embedded at a depth $h = 0.5$ mm in the inner wall of the outer disc, along

arcs of circles with radii of 82.5 and 90 mm (Fig. 1). The length of the measuring section of the microwave line was $S = 15$ cm.

The electron density was also determined independently of the microwave method to check the proposed method experimentally and to calibrate the apparatus. These measurements were made under the same conditions by a well-known electromagnetic method which involved measuring the current induced by the motion of the plasma in a transverse magnetic field.² The measurements were made in mixtures of xenon and nitrogen under conditions where no additional ionization was produced by the induced electric field. Some of the results are presented in Table I.

The proposed microwave method utilizes the fact that the attenuation constant of electromagnetic waves propagating in the two-wire line depends on the electron density. We calculated this dependence for our conditions using information from Refs. 3 and 4. Since the distance h is small compared with L , each conductor in the line above the conducting layer can approximately be considered separately, with the influence of the other conductor neglected. The validity of this approximation was justified in Ref. 3, where a strict formulation of the problem was used to analyze the propagation of electromagnetic waves along a single wire and along a multi-wire line located above a plane uniform conducting surface. These authors also derived an equation to determine the (complex) propagation constant q along the wire as a function of the properties (permittivity, magnetic permeability, conductivity) of the wire, the insulator, and the conducting layer, which is valid ($L \gg a$, $L \gg h$) to a high degree of accuracy for a two-wire line (as a first approximation),

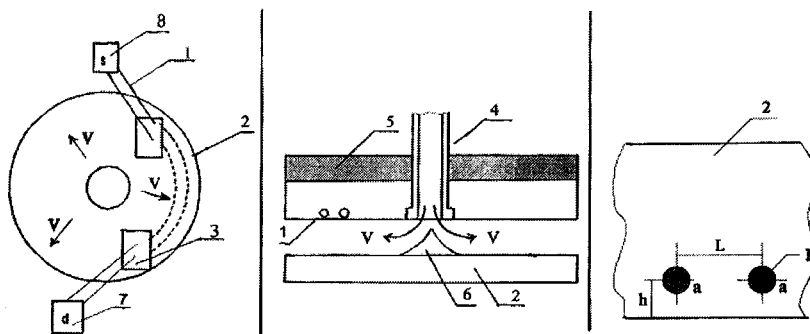


FIG. 1. Arrangement of conductors of two-wire line in disc MHD channel. 1 — conductors of two-wire line, 2 — discs of MHD channel (made of Teflon-4), 3 — seals, 4 — inlet pipe, 5 — microwave radiation absorbing rubber, 6 — plasma distributor, 7 — detector, and 8 — oscillator.

TABLE I. Results of experimental verification of the proposed method using mixtures of xenon and nitrogen (90% Xe + 10% nitrogen in the low-pressure chamber of a shock tube) at Mach numbers of the order of 3.5.

Experiment No.	Frequency ν of electron collisions with heavy component, s^{-1}	Electron density obtained from electromagnetic measurements, cm^{-3}	Electron density determined by microwave method, using results of electromagnetic calibration of the microwave method, cm^{-3}
1	5.1×10^{10}	$(6.0 \pm 0.4) \times 10^{11}$	$(5.7 \pm 0.5) \times 10^{11}$
2	3.2×10^{10}	$(5.5 \pm 0.4) \times 10^{11}$	
3	2.4×10^{10}	$(5.9 \pm 0.4) \times 10^{11}$	
4	2.0×10^{10}	$(5.4 \pm 0.4) \times 10^{11}$	

$$m_2(H_0(m_2a) - H_0(2m_2h))/H_0'(m_2a) = 2Fm_1/m_2\pi i H_0'(m_2a) + J_0(m_1a)/\varepsilon_1' J_0'(m_1a), \quad (1)$$

where $J_0(\xi)$ and $H_0(\xi)$ are zero-order Bessel and Hankel functions of the first kind,

$$F = 2\varepsilon_2' \int_0^\infty \frac{\eta_2 \eta_3 - \nu^2}{\varepsilon_3' \eta_2 + \varepsilon_2' \eta_3} \exp(-2\eta_2 h) d\nu,$$

$$\eta_j = \sqrt{\nu^2 - m_j^2}, \quad \text{Re}(\eta_j) > 0,$$

$$m_j = \sqrt{k_j^2 - q^2}, \quad \text{Im}(m_j) > 0, \quad k_j = (\omega/c) \cdot \sqrt{\varepsilon_j' \mu_j},$$

$$\text{Im}(k_j) > 0, \quad \varepsilon_j' = \varepsilon_j - (4\pi i \sigma_j / \omega),$$

ε_j' is the complex permittivity, ε_j is the permittivity, σ_j is the conductivity, and the subscripts 1, 2, and 3 refer to the conductor, the insulator, and the plasma, respectively.

Since Eq. (1) was transformed in Ref. 2 to obtain a comparatively simple formula to determine q for a different frequency interval, the propagation constant was calculated from Eq. (1) by the method of successive approximations. The calculated curves $\varepsilon_3(\sigma_3)$ obtained for different values of the absorption and the parameters of our apparatus are plotted in Fig. 2.

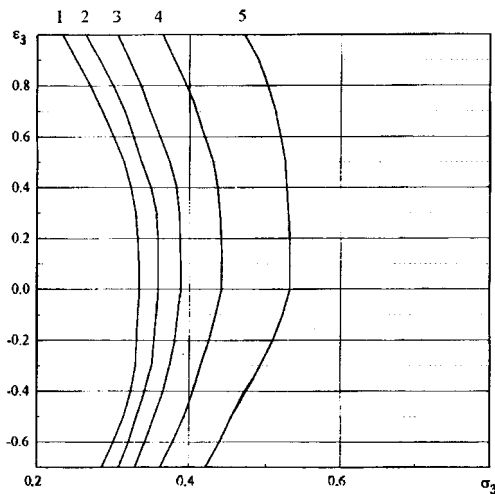


FIG. 2. Calculated curves $\varepsilon_3(\sigma_3)$ for various attenuations, characterized by the ratio of the squares of the electric field strengths in the detector E^2/E_0^2 (E and E_0 are the electric fields with and without plasma in the channel, respectively), 1 — $E^2/E_0^2 = 0.99$, 2 — 0.8, 3 — 0.6, 4 — 0.4, and 5 — 0.2.

The relation between the high-frequency conductivity and the permittivity of the plasma is determined by⁴

$$\varepsilon_3 = 1 - \sigma_3 / \varepsilon_0 \nu, \quad (2)$$

$$\sigma_3 (e^2 n_e \nu / m_e) (\omega^2 + \nu^2)^{-1}, \quad (3)$$

where ν is the effective electron collision frequency, n_e is the electron density, and m_e is the electron mass. Where the two straight lines (2) for $\varepsilon_3(\sigma_3)$ for the minimum and maximum values of $\nu = 2 \times 10^{10} - 5 \times 10^{10} s^{-1}$ intersect the two calculated curves $\varepsilon_3(\sigma_3)$ from Eq. (1) at attenuation coefficients of 0.99 and 0.6, an area bounded by these curves is obtained. According to formula (3), the electron density within this area varies in the range $(1.5 - 2.0) \times 10^{12} cm^{-3}$. It can be seen from these calculations that when the signal is attenuated to 0.6 (weak attenuation), because of the closeness of the curves, the electron density thus determined depends weakly on the frequency ν and fluctuations of the attenuation in the range 0.99–0.6 (for these parameters of the line). This assumption is accurately confirmed by making a comparison with the results obtained by the electromagnetic method. The calculations were made for the worst-case embedding depth, $h_{max} = 0.57$ mm from the point of view of the indeterminacy of n_e , assuming that the real embedding depth is $h = 0.5 \pm 0.07$ mm.

The range of values used for ν was obtained from gas-dynamic calculations for a specific series of experiments used to select the line parameters. For other collision frequencies, the line parameters (h, S, ω) can be selected by calculation and experiment to give the best possible accuracy. It is important to note that according to these experiments, the signal was attenuated predominantly by absorption in the plasma. In the calculations we neglected the mutual influence of the conductors, the radiation losses of the transmission line (because of the nonideal setup), the nonideal drawing of the wires, and the fact that the condition of infinite insulator thickness is only approximately satisfied. This is why the electron density determined by the practical microwave method is lower than the calculated value (for $h = 0.57$ mm this density is 3 times lower, and for $h = 0.5$ mm it is 2.7 times lower than the calculated value for our apparatus). However, comparative experiments indicate that the weak dependence of the measured electron density on the collision frequency and the accuracy of this method of determining the density have been confirmed experimentally. The density, which can be measured by the microwave method

(in a specific practical implementation), is determined by electromagnetic calibration for the same mixture parameters and an attenuation level of 0.6–0.9. Then the constraint imposed in the calculations, limiting the attenuation to 0.6 (neglecting additional losses not taken into account in the calculations) is satisfied even more strictly. Although the calculations mainly serve as a qualitative validation of the method, they can be used to make a fairly accurate choice of line parameters under the required conditions. The high accuracy of the method should be noted. For instance, when calibrated electromagnetically, the spread in the determination of the density by the microwave method was less than 20% at a signal level of 0.6–0.9 when the parameters and the percent composition of the mixtures varied appreciably, and the intrinsic accuracy of the microwave method was as high as 4%.

To sum up, the electromagnetic method can be used to set the required line parameters and to calibrate the apparatus

by an electromagnetic method in a channel of simple cross section where the test method is to be used. Then, the electron density (in the absence of an external magnetic field) can be measured in this channel or in channels of more complex profile.

The authors would like to thank G. K. Tumakaev for useful consultations and R. V. Vasil'eva for discussions of the results.

¹D. G. Zavarin, V. V. Rozhdestvenskii, and G. K. Tumakaev, in *Low-Temperature Plasma Diagnostics* [in Russian], Nauka, Moscow (1979).

²R. V. Vasil'eva, A. L. Genkin, V. L. Goryachev *et al.*, *Low-Temperature Rare-Gas Plasma with Nonequilibrium Ionization and MHD Generators* [in Russian], A. I. Ioffe Physicotechnical Institute, Russian Academy of Sciences, St. Petersburg (1991).

³G. A. Grinberg and B. É. Bonshtedt, *Zh. Tekh. Fiz.* **24**, 67 (1954).

⁴Yu. P. Raizer, *Physics of Gas Discharges* [in Russian], Nauka, Moscow (1987).

Translated by R. M. Durham

Local metallic conductivity of thin polyimide films as a result of “soft” electrical breakdown

A. M. El'yashevich, A. N. Ionov, V. M. Tuchkevich, M. É. Borisova, O. V. Galyukov, and S. N. Koïkov

A. F. Ioffe Physicotechnical Institute, Russian Academy of Sciences, St. Petersburg;
St. Petersburg State Technical University

(Submitted March 18, 1997)

Pis'ma Zh. Tekh. Fiz. **23**, 8–12 (July 26, 1997)

The electrical breakdown of a thin polyimide film between metal electrodes has been investigated under conditions of strong confinement of the breakdown current. The result of this “soft” electrical breakdown is a local, highly conducting channel in the insulating film implanted in the polymer and consisting of a compound of carbon and metal from the electrodes.

It is shown that the polymer channel is converted to the superconducting state by the superconducting properties of the metal from the electrodes. © 1997 American Institute of Physics. [S1063-7850(97)01807-7]

It was established in Refs. 1 and 2 that a conducting channel, whose conductivity is maintained down to low (helium) temperatures, may be formed in a polyimide film placed between metal electrodes at a pressure of several kilograms per square centimeter and an applied voltage of ≈ 1 kV. A reversible switching effect (“sensor effect”) from the conducting to the nonconducting state and back is observed as the pressure is decreased and increased again (the resistance of the channel depends on the pressure applied to the film). This conductivity is caused by the penetration of electrode metal into the polymer. Here, we propose to determine the nature of this conducting channel.

For this study we used polyimide film, $12 \mu\text{m}$ thick, made by Dupont. It was first confirmed that the action of pressure on the polymer film does not produce a sensor effect in the absence of an applied electric voltage. After a conducting channel had formed in these films, they could be removed from the electrodes and placed between electrodes made of a different metal.

The conditions for the formation of a conducting channel

in the film were selected so that at the instant of electrical breakdown, a current no greater than a few microamperes could flow through the sample. We call these conditions “soft breakdown” conditions. In our experiments, the minimum absolute value of the current at which breakdown occurred was $0.1 \mu\text{A}$.

When all the films with a conducting channel were examined under a microscope at magnifications between 96 and 400, they exhibited a breakdown track in the form of a single circular hole whose diameter (between 3 and $30 \mu\text{m}$) depended on the breakdown current. On both sides of the film around the perimeter of the hole we observed a ring $1\text{--}2 \mu\text{m}$ thick with a characteristic metallic luster, which in principle could be caused by graphite-like structures formed during the soft breakdown.

Films in which conducting channels were produced by soft breakdown between pairs of Nb, Re, graphite, and Ge electrodes were placed between Nb electrodes. When an external pressure of the same order of magnitude as that used for soft breakdown was applied to the electrodes, conduction

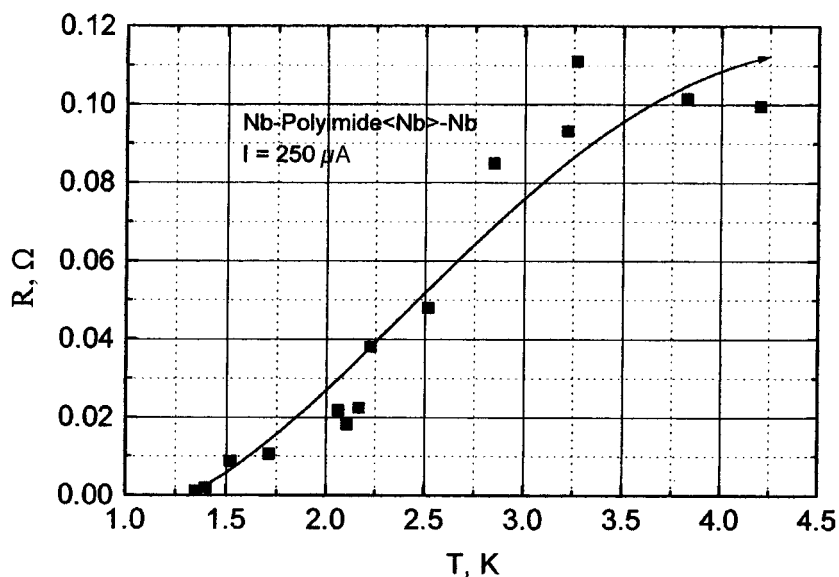


FIG. 1. Resistance versus temperature for the conducting channel in a polymer formed between two niobium electrodes.

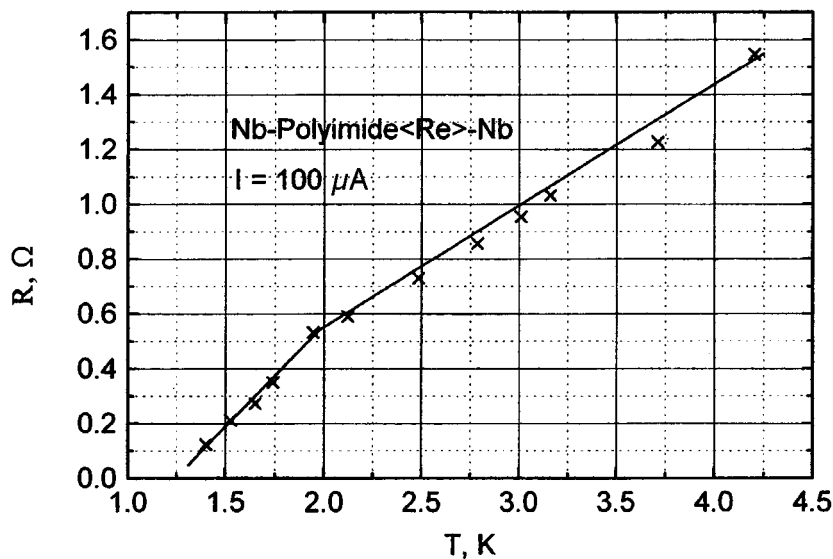


FIG. 2. Resistance versus temperature for the conducting channel in a polymer formed between two rhenium electrodes.

occurred. The onset of conduction was identified by the disappearance of the noise signal at the input to a digital voltmeter with a high input resistance, connected to the Nb-polymer(Me)-Nb structure. The structure was then placed in a helium cryostat where the temperature dependence of the conductivity was investigated in the range 1.4–4.2 K. Niobium was chosen because in this temperature range the electrodes made no contribution to the total conductivity, since the superconducting transition temperature for Nb is $T_c = 9.3$ K.

First, in order to determine whether metallic dendrites penetrating into the polymer are responsible for the conductivity of the channel, we performed soft breakdown on a polymer film between Ge electrodes doped with As, at a dopant concentration $n = 6 \times 10^{16} \text{ cm}^{-3} < n_c$, where $n_c = 3.5 \times 10^{17} \text{ cm}^{-3}$ is the critical dopant (As) concentration for a transition to the metallic state. When studying the conductivity of the Nb-polymer(Ge)-Nb structure at helium temperatures, we observed that the resistance did not increase exponentially with temperature, as would be expected for Ge dendrites with this dopant concentration, but that the channel resistance was almost independent of temperature. This indicated that the conductivity of the conducting channel was metallic. The same pattern was observed in Nb-polymer(graphite)-Nb structures. These experiments indicate that in soft breakdown the conducting channel is formed by graphitization.

A completely different picture was observed when soft breakdown was achieved in a film placed between electrodes made of Nb, which is a superconductor at low-temperatures. In this case, as can be seen from Fig. 1, the resistance of the Nb-polymer(Nb)-Nb structure falls sharply at $T < 3.5$ K,

and at $T_c = 1.4$ K the resistance of the channel is essentially zero. The observed superconducting transition temperature is much lower than the usual value of T_c for bulk Nb. This behavior suggests that the structure of the conducting channel cannot be reduced to a simple metal lining of the aperture walls or a metallic dendrite, but is more complex. We postulate that when a film located between metal electrodes undergoes soft breakdown, a layer of a compound of carbon and a superconducting metal is formed on the inner wall of the hole, and this is responsible for the superconducting transition with decreasing temperature. It is known that compounds of carbon with superconducting metals possess superconducting properties but T_c may be lower than that for a pure superconductor.³

An investigation of an Nb-polymer(Re)-Nb structure also revealed that at $T < 1.9$ K the resistance falls sharply with temperature (Fig. 2), corresponding to the transition of Re to the superconducting state ($T_c = 1.7$ K). These experiments support the conclusion that the electrode metal has a substantial influence on the conductivity of the channel formed as a result of soft breakdown.

The authors would like to thank Professor V. S. Zakrevskiĭ for discussions.

This work was supported by the Russian Fund for Fundamental Research, Grant N96-03-33730.

¹A. M. El'yashevich, A. N. Ionov, M. M. Rivkin, and V. M. Tuchkevich, *Fiz. Tverd. Tela* (St. Petersburg) **34**, 3457 (1992) [*Sov. Phys. Solid State* **34**, 1850 (1992)].

²A. M. El'yashevich *et al.*, *Vysokomol. Soedin.* **35**, 50 (1993).

³*Superconducting Compounds of Transition Metals* [in Russian] (Nauka, Moscow, 1976).

Translated by R. M. Durham

Thermal and isothermal slip in a new Liu model transport equation

A. V. Latyshev and A. A. Yushkanov

Moscow Pedagogical University

(Submitted January 22, 1997)

Pis'ma Zh. Tekh. Fiz. **23**, 13–16 (July 26, 1997)

The aim of this study was to investigate the suitability of the Liu model to solve boundary-value problems in kinetic theory. The problem of isothermal and thermal slip, which is of independent interest, is solved. A constraint on the determining parameter of the model is obtained. © 1997 American Institute of Physics. [S1063-7850(97)01907-1]

The collision integral proposed in Ref. 1 was developed and applied in Refs. 2–4 because of the various advantages inherent in this approach, including its relative simplicity combined with the possibility of accurately describing important gas parameters, such as the Prandtl number. In Refs. 2–4 the collision integral was only used to analyze volume problems. However, a serious assessment of this integral cannot be obtained without analyzing the possibility of using it to describe boundary-value problems. Our aim is to use the collision integral from Ref. 1 to analyze problems of thermal and isothermal slip, and also to identify constraints on the parameter of the model.

Linearizing the Boltzmann equation with the collision integral from Ref. 1, we obtain

$$\begin{aligned} \frac{\partial f}{\partial t} + \mathbf{v} \cdot \nabla f = -\zeta(f - f^{(0)}) + 2\beta A f^{(0)} \left(v_i v_j - \frac{1}{3} v^2 \delta_{ij} \right) \nabla_j u_i \\ + B f^{(0)} \left(\beta v^2 - \frac{5}{2} \right) \nabla_i \nabla_j \ln T, \quad \beta = m/2kT. \end{aligned} \quad (1)$$

Here f is the distribution function, \mathbf{v} is the molecular velocity, m is the molecular mass, k is the Boltzmann constant, T is the local gas temperature, \mathbf{u} is the local mass velocity of the gas, ζ has the meaning of the collision integral, $f^{(0)}$ is the local equilibrium Maxwell distribution,

$$f^{(0)} = n(\beta/\pi)^{3/2} \exp(-\beta V^2), \quad \mathbf{V} = \mathbf{v} - \mathbf{u},$$

and n is the local molecular concentration. The coefficients A and B are related to the coefficient of viscosity η_0 and the thermal conductivity λ_0 :

$$A = 1 - \xi \eta_0 / nkT, \quad B = 1 - 2\xi \lambda_0 m / 5nk^2T.$$

The model parameters may be selected to obtain an accurate value of the Prandtl number and also so that the Burnett coefficients either for the heat flux or for the pressure tensor agree with the appropriate values obtained from the complete Boltzmann equation. It was shown in Refs. 1 and 2 that this model satisfies the conservation laws and the H -theorem, and in Ref. 4 it was used in nonlinear problems.

Let us assume that a gas fills the half-space $x > 0$ and that the x axis is directed inside the gas perpendicular to the surface. We assume that the gas has a temperature gradient parallel to the surface and a tangential velocity gradient perpendicular to the surface, and that both gradients are small. We shall assume that the directions of the gas velocity and

the temperature gradient coincide with the z axis. Linearizing the problem, we write $f = f_0(1 + \varphi_0 + \varphi)$, where φ_0 is the Chapman distribution function,

$$\varphi = 2c_y \left[u_{sl} + 2Kx - (1-A)Kc_x + \frac{3}{4}(1-A)L \left(\frac{5}{2} - c^2 \right) \right],$$

f_0 is the Maxwell distribution function, φ is an unknown function, u_{sl} is an unknown slip velocity, $K = (\partial u_y^* / \partial x)_{x=\infty}$, and $L = (\partial \ln T / \partial y)_{x=\infty}$. For the function φ we cast Eq. (1) in the dimensionless form

$$c_x \frac{\partial \varphi}{\partial x'} + \varphi = 2c_y u_y^* + 2A c_x c_y \frac{\partial u_y^*}{\partial x'}.$$

Here $\mathbf{c} = \beta_0 \mathbf{v}$, $\mathbf{u}^* = \beta_0 \mathbf{u}$, $x' = \beta_0 \xi x$, $\beta_0 = \sqrt{m/2kT_0}$, $0 \leq A \leq \frac{1}{3}$, A is a numerical parameter, and x' again denotes x .

For $x \rightarrow +\infty$ the function $\varphi + \varphi_0$ should yield the Chapman function, i.e., $\varphi(+\infty, \mathbf{c}) = 0$. We shall assume that the scattering of molecules at the surface is purely diffuse, i.e., $\varphi(0, \mathbf{c}) = -\varphi_0(0, \mathbf{c})$, $c_x > 0$. We express the function φ in the form

$$\varphi = c_y [\psi(x, \mu) + (c_y^2 + c_z^2 - 2)g(x, \mu)], \quad \mu = c_x.$$

We then obtain

$$\begin{aligned} \mu \frac{\partial}{\partial x} \psi(x, \mu) + \psi(x, \mu) = \frac{1}{\sqrt{\pi}} \int_{-\infty}^{\infty} e^{-\mu'^2} \left(1 + A \mu \frac{\partial}{\partial x} \right) \\ \times \psi(x, \mu') d\mu', \end{aligned} \quad (2)$$

with the boundary conditions

$$\begin{aligned} \psi(0, \mu) = -2 \left[u_{sl} - (1-A)K\mu - \frac{3}{4}(1-A)L \left(\mu^2 - \frac{1}{2} \right) \right], \\ \mu > 0, \end{aligned} \quad (3)$$

$$\psi(\infty, \mu) = 0, \quad \mu < 0. \quad (4)$$

Using generalized functions and boundary-value problems of analytic functions, it can be shown that the problem (2)–(4) has a single solution

$$\begin{aligned} \psi(x, \mu) = \frac{1}{\sqrt{\pi}} \int_0^{\infty} e^{-x/\eta} \frac{\eta - A\mu}{\eta - \mu} a(\eta) d\eta \\ + (1-A)e^{\mu^2 - x/\mu} \lambda(\mu) a(\mu) \chi_+(\mu). \end{aligned}$$

Here

$$\lambda(z) = 1 + z \frac{1}{\sqrt{\pi}} \int_{-\infty}^{\infty} e^{-\tau^2} \frac{d\tau}{\tau - z}$$

is the Cercignani dispersion function, $\chi_+(\mu) = 1$ if $\mu > 0$; $\chi_+(\mu) = 0$ if $\mu < 0$,

$$a(\mu) = -\frac{c_0 + c_1\mu}{2\pi i\mu} \left(\frac{1}{X^+(\mu)} - \frac{1}{X^-(\mu)} \right),$$

where $c_0 = 2K + \frac{3}{2}LX_2$ and $c_1 = \frac{3}{2}L$. The function $X(z)$ satisfies the Riemann boundary-value problem $X^+(\mu)/X^-(\mu) = \lambda^+(\mu)/\lambda^-(\mu)$, $0 < \mu < \infty$, for which $X(z) = \sum_{n=0}^{\infty} X_n z^{-n}$, where

$$X_n = -\frac{2}{\sqrt{\pi}} \int_0^{\infty} \frac{e^{-\tau^2} \tau^n d\tau}{X(-\tau)}, \quad n = 1, 2, \dots;$$

$$X(z) = \frac{1}{z} \exp \left[\frac{1}{\pi} \int_0^{\infty} \frac{\arg \lambda^+(\tau) - \pi}{\tau - z} d\tau \right].$$

The required slip velocity is obtained by constructing the distribution function using methods of contour integration

$$u_{sl} = C_m lK + K_T \nu L,$$

where C_m and K_T are the coefficients of isothermal and thermal slip, respectively, given by

$$C_m = \frac{2}{\sqrt{\pi}} \frac{X_2 - A/\sqrt{2}}{1 - A}, \quad K_T = \frac{3}{2} \left[\frac{X_3}{1 - A} - \frac{A}{1 - A} \frac{X_2}{2\sqrt{2}} \right]. \quad (5)$$

It can be seen from the equalities (5) that for $A \rightarrow 0$, these expressions yield the corresponding formulas for the Bhatnagar, Gross, and Krook (BGK) model obtained by Cercignani⁵ and Loyalka.⁶ A comparison between the results obtained using the formulas (5) and the numerous results from Ref. 7 obtained using the complete Boltzmann equation and its models, reveals that the range of values of the parameter A proposed in Ref. 1 ($0 \leq A \leq \frac{1}{3}$) is too high. The coefficients C_m and K_T are fairly sensitive to the value of A . Reasonable agreement between the results obtained for the complete Boltzmann equation for molecules — hard spheres — and the results obtained using the model of Ref. 1 can be achieved for $0 \leq A \leq \frac{1}{5}$. Thus, an analysis of the solution of boundary-value problems can reveal significant constraints on the determining parameter of the model of Ref. 1

To conclude, the proposed model can be used⁸ to describe the behavior of a dense gas near a surface.

¹G. Liu, Phys. Fluids A **2**, 277 (1990).

²V. Garzó, Phys. Fluids A **3**, 1980 (1991).

³V. Garzó, Molec. Phys. **78**, 1129 (1993).

⁴V. Garzó and M. López de Haro, Phys. Fluids **6**, 3787 (1994).

⁵C. Cercignani, *Mathematical Methods in the Kinetic Theory of Gases* [Russ. transl., Mir, Moscow, 1973].

⁶S. K. Loyalka, Physica A **163**, 813 (1990).

⁷T. Ohwada, Y. Sone, and K. Aoki, Phys. Fluids A **1**, 1588 (1989).

⁸A. V. Latyshev and A. A. Yushkanov, Poverkhnost' No. 6, 45 (1994).

Translated by R. M. Durham

Integrated ionizing-radiation detector utilizing a cadmium sulfide-cadmium telluride heterojunction

V. P. Makhniĭ and Ya. N. Barasyuk

Yu. Fed'kovich State University, Chernovtsy

(Submitted August 5, 1996; resubmitted February 20, 1997)

Pis'ma Zh. Tekh. Fiz. **23**, 17–20 (July 26, 1997)

A description is given of an x-ray detector in which the scintillator and the photodiode are integrated in the structure of the heterojunction. Characteristics of the conversion of radiation into a current signal are given for a dose rate of 1 R/h. It is shown that besides the convenience of the monolithic design, a biased integrated detector has a substantially higher sensitivity compared with detectors now being used. © 1997 American Institute of Physics. [S1063-7850(97)02007-7]

Scintillator-photodiode systems may have many applications in the recording of ionizing radiation having powers up to 10^6 Gy in the energy range 0.01–20 MeV (Ref. 1). Various types of commercial Si photodiodes are usually used as the photodetector. The scintillator material should have a high energy yield and fast response time, it should be highly transparent to radioluminescent radiation, and it should be resistant to moisture, temperature, radiation, and so forth. These requirements are satisfied to some extent by CdS and ZnSe crystals doped with isovalent Te (Ref. 2). In addition, the combination of scintillation and semiconducting properties allow the photodetector to be fabricated directly on the surface of the scintillator crystal. The dose sensitivity achieved so far for $p\text{CdTe}-n\text{CdS}\langle\text{Te}\rangle$ and $p\text{ZnTe}-n\text{ZnSe}\langle\text{Te}\rangle$ integrated detectors is around 10^{-7} A·cm $^{-2}$ ·R $^{-1}$ h (Refs. 3 and 4). Further improvement involves improving the parameters of the individual elements and of the system as a whole, particularly the light collection efficiency. Here we consider one possible method of solving this problem — by enhancing the sensitivity of the photodetector in an integrated $p\text{CdTe}-n\text{CdS}\langle\text{Te}\rangle$ detector.

Scintillation crystals of CdS were obtained from a melt under inert-gas pressure and were doped with up to 0.1 mol.% Te during the growth process. At room temperature these crystals exhibit *n*-type conductivity (~ 1 S/cm) and efficient (15–20%) red photoluminescence and radioluminescence N_λ with a peak at 0.73 μm , as shown in Fig. 1. Also shown is the spectrum of the photosensitivity S_λ of a heterojunction fabricated on a CdS $\langle\text{Te}\rangle$ base substrate by solid-phase substitution reactions.⁵ The coefficient of utilization of the radiation given by $K_u = \int_0^\infty N_\lambda \cdot S_\lambda \cdot d_\lambda / \int_0^\infty N_\lambda \cdot d_\lambda$, is around 0.4 for this integrated detector, which is slightly lower than that for a combined CdS $\langle\text{Te}\rangle$ -Si photodiode [$K_u \approx 0.55$ (Ref. 1)]. In addition, the light collection efficiency for the integrated detector should be superior to that for the combined detector, for several reasons. First, the refractive index of CdTe ($n \approx 2.75$) is higher than that of CdS ($n \approx 2.5$), which eliminates total internal reflection at the heterojunction interface. Second, the variable-gap CdS $_x$ Te $_{1-x}$ provides reliable optical contact without using special antireflection coatings and complex methods of depositing these in a combined detector. These factors lead to an increase in the fraction of the radioluminescent radiation

incident on the photodiode in this integrated detector.

Scintillation was excited using an x-ray tube with a Cu anode at a supply voltage of 40 kV. The integrated detector under study and a standard combined detector were positioned at a distance for which the x-ray dose rate was 1 R/h. Under these conditions, the photocurrent density I_p of the combined detector at zero bias was around 10^{-7} A/cm 2 , as shown in Fig. 2. Note that this value is close to the dark current density I_d of the FD-228 photodiodes used in this device. These values of I_p and I_d are maintained up to reverse voltages $V \approx 10$ V. A further increase in V leads to an abrupt rise in I_d with an almost unchanged useful output signal.

The curve $I_p(V)$ for the heterojunction detector differs substantially from that for the standard detector, as can be seen from Fig. 2. While the absolute value of the photocurrent of the integrated detector is the same as that of the combined detector at zero bias, it is almost two orders of magnitude higher at $V \geq 50$ V. Investigations⁵ have shown that the heterojunction is a *p-i-n* structure, with the thickness d of the *i*-region around 50 μm . The photocurrent of this diode begins to saturate in fields $E_{cr} \approx V/d = 50 / (5 \times 10^{-5}) = 10^6$ V/m. This is close to the critical electric field for which the electron drift velocity in CdTe saturates.⁶ However, the saturation of I_p for $V > 50$ V implies that the maximum collection coefficient is achieved for the light-generated carriers. An estimate of the photocarrier transit time in the *i*-region for the heterojunction parameters specified above gives about 10^{-10} s. Note also that the specific

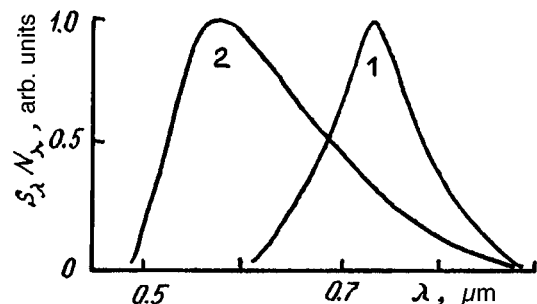


FIG. 1. Radioluminescence spectrum of CdS $\langle\text{Te}\rangle$ crystal (1) and photosensitivity spectrum of $p\text{CdTe}-n\text{CdS}\langle\text{Te}\rangle$ heterojunction (2) at 300 K.

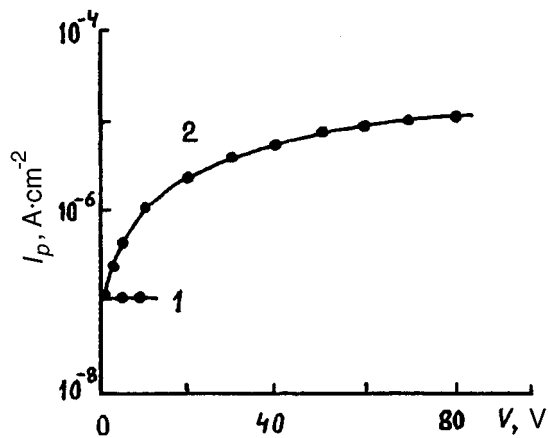


FIG. 2. Output signal I_p versus reverse voltage on photodiode for combined (1) and integrated (2) detectors irradiated by x-rays at a dose rate of 1 R/h. The dimensions of the scintillator are $5 \times 5 \times 5$ mm and the area of the photodiodes is 25 mm^2 .

capacitance of these heterostructures is around 200 pF/cm^2 as compared with 700 pF/cm^2 for the FD-288 photodiode. In addition, the dark current of the heterojunction is more than an order of magnitude lower than I_d for a Si diode, and is also lower than the useful signal of the integrated detector for these measurement conditions over the entire range of volt-

ages studied. These factors combined with the advantages of the monolithic design make it possible to operate these detectors at zero bias, where the dose sensitivities of the integrated and combined detectors are comparable, $10^{-7} \text{ A} \cdot \text{cm}^{-2} \cdot \text{R}^{-1} \text{ h}$. This sensitivity may be enhanced by two orders of magnitude by connecting the heterojunction as a photodiode at $V \geq 50 \text{ V}$ (Fig. 2).

To sum up, these results have convincingly demonstrated that it is promising to use a $p\text{CdTe}-n\text{CdS}\langle\text{Te}\rangle$ heterojunction as a highly efficient ionizing-radiation detector.

The authors would like to thank V. D. Ryzhikov for kindly supplying the $\text{CdS}\langle\text{Te}\rangle$ crystals.

¹ V. D. Ryzhikov, P. E. Stadnik, and Yu. A. Yakovlev, *Prib. Tekh. Éksp.* No. 5, 6 (1989).

² V. D. Ryzhikov, *Scintillation Crystals of II-VI Semiconductor Compounds: Preparation, Properties, and Application* [in Russian] (NIITEKhIM, Moscow, 1989).

³ V. D. Ryzhikov, O. P. Verbitskiĭ, E. M. Selegenev, and V. I. Silin, USSR Patent No. 1436794, publ. 05.05.1986.

⁴ O. P. Verbitskiĭ, L. A. Kosyachenko, V. P. Makhniĭ, and V. D. Ryzhikov, *Pis'ma Zh. Tekh. Fiz.* **14**, 702 (1988) [*Sov. Tech. Phys. Lett.* **14**, 311 (1988)].

⁵ V. E. Baranyuk, Ya. M. Barasyuk, and V. P. Makhniĭ, *Ukr. Fiz. Zh.* **41**, 450 (1996).

⁶ C. Canali, M. Martini, G. Ottaviani, and K. Zanio, *Phys. Lett. A* **33**, 241 (1970).

Translated by R. M. Durham

Modification of the Kirchhoff scalar diffraction integral

Sh. D. Kakichashvili and B. N. Kilosanidze

Institute of Cybernetics, Georgia Academy of Sciences, Tbilisi, Georgia
(Submitted May 15, 1996; resubmitted March 18, 1997)
Pis'ma Zh. Tekh. Fiz. **23**, 21–24 (July 26, 1997)

An analysis is made of a modification of the Kirchhoff scalar diffraction integral, in which the secondary waves are summed not only over the incoming wave front but also in a certain volume along its path. An example of a freely propagating, unbounded plane wave is used to show that this approach eliminates the disparity between the description using the accurate form of the Kirchhoff diffraction integral compared with the *a priori* description of this wave. © 1997 American Institute of Physics. [S1063-7850(97)02107-1]

The Kirchhoff diffraction integral is widely used in many theoretical and practical applications in optics, quasi-optics, and radiophysics.^{1–3} A polarization modification of the Kirchhoff integral has been analyzed, most systematically by Kottler.⁴ A similar form was obtained in Ref. 5 and applied to various problems in holography.^{6,7} The disagreement between the Kirchhoff theory and the experimental results shows up particularly clearly for large diffraction angles and in problems involving the description of the polarization of diffracted fields. Even for a freely propagating unbounded wave, the Kirchhoff diffraction integral describes this wave adequately only in the approximation of large observation distances. However, when its accurate form is used, such adequacy of description is unattainable. This circumstance clearly indicates that there are fundamental restrictions on the validity of Green's theorem in this case.⁸

This state of affairs was responsible for the appearance of the so-called geometric diffraction theory proposed by Keller,⁹ in which a set of computational algorithms is defined for various typical classes of diffracting objects. However, the physically based generality of the analysis is somewhat lost in this approach.

In this paper the Kirchhoff scalar diffraction integral is modified to apply to arbitrary observation distances. We use an extended concept of the Huygens–Fresnel principle, where the secondary waves are summed not only over the incoming wave front, but also in a certain volume along its path. It seems to us that the disagreement between the description obtained for an unbounded wave using the accurate form of the Kirchhoff diffraction integral compared with the *a priori* description of this wave may be eliminated by using this extended concept of the Huygens–Fresnel principle.

We write the Kirchhoff scalar diffraction integral in the well-known complex form:¹

$$\hat{E}(x, y, z, t) = \frac{1}{4\pi} \int_{x_0} \int_{y_0} \left(\hat{E}_0 \frac{\partial \hat{G}}{\partial n} - \frac{\partial \hat{E}_0}{\partial n} \hat{G} \right) dx_0 dy_0, \quad (1)$$

where $\hat{E}(x, y, z, t)$ is the field at the observation point, $\hat{E}_0(x_0, y_0, z_0, t)$ is the field directly beyond the diffracting object, $\hat{G} = \exp i\kappa R/R$ is the Green's function for free space, $\kappa = 2\pi/\lambda$ is the wave number, $R = \sqrt{(x-x_0)^2 + (y-y_0)^2 + (z-z_0)^2}$ is the distance between the observation point and a point on the surface of the object,

x_0, y_0, z_0 are the coordinates of the point on the object, x, y, z are the coordinates of the observation point, and n is the normal to the surface of integration. Integration is performed over the two-dimensional region (X_0, Y_0) occupied by the object.

In the proposed modification we express the integral (1) in the form:

$$\hat{E}(x, y, z, t) = \frac{1}{4\pi} \int_{x_0} \int_{y_0} \int_{z_0} \left(\hat{E}_0 \frac{\partial \hat{G}}{\partial n} - \frac{\partial \hat{E}_0}{\partial n} \hat{G} \right) dx_0 dy_0 dz_0. \quad (2)$$

Here integration is performed over the object occupying the three-dimensional region (X_0, Y_0, Z_0) .

To illustrate the validity of this generalization, we consider the field of an unbounded plane wave propagating freely along the z axis. In this case, Eq. (2) has the form:

$$\begin{aligned} \hat{E}(x, y, z, t) = & \frac{i\kappa}{4\pi} \exp i\omega t \int_{x_0} \int_{y_0} \int_{z_0} E_0 \exp -i\kappa z_0 \\ & \times \left[\frac{z-z_0}{R} \left(1 + \frac{1}{i\kappa R} \right) + 1 \right] \\ & \times \frac{\exp -i\kappa R}{R} dx_0 dy_0 dz_0, \end{aligned} \quad (2')$$

where $\hat{E}_0 = E_0 \exp i(\omega t - \kappa z_0)$.

We first calculate the double integral over (X_0, Y_0) in Eq. (2') using the asymptotic approximation. For this solution we use the steady-state phase method where the points $x_0 = x$ and $y_0 = y$ are taken as the critical points.¹ As a result, we have:

$$\begin{aligned} \hat{E}(x, y, z, t) = & E_0 \exp i(\omega t - \kappa z) \int_{z'_0}^{z'_0 + \hat{d}} \\ & \times \left[1 + \frac{1}{2i\kappa(z-z_0)} \right] dz_0, \end{aligned} \quad (3)$$

where the limits of integration are $z'_0 \leq z_0 \leq z'_0 + \hat{d}$, and $\hat{d} = d' - id''$ is complex.

Integrating Eq. (3) over the region Z_0 gives:

$$\hat{E}(x, y, z, t) = \left\{ \hat{d} - \frac{1}{2i\kappa} [\ln(z - z'_0 - \hat{d}) - \ln(z - z'_0)] \right\} \times E_0 \exp i(\omega t - \kappa z). \quad (4)$$

An adequate description of a freely propagating, unbounded plane wave clearly requires that the corresponding coefficient in Eq. (4) should be equated to unity

$$\hat{d} - \frac{1}{2i\kappa} [\ln(z - z'_0 - \hat{d}) - \ln(z - z'_0)] = 1. \quad (5)$$

This condition yields a system of equations to determine the real and imaginary parts of \hat{d} :

$$\begin{aligned} d' + (z - z'_0) \cos 2\kappa(1 - d') \exp 2\kappa d'' - (z - z'_0) &= 0, \\ d'' + (z - z'_0) \sin 2\kappa(1 - d') \exp 2\kappa d'' &= 0. \end{aligned} \quad (6)$$

Having solved Eqs. (6), the solution for \hat{d} clearly exhibits its periodicity, which may be simply associated with the Fresnel zones, not those located at the wavefront but rather those positioned along the path.

The values of d' and d'' were obtained from the matching between the unbounded plane wave and its *a priori* description. We believe that this approach may be applied to the case of an arbitrary diffracting object. Then d' plays the role of the length of the diffracting object along the z axis and d'' is an auxiliary quantity. In this way, the expression (2) is completely determined.

For a diffracting object with specific characteristics of thickness, absorption, and so forth, this approach may be

extended to the case of a complex wave number $\hat{\kappa}$, which is known to correspond to the most general form of the solution of the Helmholtz wave equation. Then, the diffraction problem necessarily involves finding the imaginary parts of \hat{d} and $\hat{\kappa}$ from a condition similar to (5) for matching of the solution obtained using Eq. (2) with the *a priori* description of this wave, and this we propose to do subsequently.

The authors would like to thank Z. N. Talakvadze and M. M. Khazaradze for supporting this work.

The investigation described in this publication was made possible by Grant No. LC3000 from the International Science Foundation.

¹M. Born and E. Wolf, *Principles of Optics*, 4th ed. (Pergamon Press, Oxford, 1969) [Russ. transl., Nauka, Moscow, 1970].

²A. Sommerfeld, *Optics*, transl. from the German (Academic Press, New York, 1954) [Russ. transl., IL, Moscow, 1953].

³F. A. Korolev, *Theoretical Optics* [in Russian] (Vysshaya Shkola, Moscow, 1966).

⁴F. Kottler, *Electromagnetic Theory*, in *Progress in Optics*, Vol. VI (North-Holland, Amsterdam, 1967), pp. 333–377.

⁵Sh. D. Kakichashvili, *Polarization Holography* [in Russian] (Nauka, Leningrad, 1989).

⁶D. Gabor, *Nature* (London), **161**, 777 (1948).

⁷Yu. N. Denisyuk, *Dokl. Akad. Nauk SSSR* **162**, 1275 (1962).

⁸H. Poincaré, *Acta. Math.* **16**, 297 (1892).

⁹V. A. Borovikov and B. E. Kinber, *Geometric Theory of Diffraction* [in Russian] (Svyaz', Moscow, 1978).

Translated by R. M. Durham

Plasticity of diamond at room temperature and determination of its hardness using an atomic force microscope with an ultrahard C₆₀ fullerite tip

V. D. Blank, M. Yu. Popov, N. A. L'vova, K. V. Gogolinskiĭ, and V. N. Reshetov

“Superhard Materials” Scientific and Technical Center, State Committee for Science and Technology;
Institute of Spectroscopy, Russian Academy of Sciences;
“NTE” Scientific-Industrial Organization, Zelenograd
(Submitted February 20, 1997)
Pis'ma Zh. Tekh. Fiz. **23**, 25–29 (July 26, 1997)

A method has been developed to measure the hardness of superhard materials with an atomic force microscope. By using an indenter made of ultrahard fullerite C₆₀, of hardness superior to that of diamond, plastic deformation of diamond is achieved at room temperature without any crack formation and its hardness is measured. © 1997 American Institute of Physics. [S1063-7850(97)02207-6]

Measurements of the hardness of superhard materials, particularly diamond, are of major practical interest. However, it is difficult to make such measurements on diamond at room temperature for various reasons. The main reason is its low plasticity¹ which leads to the depression being damaged during indentation. Also, when the hardness of the sample and the indenter are equal, the hardness depends strongly on the load and the depression made by the indenter exhibits appreciable elastic recovery.

By using an indenter made of ultrahard fullerite C₆₀ (Ref. 2), of hardness superior to that of diamond, and using a new method of measuring the hardness, we succeeded in achieving plastic deformation of diamond at room temperature without any crack formation and we accurately measured its hardness.

The hardness was investigated by a sclerometric method (by scratching with a constant load applied to the indenter). The results obtained by the indentation and sclerometric methods are equivalent,³ although in the latter case the plastic component of the total deformation is greater than that for indentation. The hardness H is given by

$$H = kP/b^2, \quad (1)$$

where k is the shape factor of the indenter, P is the load on the indenter, and b is the scratch width.

Since it is difficult to fabricate an indenter of given shape from a material harder than diamond, we developed a new method which allowed the shape of the indenter to be eliminated from the many parameters determining the hardness.

In this new technique, the load on the indenter is selected so that the scratch width remains constant in all the measurements with this indenter. Then, the hardness H_x of the sample in accordance with formula (1) is given by

$$H_x = H_s(P_x/P_s), \quad (2)$$

where P_x and P_s are the loads on the indenter used to scratch the sample and a standard of known hardness H_s . The mechanical properties of the standard should preferably be similar to those of the material. We used sapphire as the standard.

The samples were scratched (using a “forward edge” scheme) and the shape and size of the scratch were recorded

using a NanoScan measuring system based on the principles of an atomic force microscope and developed by “NTE” (Zelenograd).⁴ The scratching time was 2 s, the scratch width was 0.6 μm, the length was 2.5 μm, and the maximum load on the indenter was 0.1 N. The same probe was used to make a scratch and then scan the surface.

For the experiments we selected tips approximately in the form of trihedral pyramids with an apex angle of around 90 °C.

The proposed method was used to measure the hardness of various hard and superhard materials (quartz, topaz, garnet, sapphire, fianite cubic BN, and natural diamond type IIa) using an ultrahard fullerite C₆₀ tip. The formation of a scratch in these samples was not accompanied by any cracking. The samples were natural and artificial single crystals, prepared for hardness testing in accordance with the recommendations put forward in Ref. 3. As a check, hardness measurements were also made on the same samples (apart from the cubic BN and diamond) by a standard procedure using a PMT-3 hardness gauge with a Vickers pyramid. These measurements revealed good correlation between the results. The following hardness values were obtained for cubic BN and diamond: 60±3 GPa for cubic BN, and 137±6 and 167±5 GPa, respectively, for the (100) and (111) planes of diamond.

In the course of the hardness investigations using formula (2), it was observed that the load P_x could be extrapolated using formula (1), to simplify the measurement procedure, if the scratch width is within 0.5–0.7 μm.

When the hardness of diamond was determined by the proposed technique with a diamond indenter, as compared with the measurements using an ultrahard fullerite indenter, the hardness for the (111) face was found to be 231±6 GPa and the formation of a scratch was accompanied by cracking of the surface, which is typical of diamond.¹

To determine the possibility of plastic deformation at room temperature on a larger scale than in these experiments and to compare the hardness of diamond and ultrahard fullerite C₆₀ series of scratches were made using ultrahard fullerite and carbonado diamond samples. Scratching of the (111) surface of diamond with a diamond sample was accompanied by prolific cracking (Fig. 1), whereas with the

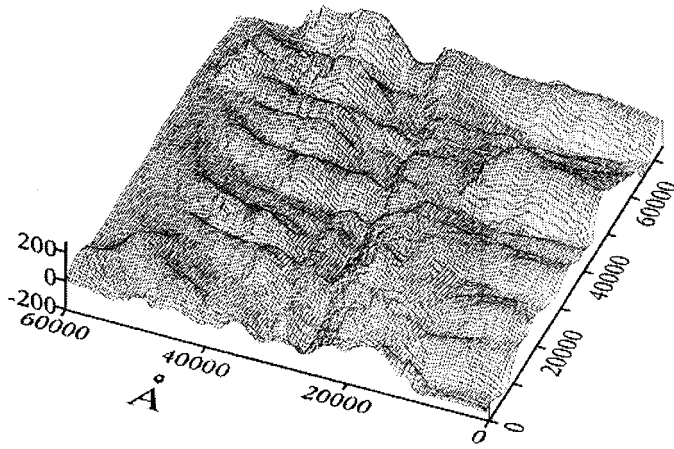


FIG. 1. Scratch created with a diamond on the (111) surface of a diamond sample. Numerous cracks are clearly visible.

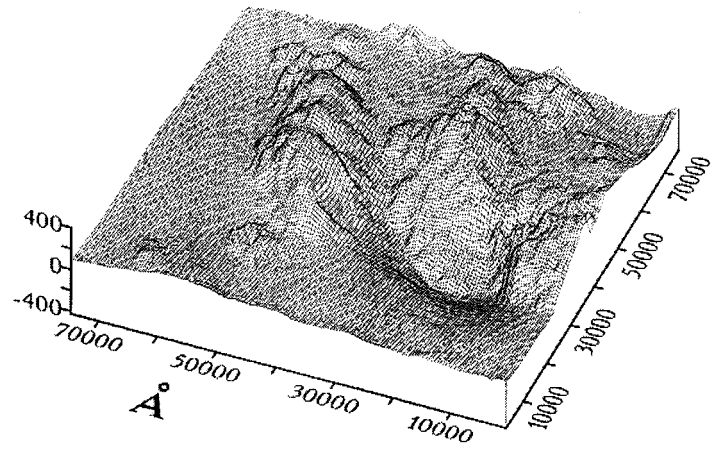


FIG. 2. Plastic deformation of the (111) surface of diamond by an ultrahard fullerite C_{60} sample.

ultrahard fullerite sample, the diamond underwent deformation like a plastic material (Fig. 2). This implies that the hardness of the ultrahard fullerite is sufficient to create the pressure at the point of contact required for plastic flow of the diamond at room temperature, and is superior to the hardness of the diamond.

The hardness obtained for the (100) surface of diamond agrees with the published data.¹ The exaggerated hardness obtained in the experiments with a diamond indenter as compared with an ultrahard fullerite C_{60} indenter (231 and 167 GPa, respectively) may be attributed to inaccuracy in the measurement procedure when the hardness of the sample and the indenter are equal.

In summary, the mechanical properties of a new material — ultrahard fullerite C_{60} — have been studied and it has

been shown that this material may be used to measure the hardness of diamond by a sclerometric technique. The proposed technique was used to measure the hardness of diamond at room temperature and values of 137 ± 6 and 167 ± 5 GPa, respectively, were obtained for the (100) and (111) planes.

¹J. Wilks and E. Wilks, *Properties and Applications of Diamond* (Butterworth, Oxford, 1991).

²V. D. Blank, S. G. Buga, N. R. Serebryanaya *et al.*, *Phys. Lett. A* **205**, 208 (1995).

³V. K. Grigorovich, *Hardness and Microhardness of Metals* [in Russian] (Nauka, Moscow, 1976).

⁴K. V. Gogolinskiĭ *et al.*, *Application of Atomic Force Microscopy to Study Hard Tungsten Carbide Alloys*, Preprint No. 002-96 [in Russian], Moscow Engineering Physics Institute (1996).

Translated by R. M. Durham

Influence of heat treatment conditions on the phase composition and superconducting properties of $\text{Bi}_{1.6}\text{Pb}_{0.4}\text{Sr}_{1.98}\text{K}_{0.02}\text{Ca}_2\text{Cu}_3\text{F}_{0.8}\text{O}_y$ ceramic

N. D. Zhigadlo, V. V. Petrashko, Yu. A. Semenenko, and N. A. Prytkova

Institute of Solid-State and Semiconductor Physics, Belarus Academy of Sciences, Minsk

(Submitted February 25, 1997)

Pis'ma Zh. Tekh. Fiz. **23**, 30–34 (July 26, 1997)

The influence of synthesis temperature and time on the properties and formation of superconducting phases in $\text{Bi}_{1.6}\text{Pb}_{0.4}\text{Sr}_{1.98}\text{K}_{0.02}\text{Ca}_2\text{Cu}_3\text{F}_{0.8}\text{O}_y$ samples has been studied by x-ray phase analysis and by measuring the electrical resistance. It is found that the ratio of the 2223 and 2212 phases formed during synthesis at 845 °C for 240 h remains almost constant in the range 845–855 °C, regardless of the additional synthesis time. Synthesis at higher temperatures leads to breakdown of the 2223 phase and enhances the content of the 2212 phase and impurity phases. The highest values $T_c(R=0)=112.8$ K were obtained for samples synthesized at 845 °C for 240 h. © 1997 American Institute of Physics. [S1063-7850(97)02307-0]

Various authors^{1–6} have reported an appreciable increase in $T_c(R=0)$ and an improvement in other physical properties of (Bi, Pb)–Sr–Ca–Cu–O superconductors when some of the oxygen is replaced with fluorine. However, $T_c(R=0)$ varies widely (between ~81 and ~121 K) for these superconducting materials, depending on the composition, heat treatment regimes, and physicochemical nature of the fluorine-containing reagents. It is therefore important to determine the optimum preparation conditions to obtain (Bi, Pb)–Sr–Ca–Cu–(O, F) superconducting materials with good superconducting parameters.

We prepared superconductors having the nominal composition $\text{Bi}_{1.6}\text{Pb}_{0.4}\text{Sr}_{1.98}\text{K}_{0.02}\text{Ca}_2\text{Cu}_3\text{F}_{0.8}\text{O}_y$ by solid-phase synthesis and studied the influence of temperature and synthesis time on the phase composition and T_c .

Samples having the nominal composition $\text{Bi}_{1.6}\text{Pb}_{0.4}\text{Sr}_{1.98}\text{K}_{0.02}\text{Ca}_2\text{Cu}_3\text{F}_{0.8}\text{O}_y$ were prepared by solid-phase synthesis in air using powders of extra-high-purity Bi and Cu oxides, Ca, Sr, and K carbonates, and PbF_2 . Mixtures of the powders corresponding to the nominal composition were pressed into pellets and calcined at $T=753$ °C for 16 h. These pellets were then ground and re-pressed into discs 12 mm in diameter and about 2 mm thick. The samples were then held at $T=845$ °C for $t=240$ h (a) and underwent additional annealing at $T=845$ °C, $t=120$ h (b) + $T=847$ °C, $t=145$ h (c) + $T=855$ °C, $t=45$ h (d) + $T=870$ °C, $t=6$ h (e) + $T=890$ °C, $t=5$ h (f), with intermediate grinding at all stages. The synthesis and grinding was carried out in air and the samples were cooled to room temperature along with the furnace. The temperature dependences of the electrical resistance $R(T)$ were measured by a standard four-probe dc method. The phase composition of the samples was monitored by x-ray phase analysis using a DRON-4-07 (CuK_α radiation) diffractometer.

Figure 1 shows diffraction patterns of $\text{Bi}_{1.6}\text{Pb}_{0.4}\text{Sr}_{1.98}\text{K}_{0.02}\text{Ca}_2\text{Cu}_3\text{F}_{0.8}\text{O}_y$ ceramic after synthesis at $T=845$ °C for $t=240$ h (a) and the additional annealing in regimes (b)–(f). It can be seen (Fig. 1a) that after synthesis in regime (a), the samples consist of a mixture of two super-

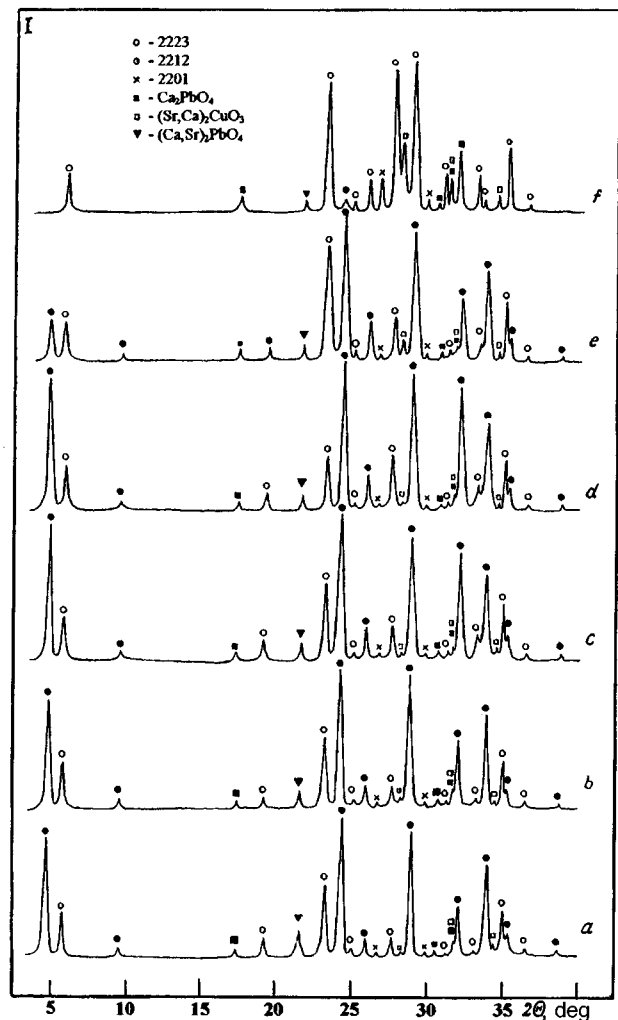


FIG. 1. Diffraction patterns of $\text{Bi}_{1.6}\text{Pb}_{0.4}\text{Sr}_{1.98}\text{K}_{0.02}\text{Ca}_2\text{Cu}_3\text{F}_{0.8}\text{O}_y$ ceramic after synthesis at $T=845$ °C for $t=240$ h (a) and additional annealing at $T=845$ °C, $t=120$ h (b) + $T=847$ °C, $t=145$ h (c) + $T=855$ °C, $t=45$ h (d) + $T=870$ °C, $t=6$ h (e) + $T=890$ °C, $t=5$ h (f).

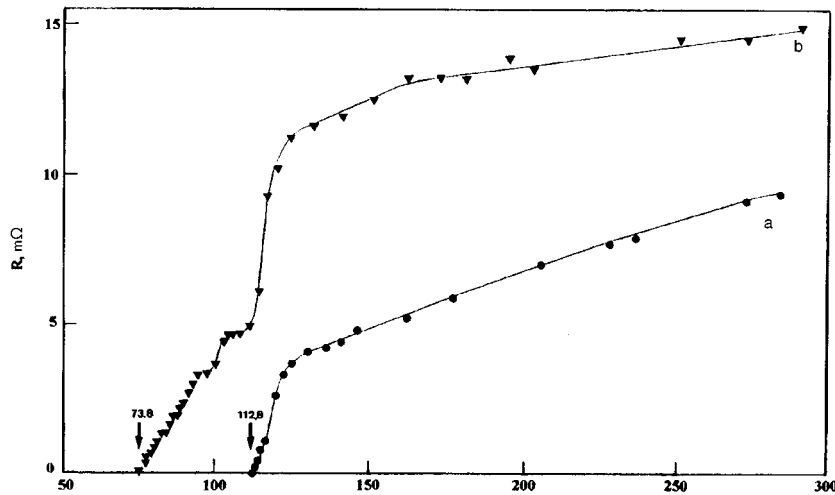


FIG. 2. Temperature dependences of the electrical resistance of $\text{Bi}_{1.6}\text{Pb}_{0.4}\text{Sr}_{1.98}\text{K}_{0.02}\text{Ca}_2\text{Cu}_3\text{F}_{0.8}\text{O}_y$ ceramic after synthesis at $T=845^\circ\text{C}$ for $t=240$ h (curve *a*) and additional annealing in regimes (*b*)–(*f*) (curve *b*).

conducting phases 2223 and 2212, with the 2223 phase predominating ($\sim 67\%$), and traces of impurities in the form of the 2201 phase and the compounds Ca_2PbO_4 , $(\text{Sr}, \text{Ca})_2\text{CuO}_3$, and $(\text{Ca}, \text{Sr})_2\text{PbO}_4$. The lattice parameters determined for the 2223 phase ($a=b=5.398 \text{ \AA}$, $c=36.958 \text{ \AA}$) and 2212 phase ($a=b=5.399 \text{ \AA}$, $c=30.763 \text{ \AA}$) show good agreement with the results of Refs. 1 and 6. Although the results of the x-ray phase analysis indicate that two superconducting phases 2223 and 2212 predominate, the curve $R(T)$ reveals a single superconducting transition with the onset temperature $T_c^{\text{on}}=125 \text{ K}$ and zero resistance temperature $T_c(R=0)=112.8 \text{ K}$, attributed to the 2223 phase (Fig. 2, curve *a*). The enhanced value of $T_c(R=0)$ for this ceramic compared with the undoped ceramic, and the absence of a superconducting transition from the 2212 phase (its content in the sample is $\sim 33\%$, Fig. 1a) may be attributed to the establishment of good bonds among the grains of the 2223 phase in the fluorine-containing ceramic.

It has been established that for the $(\text{Bi}, \text{Pb})\text{-Sr-Ca-Cu-O}$ system, prolonged synthesis in the range $T=845\text{--}855^\circ\text{C}$ promotes an increase in the bulk content of the 2223 phase and increases $T_c(R=0)$ (Refs. 7 and 8). We attempted to improve the phase composition (the volume of the 2223 phase) and the value of $T_c(R=0)$ for this fluorine-containing ceramic by increasing the annealing time (*b*) and sintering at elevated temperatures (*c*)–(*f*), and we obtained the following results. Unlike the undoped ceramic, annealing in regimes (*b*), (*c*), and (*d*) did not produce any substantial changes in the phase composition of the $\text{Bi}_{1.6}\text{Pb}_{0.4}\text{Sr}_{1.98}\text{K}_{0.02}\text{Ca}_2\text{Cu}_3\text{F}_{0.8}\text{O}_y$ ceramic (Fig. 1), and the value of $T_c(R=0)$ decreased to 82.4 K after annealing in regime (*b*). A further increase in the annealing temperature in regimes (*e*) and (*f*) reduced the bulk content of the 2223 phase and increased the concentration of the 2212 phase and the impurity phases in the $\text{Bi}_{1.6}\text{Pb}_{0.4}\text{Sr}_{1.98}\text{K}_{0.02}\text{Ca}_2\text{Cu}_3\text{F}_{0.8}\text{O}_y$ samples. In case (*e*), the percent content of the 2223 and 2212 phases was almost the same and the peaks assigned to the 2201 phases and the compound $(\text{Sr}, \text{Ca})_2\text{CuO}_3$ showed an increase. In case (*f*), only one peak assigned to the 2223 phase, at $2\theta=24.3^\circ$, was observed and the 2212 phase dominated. The intensities of the peaks assigned to the 2201 phase

and the compounds $(\text{Sr}, \text{Ca})_2\text{CuO}_3$ and $(\text{Ca}, \text{Sr})_2\text{PbO}_4$ were also increased. The temperature dependence $R(T)$ of the $\text{Bi}_{1.6}\text{Pb}_{0.4}\text{Sr}_{1.98}\text{K}_{0.02}\text{Ca}_2\text{Cu}_3\text{F}_{0.8}\text{O}_y$ ceramic after all the heat treatment regimes (*b*)–(*f*) (Fig. 2, curve *b*) has a multistage profile with $T_c(R=0)=73.8 \text{ K}$. Although the electrical resistance of the samples exhibits a metallic temperature dependence for $T>T_c$, regardless of the heat treatment regime, the normal-state resistance for a sample annealed at higher temperature (regime (*f*)) is considerably higher than that for a sample synthesized at lower temperature (regime (*a*)). This behavior can be attributed to deterioration in the bond at the grain boundaries of the superconducting phases, as a result of the presence of a large quantity of impurity phases. This is also mainly responsible for the low value of $T_c(R=0)$ for the sample treated in regime (*f*).

To sum up, it has been established as a result of these investigations that the phase composition of $\text{Bi}_{1.6}\text{Pb}_{0.4}\text{Sr}_{1.98}\text{K}_{0.02}\text{Ca}_2\text{Cu}_3\text{F}_{0.8}\text{O}_y$ superconducting ceramic formed after solid-phase synthesis at 845°C for 240 h remains almost unchanged after additional annealing in the range $845\text{--}855^\circ\text{C}$. Annealing at higher temperatures breaks down the 2223 phase, and after annealing at 890°C the 2212 phase predominates. The highest value of $T_c(R=0)=112.8 \text{ K}$ was obtained for samples synthesized at 845°C for 240 h. Further investigations are required to gain a better understanding of the processes involved in the formation of the superconducting phases and superconductivity in a $(\text{Bi}, \text{Pb})\text{-(Sr, K)-Ca-Cu-(O, F)}$ system.

¹X. H. Gao, S. F. Jiang, S. Gao *et al.*, *Physica C* **245**, 66 (1995).

²X. -G. Wang, P. -Y. Hu, Z. -M. Huang *et al.*, *Physica C* **233**, 327 (1994).

³S. Horiuchi, K. Shoda, H. Nozaki *et al.*, *Jpn. J. Appl. Phys.* **28**, L621 (1989).

⁴Z. Tang, S. J. Wang, and X. H. Gao, *Phys. Rev. B* **50**, 3209 (1994).

⁵S. Y. Lee, S. Suehara, and S. Horiuchi, *Physica C* **185–189**, 477 (1991).

⁶X. H. Gao, X. L. Wu, H. Yan *et al.*, *Mod. Phys. Lett. B* **4**, 137 (1990).

⁷V. V. Petrushko, Yu. A. Semenenko, B. V. Novysh, and V. P. Yarusnichev, *Sverkhprovodimost' (KIAE)* **3**, 1670 (1990) [*Superconductors* **3**, 1344 (1990)].

⁸I. E. Arshakyan, N. N. Oleinikov, and Yu. D. Tret'yakov, *Neorg. Mater.* **30**, 824 (1994).

Translated by R. M. Durham

Influence of ionic conductivity on the elastic characteristics of four-component copper and silver chalcogenides

Yu. F. Gorin, N. V. Mel'nikova, E. R. Baranova, and O. L. Kobeleva

A. M. Gorki Ural State University, Ekaterinburg

(Submitted March 5, 1997)

Pis'ma Zh. Tekh. Fiz. **23**, 35–39 (July 26, 1997)

The relation between the ultrasonic characteristics and the ionic conductivity produced by Cu^+ and Ag^+ ions has been investigated in four-component CuGeAsS_3 and AgGeAsSe_3 chalcogenides. It is shown that the temperature range where ionic conductivity appears corresponds to the onset of a rapid decrease in the ultrasound velocity. © 1997 American Institute of Physics. [S1063-7850(97)02407-5]

Multicomponent silver and copper chalcogenides are promising materials for microelectronics, optoelectronics, and radioelectronics, since they combine semiconducting properties with ionic, ferroelectric, and other interesting properties. Studies of three- and four-component compounds of silver and copper such as $(\text{GeC})_{1-x}(\text{ABC}_2)_x$, where $A = \text{Cu, Ag}$, $B = \text{As, Sb}$, and $C = \text{S, Se}$, and others, require a multiple-technique approach. The electrical properties of these compounds and investigations of the ultrasonic characteristics in three-component compounds have been reported.¹⁻⁹ Here we study the elastic characteristics of the polycrystalline compounds CuGeAsS_3 and AgGeAsSe_3 .

The compounds CuGeAsS_3 and AgGeAsSe_3 are mixed

(electronic-ionic) conductors where the conduction is produced by the Cu^+ and Ag^+ ions, respectively.^{6,5} By studying the impedance and admittance over a wide frequency range (10^2 – 10^{-5} kHz), it was possible to determine a frequency range which characterized the bulk properties of the compounds. The temperature dependences of the electrical conductivity and the permittivity in the range 78–600 K were measured at a frequency of 1.592 kHz, which lies within this range. The temperature dependences of the electrical conductivity of polycrystalline CuGeAsS_3 and AgGeAsSe_3 are plotted in Fig. 1. A characteristic feature of these curves is the presence of two regions (a low-temperature and a high-temperature region) with different activation energies. The

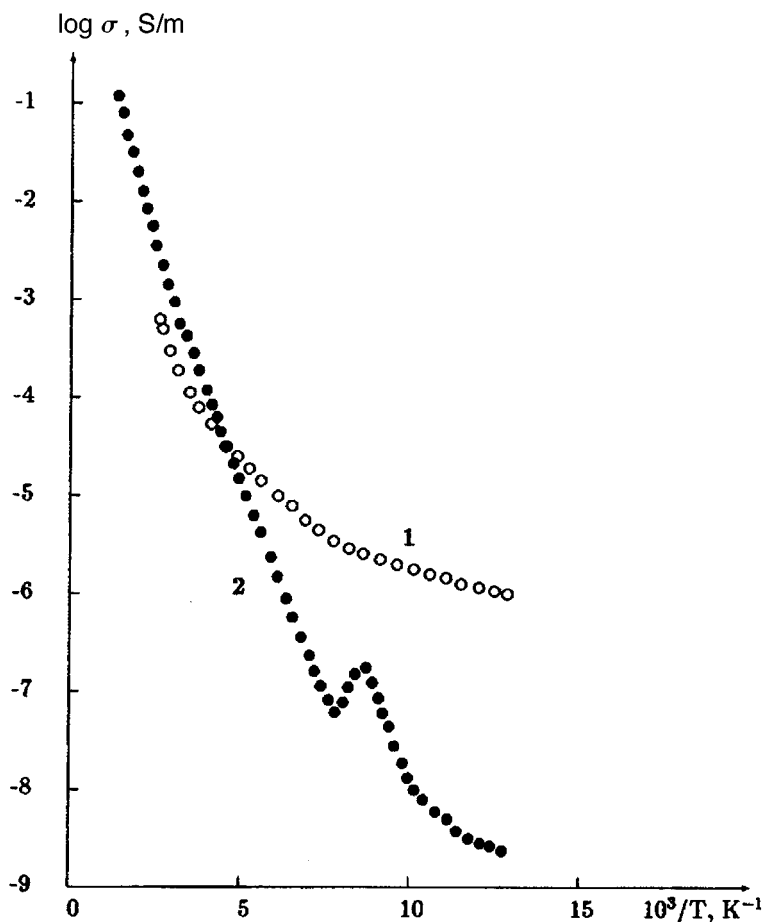


FIG. 1. Temperature dependence of the electrical conductivity of polycrystalline CuGeAsS_3 (1) and AgGeAsSe_3 (2).

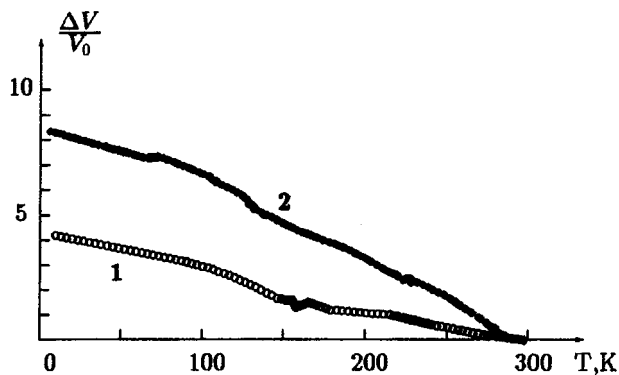


FIG. 2. Temperature dependence of the relative change in the velocity of sound for transverse waves in polycrystalline CuGeAsS_3 (1) and AgGeAsSe_3 (2).

low-temperature regions correspond to the electronic conduction while the high-temperature regions with higher activation energies, correspond to ionic or mixed conduction. The existence of ionic transport in CuGeAsS_3 and AgGeAsSe_3 was confirmed by measurements of the electrical conductivity using filters for the Cu^+ and Ag^+ ions; the filters were $5\text{CuCl} \cdot 3\text{RbCl}$ as an ionic conductor for Cu^+ ions and Ag_4RbI_5 for Ag^+ ions. For polycrystalline AgGeAsSe_3 the temperature dependences of the electrical conductivity and the permittivity revealed anomalies near 114–138 K (Ref. 5), which are considered to be the result of a structural phase transition. The temperature range in which ionic transport becomes appreciable was estimated from the temperature at which the conductivity began to increase rapidly. More accurate confirmation of this result was provided by investigating the permittivity of CuGeAsS_3 and AgGeAsSe_3 .

The temperature range in which ionic transport becomes appreciable is 110–130 K for CuGeAsS_3 and 140–150 K for AgGeAsSe_3 . At 300 K the ionic component accounts for 15% of the total conductivity in CuGeAsS_3 and 95% in x-ray amorphous AgGeAsSe_3 .

The acoustic properties of polycrystalline CuGeAsS_3 and AgGeAsSe_3 were investigated by a phase-pulse method. The propagation velocity of ultrasonic waves in the sample was measured in the temperature range 300–6 K (under cooling), where the longitudinal wave frequency was 5 MHz and the transverse frequency was 2.5 MHz. The temperature dependences of the relative change in the velocity of sound for transverse waves in polycrystalline CuGeAsS_3 and AgGeAsSe_3 are plotted in Fig. 2. Table I gives the velocities

TABLE I. Ultrasonic wave velocities at 297 K, elastic constants, and Debye temperatures for CuGeAsS_3 and AgGeAsSe_3 .

Compound	V_l , m/s	V_t , m/s	Shear modulus, N/m^2	Elastic modulus, N/m^2	θ_D , K
CuGeAsS_3	3420	2400	2.0×10^{10}	2.5×10^{10}	492
AgGeAsSe_3	1830	1380	1.1×10^{10}	0.6×10^{10}	286

of the longitudinal V_l and transverse V_t waves at 297 K, together with the shear moduli, elastic moduli, and Debye temperatures for these compounds.

The temperature dependence of the relative change in the velocity of sound for transverse waves in CuGeAsS_3 typically exhibits kinks around 145–165 K and an abrupt decrease in the velocity of the ultrasonic waves in the range 116–145 K. The onset of appreciable ionic transport in this compound is observed at 110–130 K. Thus, the temperature range in which the ionic conduction becomes appreciable corresponds to the onset of a faster decrease in the ultrasound velocity. The establishment of ionic conduction, indicating a softening of the crystal lattice, precedes the kinks on the temperature curve of the relative change in the velocity of sound in the CuGeAsS_3 sample, which are associated with structural changes in the crystal lattice (with no change in the symmetry system).

The temperature curve of the relative change in the velocity of transverse ultrasonic waves in AgGeAsSe_3 has a kink near 70 K and this is followed by a more rapid decrease (with increasing temperature) in the velocity of sound in the range 115–135 K. The temperature range in which these changes occur coincides with the region of anomalous behavior (the existence of a peak) of the electrical conductivity and the permittivity (114–138 K) in this compound. This kink on the curve at $T \sim 70$ K, the decrease in the velocity of the ultrasonic waves, and the anomalies in the electrical properties at 114–138 K are clearly the consequence of structural phase transitions, which then give rise to appreciable ionic conduction. Thus, if the kink observed at $T \sim 130$ K on the curve giving the relative change in the ultrasound velocity is considered to be the consequence of changes taking place in the crystal lattice (loosening), it may be postulated that the ionic conduction appears at $T \sim 130$ K and becomes appreciable at 140–150 K. It has been noted that the temperature for the onset of appreciable ionic transport was estimated by studying the behavior of the electrical conductivity and the permittivity.

To conclude, we note that in CuGeAsS_3 and AgGeAsSe_3 a correlation has been observed between the onset of ionic conduction and the relative change in the velocity of sound with increasing temperature. Clearly, ultrasonic investigations may be a method of establishing the temperature range in which ionic migration occurs, at least for some types of ionic semiconductors.

¹S. V. Karpachev, G. M. Zlokazova, L. Ya. Kobelev, and V. B. Zlokazov, Dokl. Akad. Nauk SSSR **303**, 349 (1988) [Sov. Phys. Dokl. **33**, 833 (1988)].

²Yu. F. Gorin, A. N. Babushkin, L. Ya. Kobelev, and A. S. Savel'kaev, JETP Lett. **41**, 521 (1985).

³Yu. F. Gorin, A. N. Babushkin, L. Ya. Kobelev, and Yu. S. Kuznetsov, Fiz. Tverd. Tela (Leningrad) **25**, 922 (1983) [Sov. Phys. Solid State **25**, 531 (1983)].

⁴Ye. R. Baranova, V. B. Zlokazov, L. Ya. Kobelev, and M. V. Perfil'ev, Acta Crystallogr. A **46**, Suppl., C-363 (1990).

⁵E. R. Baranova, V. B. Zlokazov, and M. V. Perfil'ev, Impedance (10^2 – 10^{-5} kHz) and Temperature Dependence of the Electrical Conductivity and Permittivity of AgGeAsSe_3 [in Russian] (Urals University Press, Sverdlovsk, 1989).

⁶V. B. Zlokazov, N. V. Mel'nikova, E. R. Baranova, M. V. Perfil'ev, and L. Ya. Kobelev, Elektrokimiya **28**, 1523 (1992).

⁷E. R. Baranova, V. L. Kobelev, O. L. Kobeleva, N. V. Melnikova, V. B. Zlokazov, L. Ya. Kobelev, and M. V. Perfiliev, *Proceedings of the Tenth International Conference on Solid State Ionics*, Singapore, 1995, p. 20.
⁸N. V. Mel'nikova, L. Ya. Kobelev, and V. B. Zlokazov, *Pis'ma Zh. Tekh. Fiz.* **21**(1), 9 (1995) [*Tech. Phys. Lett.* **21**, 3 (1995)].

⁹E. R. Baranova, V. B. Zlokazov, L. Ya. Kobelev, and M. V. Perfil'ev, *Pis'ma Zh. Tekh. Fiz.* **16**(10), 27 (1990) [*Sov. Tech. Phys. Lett.* **16**, 372 (1990)].

Translated by R. M. Durham

Influence of spheroidal deformation on the stability of a drop charged below the Rayleigh limit

V. A. Koromyslov, Yu. D. Rakhmanova, and S. O. Shiryayeva

Yaroslavl' State University

(Submitted March 21, 1997)

Pis'ma Zh. Tekh. Fiz. **23**, 40–43 (July 26, 1997)

The principle of minimization of the potential energy of an isolated drop of an ideally conducting, nonviscous liquid is used to show that a deformed drop charged below the Rayleigh limit can become unstable. © 1997 American Institute of Physics. [S1063-7850(97)02507-X]

The theory of thunderstorm electricity must take into account liquid droplets charged below the Rayleigh limit which, under normal conditions, are stable with respect to their own charge. However, it is known¹ that on account of aerodynamic conditions, around 40% of cloud droplets have an elongated spheroidal shape. It is therefore interesting to determine the influence of spheroidal deformation on the critical conditions for the buildup of instability for a drop charged below the Rayleigh limit.

We consider an elongated spheroidal charged drop of ideal liquid with surface charge Q , surface tension σ , and an equivalent spherical volume of radius R . This drop will have the energy

$$U = \frac{Q^2}{2C} + \sigma S, \quad (1)$$

$$C = \frac{\sqrt{a^2 - b^2}}{\cosh^{-1}(a/b)}, \quad S = 2\pi ab \sqrt{1 - e^2} + \frac{\sin^{-1} e}{e},$$

$$e = \frac{\sqrt{a^2 - b^2}}{a},$$

where C is the volume of the elongated spheroid, S is its surface area, and e is its eccentricity. Obviously, the volume of the drop does not change during the deformation process:

$$V = \frac{4}{3} \pi R^3 = \frac{4}{3} \pi ab^2 = \text{const.} \quad (2)$$

As a result of virtual, infinitely slow elongation, a drop may spontaneously decay into two, three, and so on, daughter drops.²⁻⁴ Another decay mechanism is also possible,^{5,6} whereby an increase in the charge density at the tips of the spheroid causes instability of high-order capillary-wave modes which form emitting protuberances at the tips, from which excess charge begins to be ejected in the form of numerous, highly disperse, strongly charged droplets. The dependence of the total potential energy U of a spheroidal droplet on the eccentricity e has two minima: the first corresponds to an undeformed spherical droplet and the second to a droplet at the decay surface. It is logical to assume that the maximum energy is obtained for that eccentricity at which one of the decay mechanisms is initiated.²⁻⁶

Let us find the eccentricity e of the drop at this point.

Expressions (1) and (2) yield an expression for the potential energy of an elongated, charged spheroidal drop:⁷

$$U = \frac{Q^2}{2R} \cosh^{-1}(1 - e^2)^{-1/2} \frac{(1 - e^2)^{-1/3}}{e} + 2\pi R^2 \times \left[(1 - e^2)^{1/3} + \frac{\sin^{-1} e}{e(1 - e^2)^{1/6}} \right]. \quad (3)$$

In order to obtain the extremum of the eccentricity for a drop which is still stable with respect to its own charge but is located at the rupture surface, we equate to zero the derivative of the energy U with respect to the eccentricity e , and then after various simple transformations, we can obtain the critical value of the Rayleigh parameter $W = Q^2/16\pi\sigma R^3$ characterizing the stability of the drop, as a function of the eccentricity:

$$W = \frac{1}{4} \left((2e^2 - 3)e + \frac{\sin^{-1} e}{(1 - e^2)^{1/2}} (3 - 4e^2) \right) \times (3e - \cosh^{-1}(1 - e^2)^{-1/2} (3 - e^2))^{-1}. \quad (4)$$

Figure 1 gives the curve $W = W(e)$ calculated according to formula (4). Points lying in the area below this curve correspond to the values of the Rayleigh parameter for which the drop remains stable under spheroidal deformation while points lying above this curve correspond to those values for which the drop will be unstable under this deformation. It can be seen that for values of the Rayleigh parameter

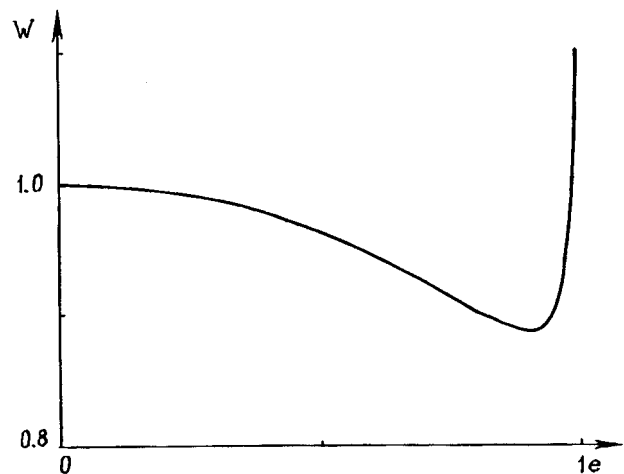


FIG. 1. Critical Rayleigh parameter W for the fission of a highly deformed charged droplet as a function of the eccentricity e : $W = W(e)$. The unstable states lie above this curve.

$W \geq 1$, the drop will be unstable for any eccentricity. For $W \leq 0.89$, the drop cannot undergo spontaneous decay as a result of the buildup of electrohydrodynamic instability.

We therefore postulate that the decay of a drop charged below the Rayleigh limit will take place by the usual²⁻⁵ scenario: after a certain virtual deformation has been attained, the drop begins to stretch spontaneously until it reaches the eccentricity $e \approx 0.8$ (Ref. 6) after which, depending on the viscosity,³ the drop either decays into several parts of comparable size or it decays by emitting numerous, highly charged, highly disperse droplets.

¹I. P. Mazin, A. Kh. Khr̄gian, and I. M. Imyanitov, *Handbook of Clouds and Cloud Atmospheres* [in Russian] (Gidrometeoizdat, Leningrad).

²A. I. Grigor'ev, S. O. Shiryayeva, I. D. Grigor'eva, A. É. Lazaryants, and E. I. Mukhina, *Zh. Tekh. Fiz.* **61**(4), 25 (1991) [*Sov. Phys. Tech. Phys.* **36**, 385 (1991)].

³V. A. Koromyslov and I. D. Grigor'eva, *ÉOM*, No. 3, 55 (1995).

⁴A. I. Grigor'ev and S. O. Shiryayeva, *Zh. Tekh. Fiz.* **61**(3), 19 (1991) [*Sov. Phys. Tech. Phys.* **36**, 258 (1991)].

⁵A. I. Grigor'ev and S. O. Shiryayeva, *J. Phys. D.* **23**, 1361 (1991).

⁶G. Taylor, *Proc. R. Soc. London* **280**, 383 (1964).

⁷L. D. Landau and E. M. Lifshitz, *Electrodynamics of Continuous Media*, transl. of 1st Russian ed. (Pergamon Press, Oxford, 1960) [Russ. original, Nauka, Moscow, 1992].

Translated by R. M. Durham

Anomalously high rate of grain boundary displacement under fast shear loading

S. G. Psakh'e and K. P. Zol'nikov

Institute of Physics of Strength of Materials and Materials Science, Siberian Branch of the Russian Academy of Sciences, Tomsk

(Submitted March 19, 1997)

Pis'ma Zh. Tekh. Fiz. **23**, 44–48 (July 26, 1997)

A computer simulation is made of the grain boundary behavior in an aluminum sample under conditions of fast shear loading. The calculations are made using a molecular dynamics method and pseudopotential theory. It is observed that under these loading conditions, the grain boundaries may undergo displacement at an anomalously high speed, even exceeding the rate of the applied shear. The atomic mechanisms responsible for this effect are investigated.

© 1997 American Institute of Physics. [S1063-7850(97)02607-4]

Studies of the response of a material under exposed to high-energy action are of considerable interest from the scientific viewpoint and from the viewpoint of materials technology. Anomalously high rates of mass transport, flow of materials without resistance, and so forth, may take place in materials exposed to severe shear deformation.^{1–7} Simulation of fast shear has revealed various important characteristics.^{8–10} For instance, in materials containing a special type of grain boundaries, shear loading induces a vortex-like collective motion of atoms near the grain boundary. Under these conditions, the largest displacements of grain-boundary atoms are observed perpendicular to the direction of shear. It was observed in Ref. 11 that fast mechanical loading leads to the formation and propagation of soliton-like pulses in the material. These pulses showed up most clearly at low temperatures and their interaction with structural defects could result in the formation of so-called hot spots,^{12,13} — local regions where the temperature is higher than the average over the sample.

In this paper we study the influence of fast loading on the change in the microstructure of the grain boundaries. We simulated an isolated well-tested grain boundary and we studied its structural rearrangements and the atomic mechanisms responsible for the characteristics of the response.

As in Refs. 8–12, the simulation was performed using the unique MONSTER-MD software, based on the molecular dynamics method. The object of the simulation was a three-dimensional aluminum crystallite containing a special $\Sigma 7$ type of grain boundary with the X, Y, and Z coordinate axes oriented in the [111], [2 $\bar{1}$ 1], and [011] crystallographic directions, respectively.

We used the system of atomic units, conventionally adopted to perform calculations at the microscopic level.¹⁴ The dimensions of the sample in the X, Y, and Z directions were 167 a.u., 65 a.u., and 40 a.u., respectively. The grain boundary was located in the middle of the sample perpendicular to the X axis. The sample contained about 4000 atoms. Periodic boundary conditions were used in the Y and Z directions and a shear load was applied along the edges of the sample in the direction of the X axis at the rate

$$V_x = V_z = 0;$$

$$V_y^l = -V_y^r = -2.5 \times 10^{-5} \text{ a.u. } (\approx 50 \text{ m/s}),$$

where V_y^l and V_y^r are the y-components of the rates on the left and right sides of the sample, respectively.

The interaction between the atoms was described in the pair approximation using the pseudopotential theory, as in Ref. 15. Prior to the simulation of mechanical loading, the crystallite was thoroughly relaxed.

The calculations showed that under the action of this type of load, vortex-like atomic motion occurs in the intergranular region^{8–10} and the boundary begins to move along the X axis. The position of the grain boundary and the structure of one of the atomic layers perpendicular to the Z axis is shown in Fig. 1. Similar behavior of the atomic structure is observed for all the other atomic planes of the crystallite. Note that as the grain boundary moves along the sample, it

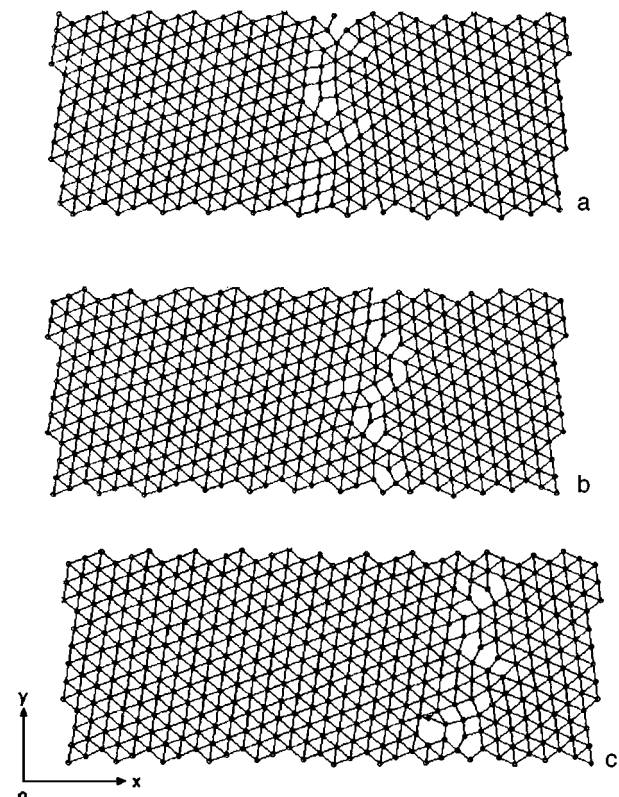


FIG. 1. Position of grain boundary for one of the atomic planes at various times: a — $t = 0$, b — $t = 120\,000$ a.u., and c — $t = 250\,000$ a.u.

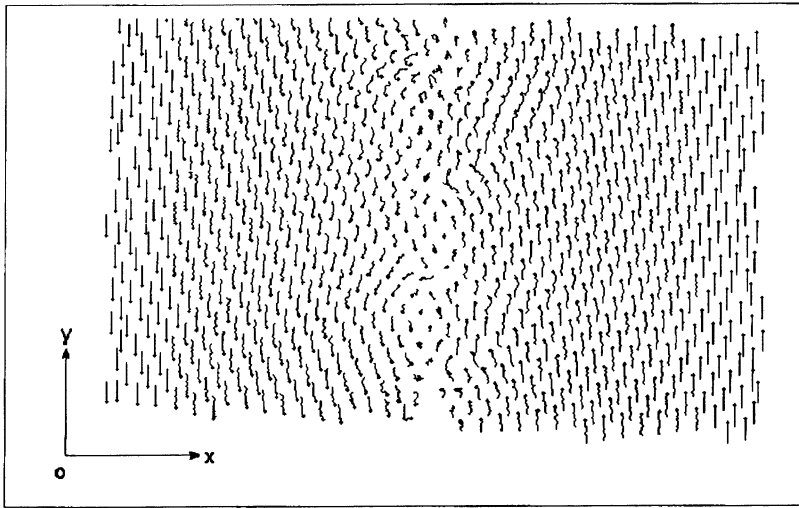


FIG. 2. Trajectories of atomic motion for three atomic planes over the time interval $0 < t < 80\,000$ a.u.

slows down and stops near a “trap” in the sample. These test calculations showed that when the direction of the shear load is reversed, the boundary moves in the opposite direction. Note that under this type of action, all the atomic displacements in the grain boundary region are matched to each other. Estimates of the rate of grain boundary displacement show that this is anomalously high (up to 600 m/s), i.e., it is higher than the rate of shear loading.

An analysis of the atomic trajectories, velocity fields, and crystallite structure in various time intervals indicates that the processes taking place in the sample under this action exhibit clearly defined nonlinear behavior (Fig. 2).

The analysis showed that the growth of a single grain as a result of displacement of the grain boundary is based on cooperative, group displacements of atoms. This corresponds to the correlated nonlinear motion of groups of atoms, where the displacement of each individual atom is fairly small, as can be seen clearly from Fig. 1.

To sum up, computer simulation has been used for the first time to demonstrate anomalously high rates of grain boundary displacement under conditions of fast shear loading. Similar conditions may be created in materials, not only under extreme operating conditions, but also under normal conditions, as a result of the heterogeneity of the material in zones of concentrated stress, and also during the crack propagation and the formation of various types of discontinuities, where local fast shear deformations may occur in the sample. This grain boundary behavior may have a substantial influ-

ence on changes in the microstructure of the material and consequently, on its properties and behavioral characteristics.

- ¹N. S. Enikolopyan, Dokl. Akad. Nauk SSSR **251**, 283 (1985).
- ²N. S. Enikolopyan, Zh. Fiz. Khim. **63**, 2289 (1989).
- ³V. V. Boldyrev, Izv. Akad. Nauk SSSR Ser. Khim. **10**, 2238 (1990).
- ⁴S. G. Psakh'e and S. Yu. Korostelev, in *Structural Levels of Plastic Deformation and Damage*, edited by V. E. Panin, Yu. V. Grinyaev, V. I. Danilov *et al.* [in Russian] (Nauka, Novosibirsk, 1990), pp. 204–231.
- ⁵V. E. Panin, V. E. Egorushkin, Yu. A. Khon, and T. F. Elsukova, Izv. Vyssh. Uchebn. Zaved. Fiz. No. 12, 5 (1982).
- ⁶V. E. Panin, Yu. I. Meshcheryakov, T. F. Elsukova, A. K. Divakov, S. G. Psakh'e, and M. M. Myshlyaev, Izv. Vyssh. Uchebn. Zaved. Fiz. No. 2, 107 (1990).
- ⁷V. E. Panin, *Physical Mesomechanics and Computer-Aided Design of Materials* [in Russian] (Nauka, Novosibirsk, 1995), pp. 7–49.
- ⁸S. G. Psakh'e, S. Yu. Korostelev, S. I. Negreskul, K. P. Zol'nikov, Z. Wang, and Sh. Li, Pis'ma Zh. Tekh. Fiz. **20**(1), 36 (1994) [Tech. Phys. Lett. **20**, 17 (1994)].
- ⁹S. G. Psakh'e, S. Yu. Korostelev, S. I. Negreskul, K. P. Zol'nikov, Z. Wang, and S. Li, Phys. Status Solidi B **176**, K41 (1993).
- ¹⁰K. P. Zol'nikov, S. G. Psakh'e, S. I. Negreskul, and S. Yu. Korostelev, J. Mater. Sci. Technol. **12**, 235 (1996).
- ¹¹S. G. Psakh'e, K. P. Zol'nikov, and S. Yu. Korostelev, Pis'ma Zh. Tekh. Fiz. **21**(13), 1 (1995) [Tech. Phys. Lett. **21**, 489 (1995)].
- ¹²S. G. Psakh'e, K. P. Zol'nikov, and D. Yu. Saraev, Pis'ma Zh. Tekh. Fiz. **22**(10), 6 (1996) [Tech. Phys. Lett. **22**, 389 (1996)].
- ¹³D. H. Tsai, J. Chem. Phys. **95**, 7497 (1991).
- ¹⁴W. A. Harrison, *Pseudopotential in the Theory of Metals* (Benjamin, New York, 1966).
- ¹⁵S. G. Psakh'e and V. E. Panin, Fiz. Met. Metalloved. **50**, 620 (1980).

Translated by R. M. Durham

Characteristics of an electric circulation module for pulse-periodic ArF*, KrF*, and XeF* molecular lasers

A. K. Shuaibov, L. L. Shimon, A. I. Minya, and A. I. Dashchenko

Uzhgorod State University

(Submitted March 4, 1997)

Pis'ma Zh. Tekh. Fiz. **23**, 49–55 (July 26, 1997)

The characteristics of an electric circulation module for a miniature, pulse-periodic, inert-gas fluoride laser utilizing He/(Ar, Kr, Xe)/F₂ mixtures at a pressure of 100–350 kPa have been investigated and results are presented. It is shown that a positive dc voltage is optimum for supplying the electric circulation module. The lasing zone of a negative corona discharge is of interest for developing simple high-pressure excimer lamps with a self-circulating active medium. © 1997 American Institute of Physics. [S1063-7850(97)02707-9]

The authors of Ref. 1 reported the use of electrically driven circulation of the active media in pulse-periodic N₂ and XeCl* lasers, which allowed the pulse repetition rate to be increased to 70 Hz with an average gas transverse flow velocity $v \leq 3$ m/s. This circulation was based on using a corona discharge in a "tip-grid" electrode system whose entire length is comparable with the length of the laser active medium. The gas circulation velocity $v \propto (I)^{1/2}$ (Ref. 2) (where I is the average corona discharge current) is limited by the buildup of corona discharge instability. In Ref. 3, we studied the characteristics of a similar corona discharge in a He/Xe/HCl mixture, which showed that the current of an uncontracted corona discharge could be varied widely by varying the pressure and composition of the active medium in an XeCl* laser. Since the active media of inert-gas fluoride electric-discharge lasers (utilizing He/R/F₂ mixtures where R=Ar, Kr, or Xe) are particularly corrosive and are characterized by more stringent requirements on the purity of the active mixtures, it is of particular interest to use electrically driven circulation in these systems.

Here we present results of an investigation of the operating regimes of an electric circulation module for a miniature pulse-periodic laser utilizing inert-gas monofluorides.

1. A corona discharge was investigated using the apparatus described in Refs. 3 and 4. The system of corona discharge electrodes consisted of a single row of tips and a nickel grid and was 11 cm long. The tip density in the row was one tip per centimeter. The grid contained cells of 0.1×0.1 cm and was made of 0.03 cm diameter wire. The interelectrode gap in the system of corona discharge electrodes was 2 cm. The electrode system was removed from the discharge chamber of the laser emitter and was mounted in a separate high-pressure chamber fitted with CaF₂ windows. A negative or positive dc voltage was supplied to the tips via a limiting resistance $R = 1-3$ MΩ.

The current-voltage and frequency characteristics of positive and negative corona discharges in He/R/F₂ mixtures were investigated at pressures of 100–350 kPa. Emission spectrum analysis was used to study the qualitative composition of the plasma in the lasing zones of these corona discharges.

2. Negative and positive corona discharges both consisted of a lasing zone, positioned at the ends of the tips, and

a dark outer region. The lasing zone of the corona discharge was continuous and did not consist of a set of point lasing zones (formed alongside each tip) similar to the lasing zone of the corona discharge in the active medium of an XeCl* laser.³ The lasing zone in the corona discharge in He/R/F₂ mixtures consisted of a bright plasma filament 11 cm long and 0.5–1.0 cm in diameter. The emission from the lasing zone of the negative corona discharge was particularly intense. The transverse dimensions of the lasing zone of the corona discharge increased with increasing voltage on the tips. Above a certain critical voltage, an anode or cathode streamer appeared alongside one of the tips and the corona discharge contracted.

The current-voltage characteristics of the corona discharge are plotted in Fig. 1. For active media having the same composition and pressure, the current-voltage characteristics of the positive and negative corona discharges had quite different ignition potentials but the limiting currents of the noncontracted discharge stage were approximately the same. A positive corona discharge was more favorable at lower supply voltages ($U \leq 10$ kV) and a negative discharge was favorable at higher U . An increase in the He pressure to 300–350 kPa resulted in an increase in the ignition potentials and extended the range of operating pressures. The current-voltage characteristics of He/R/F₂ mixtures were nearly linear and differed appreciably from the quadratic curves $I = \alpha(U - U_0)^2$ of a corona discharge⁵ (where α is a constant and U_0 is the discharge ignition potential), which are most typical of a classical corona discharge. This difference was caused by the nonlinearities of a corona discharge in inert gases⁶ for which the discharge becomes intermediate between a corona and a glow discharge.

3. For a corona discharge in electropositive gases (He/N₂ mixture), the discharge was mainly continuous and the maximum current at the noncontracted stage was determined by the ballast resistance, reaching 2–3 mA (Ref. 7). When the mixture contained strongly electronegative molecules, the current flow regime of the negative corona discharge was purely pulsed, whereas in a positive corona discharge the current consisted of continuous and pulsed components. Typical profiles of corona discharge current pulses are shown in Fig. 2. The half-height duration of the corona discharge

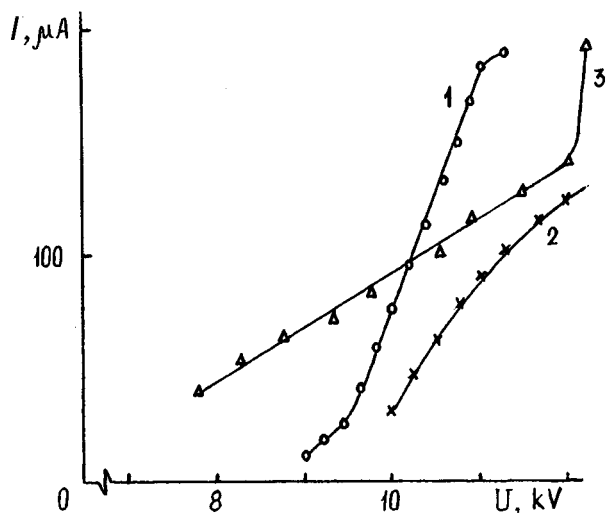


FIG. 1. Current-voltage characteristics of negative (1, 2) and positive (3) corona discharges in the following mixtures: 1, 3 — He/Kr/F₂ = 200/6, 4/0, 8 kPa, 2 — He/Ar/F₂ = 190/17, 6/0, and 8 kPa.

current pulses was 0.2–0.3 μs, with a rise time of ≤50 ns and a decay time of 1.0 μs.

Dependences of the current pulse repetition rate on the magnitude and polarity of the voltage on the tips are plotted in Fig. 3. With increasing supply voltage, the pulse repetition rate of the positive corona discharge current increased quadratically whereas similar dependences for a negative corona discharge were linear. The pulse repetition rate of the negative corona discharge current was in the range 1–40 kHz whereas that for the positive corona discharge reached 160 kHz. The upper limits of the pulse repetition rate for the negative corona discharge were determined by the mobility of the positive R⁺ (R₂⁺) ions screening the negative tips of the tips.⁸ As the atomic weight of the inert gases is decreased, the limiting pulse repetition rate increases, reaching 80–90 kHz in a He/F₂ mixture. In a positive corona dis-

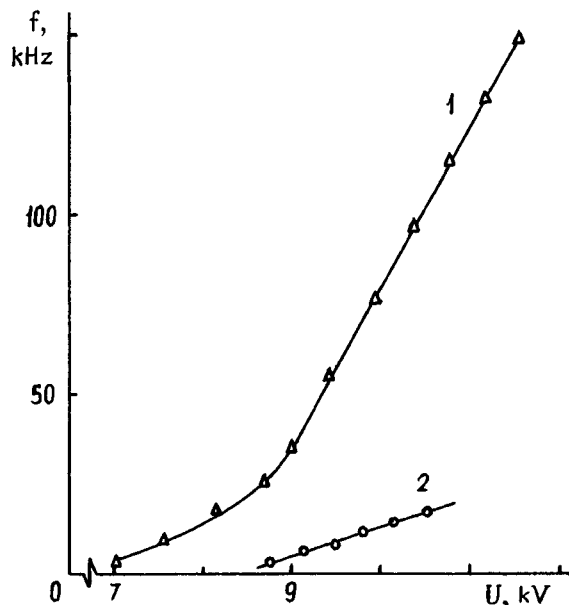


FIG. 3. Profile of positive (1) and negative (2) corona discharge current pulses in an He/Kr/F₂ mixture.

charge the pulse repetition rate is probably determined by the mobility of the negative F⁻ ions screening the positive ends of the tips in the electrode system. The continuous component of the positive corona discharge current is probably a flux of positive inert-gas ions, but the density of negative ions is not sufficiently high to completely block the interelectrode gap in this corona discharge.

4. An investigation of the overall emission spectrum of the lasing zone of the corona discharge revealed that this is a selective source of 193 nm ArF*, 249 nm KrF*, and 351 nm XeF* radiation. In the visible range we observed selective filling of some *p*-states of heavy inert-gas atoms due to the Ar(4*s*–5*p*), Kr(5*s*–6*p*), and Xe(6*s*–7*p*) transitions in the blue-green. This radiation determined the color of the corona-discharge lasing zone, but its intensity was approximately two orders of magnitude lower than that of the excimer-band radiation. Thus the lasing zone of a negative corona discharge may be used to develop simple sources of ultraviolet radiation from inert-gas fluorides with a self-circulating active medium. These sources of ultraviolet radiation exhibit enhanced sensitivity.

To conclude, our investigation of the operating conditions of an electric circulation module for a pulse-periodic laser utilizing inert-gas monofluorides has shown that for a corona discharge in He/R/F₂ mixtures, it is best to use a positive voltage since the discharge current is mainly continuous and its ignition potentials are lower than those for a negative corona discharge. The lasing zone of the corona discharge is continuous, which helps to produce a more uniform flow of gas mixture beyond the grid. In addition, RF(B) molecules are efficiently formed in the lasing zone of a negative corona discharge which may be utilized to develop simple sources of ultraviolet radiation for biomedical applications.

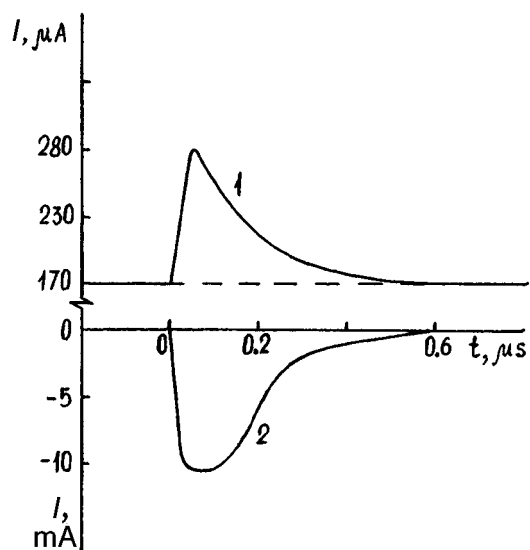


FIG. 2. Pulse repetition rate of corona discharge current in He/Kr/F₂ as a function of positive (1) and negative (2) supply voltages.

- ¹A. I. Baranov, K. V. Gurkov, V. F. Tarasenko *et al.*, *Prib. Tekh. Éksp.* No. 4, 108 (1994).
- ²I. P. Vereshchagin, *Corona Discharge in Electron-Ion Technology Systems* [in Russian] (Énergoatomizdat, Moscow, 1986).
- ³A. K. Shuaibov, L. L. Shimon, and I. V. Shevera, *Kvantovaya Élektron* (Moscow, 1997) (in press).
- ⁴A. K. Shuaibov and I. V. Shevera, *Zh. Prikl. Spektrosk.* **64**, 246 (1997).
- ⁵P. L. Henson, *J. Appl. Phys.* **52**, 709 (1981).
- ⁶A. A. Belevtsev and L. M. Biberman, *Beitr. Plasmaphys.* **23**, 303 (1983).
- ⁷A. K. Shuaibov, A. I. Minya, V. V. Zvenigorodskii, and V. S. Shevera, *Pis'ma Zh. Tekh. Fiz.* **22**(13), 73 (1996) [*Tech. Phys. Lett.* **22**, 551 (1996)].
- ⁸É. D. Lozanskiĭ and O. B. Firsov, *Spark Theory* [in Russian] (Moscow, 1975).

Translated by R. M. Durham

White-light interferometry with depolarization of the radiation

É. I. Alekseev and E. N. Bazarov

Institute of Radio Engineering and Electronics, Russian Academy of Sciences, Fryazino

(Submitted January 20, 1997)

Pis'ma Zh. Tekh. Fiz. **23**, 56–60 (July 26, 1997)

It is shown that the precision of white-light interferometers with a single-mode fiber linking the sensing and processing interferometers can be enhanced by incorporating discrete or all-fiber "time-average" radiation depolarizers (Billings depolarizers). Relations are given to describe the dependence of the output signal and the "zero" drift of white-light interferometers on the polarization characteristics of the optical channel. Relations are also presented for the elements of the Jones matrix of a Billings depolarizer. © 1997 American Institute of Physics. [S1063-7850(97)02807-3]

1. White-light interferometry is one of the most rapidly developing directions in modern optical metrology.¹⁻³ Thus the search for methods of improving the precision of white-light interferometers is of major practical interest. A typical white-light interferometer (see Fig. 1a) consists of a source of wide-band radiation 1, two highly unbalanced interferometers 2 and 5, linked by a section of single-mode optical fiber 3, and a photodetector 6. Until recently it was usually assumed that the transmission (polarization) characteristics of the single-mode fiber link do not affect the precision of white-light interferometers. However, it was shown in Ref. 4 that in white-light interferometers, as in other single-mode fiber interferometers, variations in the polarization characteristics of single-mode fiber waveguides give rise to "zero" drift and fading of the output signal. A method of eliminating the influence of the polarization characteristics of the single-mode fiber link in "reflective" white-light interferometers with a Michelson sensing interferometer was proposed in Ref. 5. In this article we show that the precision of white-light interferometers can also be enhanced by incorporating a discrete or fiber-optic Billings depolarizer.^{6,7}

2. A Billings depolarizer (a monochromatic radiation depolarizer or "time-average" depolarizer) consists of two sequential bulk⁶ or fiber⁷ linear phase plates whose fast axes are turned through 45° relative to each other. The relative phase delays in these linear phase plates vary with time in such a way that incoming completely polarized radiation with the coherence matrix ρ_{in} becomes unpolarized "averaged over time," with the coherence matrix

$$\overline{\rho_{out}} = \overline{D(t)\rho_{in}\tilde{D}(t)} = \frac{1}{2}IE. \quad (1)$$

Here I is the total radiation intensity, D is the Jones matrix of the depolarizer, E is the unit matrix, the tilde denotes Hermitian conjugation, and the bar indicates time averaging. It follows from formula (1) that the elements of the matrix D satisfy the relations

$$\overline{D_{ik}(t)D_{je}^*(t)} = \frac{1}{2}\delta_{ij}\delta_{kl}, \quad (2)$$

where the asterisk indicates complex conjugation, and δ_{ij} and δ_{kl} ($i, j, k, l = 1, 2$) are Kronecker deltas.

A direct consequence of formula (2) is the equality

$$\overline{D(t)\sigma\tilde{D}(t)} = \frac{1}{2}(\text{Tr}\sigma)E. \quad (3)$$

Here σ is an arbitrary, constant or slowly time-varying 2×2 matrix, and Tr denotes the trace of a matrix.

3. Let us assume that the radiation source in the white-light interferometer has unit intensity and the line profile $\Phi(\omega)$ normalized to unity, with the average frequency ω_0 and width $\Delta\omega$ ($\Delta\omega/\omega_0 \ll 1$). The photodetector current at the exit from the white-light interferometer is then given by

$$i = \langle m_0 [1 + (2|m_1|/m_0)\cos(\Delta\varphi + \delta)] \rangle, \quad (4)$$

where, in the absence of a depolarizer

$$\begin{aligned} m_0 = & \text{Tr}(R_3GR_1\rho_0\tilde{R}_1\tilde{G}\tilde{R}_3\sigma_0) + \text{Tr}(R_3GR_2\rho_0\tilde{R}_2\tilde{G}\tilde{R}_3\sigma_0) \\ & + \text{Tr}(R_4GR_1\rho_0\tilde{R}_1\tilde{G}\tilde{R}_3\sigma_0) \\ & + \text{Tr}(R_4GR_2\rho_0\tilde{R}_2\tilde{G}\tilde{R}_4\sigma_0), \end{aligned} \quad (5)$$

$$m_1 = \text{Tr}(R_4GR_1\rho_0\tilde{R}_2\tilde{G}\tilde{R}_3\sigma_0), \quad \sigma = \arg(m_1).$$

Here the angle brackets denote integration over ω with the weight $\Phi(\omega)$, $\Delta\varphi$ and R_i ($i = 1-4$) are the resultant phase difference and the Jones matrices of the readout and sensing interferometer channels, G is the Jones matrix of the single-mode fiber link, $\rho_0 = \rho(\omega_0)$ and $\sigma_0 = \sigma(\omega_0)$ are the excitation and observation matrices, respectively; for simplicity the explicit dependence of the quantities in formula (5) on ω is not given. The quantity $q = 2|m_1|/m_0$ is the visibility of the interference pattern formed by the spectral component of the radiation at the frequency ω , and $\delta = \arg(m_1)$ is the spurious phase shift caused by the nonideality of the polarization characteristics of the interferometer channels and the single-mode fiber link that connects them. The values of q and δ fluctuate with changes in the ambient conditions (primarily because of variation in the polarization characteristics of the single-mode fiber links), which gives rise to zero drift and fading of the output signal from the white-light interferometer.⁴ Even when a completely unpolarized radiation source and an ideal photodetector are used, where ρ_0 and σ_0 are proportional to the unit matrix E , the spurious phase shift does not generally vanish.

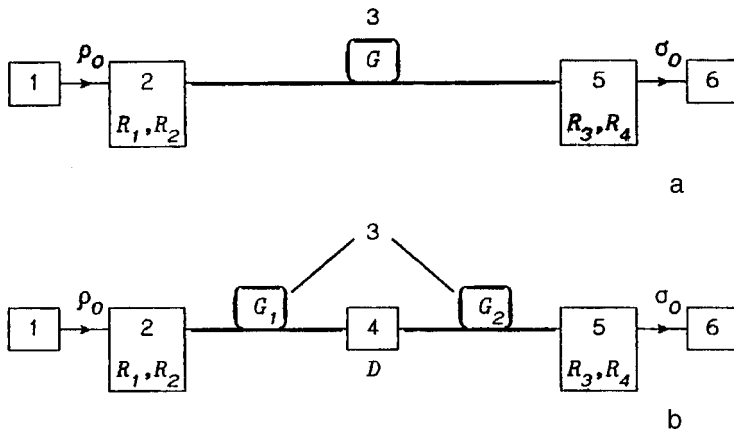


FIG. 1. Diagram of conventional white-light interferometer (a) and white-light interferometer with Billings depolarizer (b).

4. When a Billings depolarizer 4 is incorporated at a midpoint in the single-mode fiber link (see Fig. 1b), expression (4) will contain the time-averaged values \bar{m}_0 , \bar{m}_1 , and $\bar{\delta}$.

Using Eq. (3), we find

$$\begin{aligned} \bar{m}_1 &= \text{Tr}[R_4 G_2 D(t) G_1 R_1 \rho_0 \tilde{R}_2 \tilde{G}_1 \tilde{D}(t) \tilde{G}_2 \tilde{R}_3 \sigma_0] \\ &= \frac{1}{2} \text{Tr}(G_1 R_1 \rho_0 \tilde{R}_2 \tilde{G}_1) \cdot \text{Tr}(R_4 G_2 \tilde{G}_2 \tilde{R}_3 \sigma_0), \end{aligned} \quad (6)$$

where G_1 and G_2 are the Jones matrices of the sections of the single-mode fiber link before and after the depolarizer. If these sections of the link are nondichroic, i.e., if the matrices G_1 and G_2 are unitary, $\tilde{G}_1 G_1 = G_2 \tilde{G}_2 = E$, then

$$\bar{m}_1 = \text{Tr}(R_1 \rho_0 \tilde{R}_2) \cdot \text{Tr}(R_4 \tilde{R}_3 \sigma_0). \quad (7)$$

In exactly the same way, it can be shown that the value of \bar{m}_0 does not depend on the polarization characteristics of the single-mode fiber links, from which it follows that because of the depolarizer, slow variations in the polarization characteristics of the single-mode fiber link (slow compared with the characteristic times of variation of the relative phase delays in the depolarizer) are effectively averaged out and do not influence the precision of the white-light interferometer.

5. To conclude, it has been shown that a bulk or all-fiber Billings depolarizer can be used to improve the precision of white-light interferometers by eliminating the zero drift and fading of the output signal caused by variations in the polarization characteristics of the single-mode fiber linking the sensing and readout interferometers.

The authors would like to thank V. P. Gubin and N. I. Starostin for their interest in this work and for useful discussions.

The work was supported by the Russian Fund for Fundamental Research, Grant No. 96-02-18434.

¹Th. Bosselmann and R. Ulrich, *Proceedings of the Second Conference on Optical Fiber Sensors* (VDE Verlag, Stuttgart, 1984), p. 361.

²R. Jones, M. Hazell, and R. Welford, *Proc. SPIE* **1314**, 315 (1990).

³T. P. Newson, F. Farahi, J. D. C. Jones, and D. A. Jackson, *Opt. Commun.* **68**, 161 (1988).

⁴R. R. Gauthier, F. Farahi, and N. Dahi, *Opt. Lett.* **19**, 138 (1994).

⁵L. A. Ferreira, J. L. Santos, and F. Farahi, *Opt. Commun.* **114**, 386 (1995).

⁶B. H. Billings, *J. Opt. Soc. Am.* **41**, 966 (1951).

⁷É. I. Alekseev, E. N. Bazarov, and A. M. Kurbatov, *Pis'ma Zh. Tekh. Fiz.* **9**, 885 (1983) [*Sov. Tech. Phys. Lett.* **9**, 381 (1983)].

Translated by R. M. Durham

Onset of spatial instability in parametric four-wave in a medium with a diagonally bipolar response

S. A. Podoshvedov

Chelyabinsk Technical University

(Submitted December 20, 1996)

Pis'ma Zh. Tekh. Fiz. **23**, 61–65 (July 26, 1997)

A method of analyzing equations on the phase plane is used to solve a system of equations describing four-wave mixing in media with diagonally bipolar nonlinearity. It is shown theoretically that for certain parameters of the interacting waves, parametric instabilities may occur. It is established that the conversion of the mixed wave power depends strongly on their initial phase shift. © 1997 American Institute of Physics. [S1063-7850(97)02907-8]

It was shown in Ref. 1 that in media whose nonlinear response has specific properties, the dissipation of optical energy induces changes of different sign in the refractive indices. For instance, in nematic liquid crystals we find: $\partial n_e / \partial T < 0$ and $\partial n_o / \partial T > 0$, where $|\partial n_e / \partial T| / |\partial n_o / \partial T| > 5$. This nonlinearity leads to parametric coupling between the waves with the excitation of static gratings. The Hamiltonian nature of nonlinear parametric four-wave mixing allows this process to be described accurately (without various simplifications) on the phase plane. In an earlier study,² four-wave mixing was considered for the amplification of weak waves in the inexhaustible pump wave approximation. An accurate solution of the problem allows us to identify all the “details” which may arise in four-wave interaction.

Let us assume that two unidirectional elliptically polarized waves are incident almost symmetrically relative to the optic axis on a layer of crystal with the optic axis along n . Each wave generates e - and o -type refracted waves, where two waves propagate at the angle δ and another two waves propagate at the angle δ' relative to each other. Then the truncated equations describing four-wave mixing in media with diagonally bipolar nonlinearity have the following form:²

$$\frac{dE_1}{dz} = -\frac{i\pi C_e}{\lambda n_e \cos^2 \theta} ((\Theta_0 + A_e b_e \cos^2 \theta' |E_3|^2) E_1 \cos \theta + A_0 b_0 \cos \theta' E_2 E_3 E_4^* \exp(i\Delta k_z z)),$$

$$\frac{dE_2}{dz} = \frac{i\pi C_0}{\lambda n_0 \cos(\theta + \delta)} ((\Theta_0 + A_0 b_0 |E_4|^4) E_2 + A_e b_e \cos \theta \cos \theta' E_1 E_3^* E_4 \exp(-i\Delta \mathbf{k}_z z)),$$

$$\frac{dE_3}{dz} = -\frac{i\pi C_e}{\lambda n_e \cos^2 \theta'} ((\Theta_0 + A_e b_e \cos^2 \theta |E_1|^2) E_3 \cos \theta' + A_0 b_0 \cos \theta E_1 E_2^* E_4 \exp(-i\Delta \mathbf{k}_z z)),$$

$$\frac{dE_4}{dz} = \frac{i\pi C_0}{\lambda n_0 \cos(\theta' + \delta')} ((\Theta_0 + A_0 b_0 |E_2|^2) E_4 + A_e b_e \cos \theta \cos \theta' E_1^* E_2 E_3 \exp(i\Delta k_z z)), \quad (1)$$

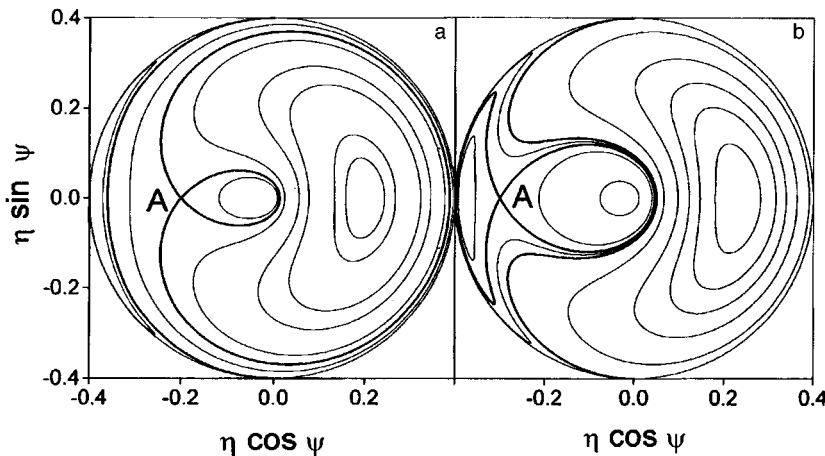


FIG. 1. Phase portraits: a — for $k=0$, b — for $k=0.4$.

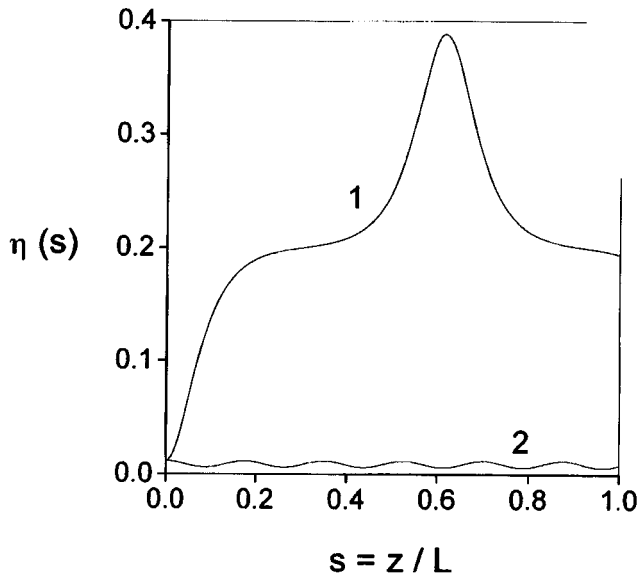


FIG. 2. Influence of the relative initial phase on the energy exchange between light waves.

where $\theta_0 = A_0(|E_2|^2 + |E_4|^2) + A_e(|E_1|^2 \cos^2 \theta + |E_3|^2 \cos^2 \theta')$, $C_e = -|C_e|$, and $C_0 = |C_0|$ are real coefficients ($C_e C_0 < 0$ is the bipolarity condition); when the medium is heated the difference between the coefficients A_0 and A_e is determined by the dichroism of the absorption of light. The quantities n_0 and n_e are the refractive indices of the ordinary and extraordinary waves, λ is the wavelength of the waves participating in the interaction, b_0 and b_e determine the efficiency of the recording of static gratings by the ordinary and extraordinary waves, the angles θ and θ' are the angles of convergence of the waves, and $\Delta \mathbf{k}_z = (\mathbf{k}_2 + \mathbf{k}_3 - \mathbf{k}_1 - \mathbf{k}_4)_z$ is the projection of the wave mismatch on the direction of propagation (z axis). The coefficients A_0 , A_e , b_0 , and b_e are positive real quantities.

The system (1) has the following conserved quantities (integrals of motion): $a|E_1|^2 + |E_2|^2 + b|E_3|^2 + c|E_4|^2 = P$, $a|E_1|^2 - |E_2|^2 = D_1$, and $b|E_3|^2 - c|E_4|^2 = D_2$, where $a = (A_e b_e C_0 n_e \cos^3 \theta') / (A_0 b_0 C_e n_0 \cos(\theta + \delta))$, $b = (A_e b_e C_0 n_e \cos^3 \theta') / A_0 b_0 C_e n_0 \cos(\theta + \delta)$, and $c = \cos \times (\theta' + \delta') / \cos(\theta + \delta)$. By changing to the new variables: $E_1 = q_1 \sqrt{P/a}$, $E_2 = q_2 \sqrt{P}$, $E_3 = q_3 \sqrt{P/b}$, and $E_4 = q_4 \sqrt{P/c}$, we can write the integrals of motion as $|q_1|^2 + |q_2|^2 + |q_3|^2 + |q_4|^2 = 1$, $|q_1|^2 - |q_2|^2 = d_1$, and $|q_3|^2 - |q_4|^2 = d_2$, where $d_1 = D_1/P$ and $d_2 = D_2/P$.

This change of variables allows the initial system (1) to

be reduced to two differential equations for $\eta(s) = |q_2|^2$ and $\psi = ks + \varphi_2 + \varphi_3 - \varphi_1 - \varphi_4(\varphi_i)$ (here φ_i ($i = 1-4$) are the phases of the corresponding light waves: $d\eta/ds = -\partial H/\partial \psi$ and $d\psi/ds = \partial H/\partial \eta$ with the Hamiltonian H :

$$H = \sqrt{\eta(d_1 + \eta)(1 - d_1 + d_2 - 2\eta)(1 - d_1 - d_2 - 2\eta)} \times \cos \psi - \frac{\eta^2}{2}(r_{23} + r_{13} + r_{43} + r_{33}) + \eta \left(r_{23} \frac{1 - d_1 - d_2}{2} + r_{13} \frac{1 - d_1 + d_2}{2} - r_{33} d_1 + k \right), \quad (2)$$

where $s = zp$, $k = \Delta \mathbf{k}_z / \rho$, $\rho = (\pi C_e A_0 b_0 P / \lambda n_e) \times \sqrt{\cos(\theta + \delta) \cos \theta / (\cos(\theta' + \delta') \cos \theta')}$, and the coefficients r_{ij} depend only on the parameters of the medium and the experimental geometry. For simplicity it was assumed in Eq. (2) that $\cos \theta = \cos \theta'$ and $\cos(\theta + \delta) = \cos(\theta' + \delta')$ to obtain the coefficients r_{ij} . The coefficients r_{ij} have the following form: $r_{23} = r_{43} = 1/r_{13} = 1/r_{33} = C_0 n_e \cos \theta / (C_e n_0 \cos(\theta + \delta))$. All other q_i are expressed in terms of η as $|q_1|^2 = \eta + d_1$, $|q_3|^2 = (1 - d_1 + d_2 - 2\eta)/2$, and $|q_4|^2 = (1 - d_1 - d_2 - 2\eta)/2$.

It can be shown that the energy exchange between the waves described by Eq. (1) depends strongly on two bifurcation parameters: $r = r_{23} + r_{43} + r_{13} + r_{33}$ and k . For the values considered here $d_1 = d_2 = 0.1$ we find $r_{er} = 4.33$. For example, for $r_{23} = 0.25$ we find $r = 8.5 > r_{cr}$, which gives rise to a parametrically unstable Hamiltonian natural mode^{3,4} for various values of the dimensionless parameter k . Figures 1a and 1b show phase portraits ($H = \text{const}$) for $k = 0$ and $k = 0.4$, respectively. The unstable mode indicated by the letter A in Fig. 1 generates a two-loop separatrix (all the separatrices are indicated by the thicker lines). It is worth noting the difference between the form of the two-loop separatrices for different k . As a consequence of the asymmetry of the phase portraits relative to the vertical axis, the power conversion between the waves depends strongly on the initial relative phase of the waves. Figure 2 shows how an initial weak wave $\eta = |E_2|^2/P$ evolves with the distance z/L (L is the length of the medium). Curve 1 was obtained for $\psi_0 = \psi(z=0) = 0$ and curve 2 was obtained for $\psi_0 = \pi$ (here $k = 0$).

¹B. Ya. Zel'dovich and N. V. Tabiryan, Usp. Fiz. Nauk **147**, 633 (1985) [Sov. Phys. Usp. **28**, 1059 (1985)].

²T. V. Galstyan, B. Ya. Zel'dovich, Yam Chun Khoo, and N. V. Tabiryan, Zh. Eksp. Teor. Fiz. **100**, 737 (1991) [Sov. Phys. JETP **73**, 409 (1991)].

³S. Trillo and S. Wabnitz, Opt. Lett. **17**, 1572 (1992).

⁴G. Gregori and S. Wabnitz, Phys. Rev. Lett. **56**, 600 (1986).

Translated by R. M. Durham

Excitation of a potentially self-oscillating state in an oscillator with delay and inertia exposed to the simultaneous action of regular and chaotic signals

É. V. Kal'yanov

Institute of Radio Engineering and Electronics, Russian Academy of Sciences, Fryazino
(Submitted March 24, 1997)

Pis'ma Zh. Tekh. Fiz. **23**, 66–71 (July 26, 1997)

An analysis is made of the possibility of inducing a potentially self-oscillating state in a bistable self-oscillating system exposed simultaneously to regular and chaotic signals, as applied to the covert transfer of information in a binary computational system. A system of nonlinear differential difference equations is derived, which describe the behavior of an oscillator with delay and inertia under the action of complex oscillations in a given time interval. It is shown numerically that even when a potentially self-oscillating state is not excited by an external regular signal, stochastic oscillations, as well as providing a masking effect, may function as an additional stimulus to transfer the system to the basin of attraction of a potentially self-oscillating attractor. © 1997 American Institute of Physics. [S1063-7850(97)03007-3]

Various methods of transmitting a signal masked by chaotic oscillations have recently been extensively studied.^{1–6} Since bistable microwave oscillators can be used to transfer information in a binary computational system,⁷ it is profitable to study the possibility of inducing transitions in these oscillators from one stable state to another by a weak regular signal in the presence of masking noise.

Microwave oscillators typically exhibit delay and inertia. Here results are presented of a numerical analysis of the action of a regular external signal on a self-oscillating system with inertia and delay, located in a noisy medium. For the numerical analysis, the following equations are used

$$\frac{d^2x_i}{dt^2} + \frac{\omega_i}{Q_i} \frac{dx_i}{dt} + \omega_i^2 x_i = \omega_i^2 \left(\frac{1}{\sigma_i} \frac{d}{dt} F_i(y_i) + K_j f(t) \right),$$

$$\delta_i \frac{dy_i}{dt} + y_i = x_i(t - \tau_i), \quad (1)$$

$$f(t) = D(1 + \tanh(t - t_0))(1 - \tanh(t - (t_0 + T_0)))\varphi(t),$$

$$\varphi(t) = Cx_2(t) + A_c \cos(\omega_c t),$$

where $i, j = 1, 2$ for $i \neq j$, $k_i = 0$, and $k_2 = 1$.

The system of nonlinear differential difference equations (1) describes the first ($i=1$) oscillator which is exposed to the oscillations of a second ($i=2$) oscillator together with an external harmonic signal, in a given time interval T_0 . Each oscillator consists of a nonlinear amplifier, first- and second-order filters, a delay line, and a differentiating element, all in a closed loop. The notation is as follows: x_i and y_i are variables which depend on the time t and characterize the oscillation processes in the oscillators, ω_i and Q_i are the frequencies and Q factors of the second-order filters, δ_i and τ_i are the time constants of the first-order filters and the differentiating elements, respectively, $F_i(y_i)$ are the characteristics of the nonlinear amplifiers, τ_i are the time delays of the signals, A_c and ω_c are the amplitude and frequency of the external harmonic signal, C is a coefficient determining the level of

action of the oscillations of the second oscillator, D is a constant coefficient, and t_0 is the time of initiation of the action.

The calculations were made by a fourth-order Runge–Kutta method with an integration time step of 0.05, where the characteristics of the nonlinear amplifiers were approximated by

$$F_i(y_i) = B_i \sigma_i \exp(-y_i^{n_i}), \quad (2)$$

where B_i and n_i are the gain parameter and the degree of nonlinearity.

The parameters in Eqs. (1) and (2) are selected so that the first oscillator is bistable and the second is chaotic. The values of these parameters are: $\omega_1 = \omega_2 = 1$, $Q_1 = Q_2 = 2$, $\delta_1 = \delta_2 = 0.1$, $\tau_1 = 9.25$, $\tau_2 = 9.5$, $B_1 = 1.6$, $B_2 = 4$, $n_1 = 2$, and $n_2 = 6$.

For the selected parameters of this oscillator, oscillations are excited autonomously in the basin of attraction of the high-frequency attractor (attractor H) at the frequency $\omega_H = 1.26$, and at $\omega_L = 0.76$ (low-frequency attractor L) they are potentially self-oscillating. The action of the external signal can be used to control the excitation of oscillations. This control is achieved by inducing a transition of the oscillations from the basin of attraction of the attractor H to that of the attractor L and back. It has been established that such a transition may take place when higher-intensity chaotic oscillations act in addition to the regular signal, even when the regular oscillations alone do not excite a potentially self-oscillating state. This is illustrated by the realizations in Figs. 1 and 2.

Figure 1 shows realizations illustrating the behavior of the oscillatory process $x_1(t)$ under the action of an external signal $f(t)$ when this signal either comprises only regular oscillations (Fig. 1a) or only chaotic oscillations (Fig. 1b), or the sum of regular and chaotic oscillations (Fig. 1c). The realizations of the corresponding actuating oscillations are given in Figs. 2a–2c. The parameters determining the actuating oscillations have the values $A_c = 0.2$, $\omega_c = 0.76$, $C = 0$ for the case in Figs. 1a and 2a, $A_c = 0$, $C = 0.8$ for the case in

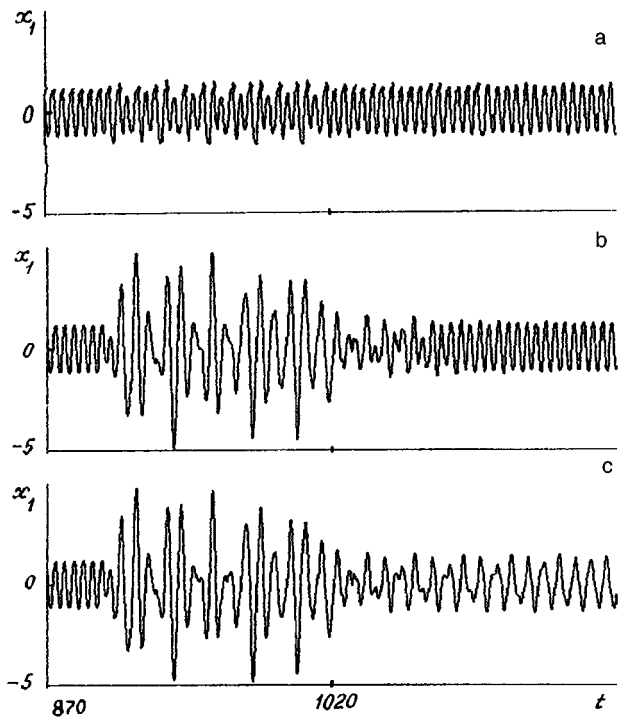


FIG. 1. Realizations of oscillations of the oscillator exposed to only a regular signal (a), only chaotic oscillations (b), and both regular and chaotic signals (c).

Figs. 1b and 2b, and $A_c=0.2$, $\omega_c=0.76$, $C=0.8$ for the case in Figs. 1c and 2c. In all three cases, $D=0.25$, $T_0=120$, and $t_0=900$.

In the time interval $t \in (870;900)$ (before the action) regular autonomous oscillations $x_1(t)$ take place at the frequency $\omega_h=1.26$ with a simple limit cycle in the basin of attraction of the attractor H . Under the external action (in the time interval $t \in (900;1020)$) a transient process takes place, which continues after the action has ended. As a result, in the case in Figs. 1a and 1b the oscillations $x_1(t)$ remain in the basin of attraction H whereas in Fig. 1c, they enter the basin of attraction of the attractor L . In this last case the frequency of the oscillating process $x_1(t)$ tends to $\omega_l=0.76$ after the end of the action and, since $\omega_l=\omega_c$, this may be considered to be a process where the system “remembers” the frequency of the regular component of the actuating oscillations.

The oscillations $x_2(t)$ in the time interval $t \in (900;1020)$ fairly accurately play the role of an oscillating process masking the regular signal in this time interval. It can be seen from a comparison of the realizations in Fig. 2 that the amplitude of the regular oscillations (Fig. 2a) is an order of magnitude lower than the maximum deviations of the chaotic oscillating process $x_2(t)$ (Fig. 2b). Thus, the realization of the sum oscillations has the form of a stochastic signal (see Fig. 2c) and differs negligibly from the realization in Fig. 2b.

As well as functioning as a masking signal, the chaotic oscillations in Fig. 1c also act as a source of additional stimulus since, without them, the system does not undergo a transition to the basin of attraction of the attractor L . When

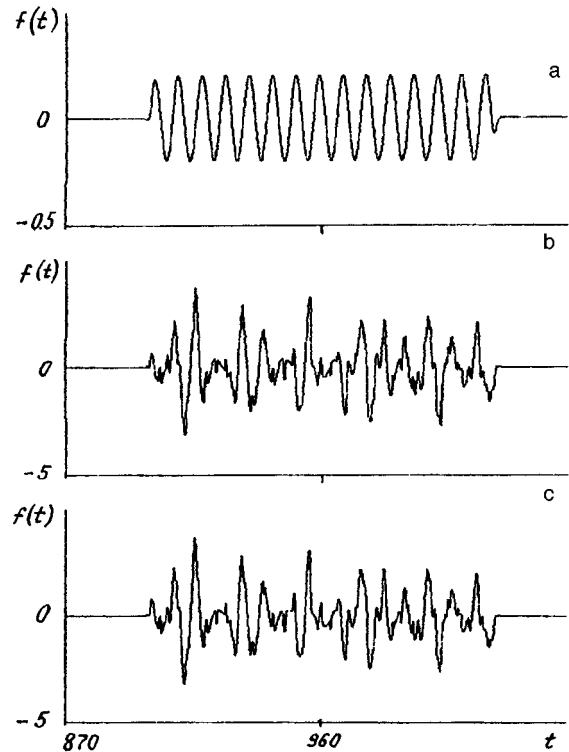


FIG. 2. Realizations of actuating oscillations: a — regular oscillations, b — chaotic oscillations, c — sum oscillations of regular and chaotic signals.

the amplitude of the regular signal oscillations is fairly large (for instance, when $A_c=0.4$), the system can also undergo a transition to the basin of attraction of the attractor L when $C=0$. However, the masking role of the stochastic oscillations is retained.

To conclude, the results of these calculations indicate that in principle, covert transfer of information may be achieved when a potentially self-oscillating state is induced by the simultaneous action of regular and chaotic signals. It should be noted that this effect may depend on the duration of the action. This aspect has not been studied and is interesting in itself. The influence of the duration of action on a bistable self-oscillating system was only considered in Ref. 8 for the case of regular actuation and it was shown that the behavior of the system depends nontrivially on the duration of the external radio pulse used.

- ¹L. J. Kocarev, K. S. Halle, K. Eckert, and L. O. Chua, *Int. J. Bifurcat. Chaos* **2**, 709 (1992).
- ²A. R. Volkovskii and N. F. Rul'kov, *Pis'ma Zh. Tekh. Fiz.* **19**(3), 71 (1993) [*Tech. Phys. Lett.* **19**, 97 (1993)].
- ³Yu. L. Bel'skiĭ and A. S. Dmitriev, *Radiotekh. Élektron.* **38**, 1310 (1993).
- ⁴B. Ya. Kislov, *Radiotekh. Élektron.* **38**, 1793 (1993).
- ⁵A. K. Kozlov and V. D. Shalfeev, *Pis'ma Zh. Tekh. Fiz.* **19**(23), 83 (1993) [*Tech. Phys. Lett.* **19**, 769 (1993)].
- ⁶A. K. Kozlov, *Pis'ma Zh. Tekh. Fiz.* **20**(17), 65 (1994) [*Tech. Phys. Lett.* **20**, 710 (1994)].
- ⁷M. B. Golant, Yu. V. Gulyaev, A. V. Gritsenko *et al.*, *Radiotekh. Élektron.* **36**, 501 (1991).
- ⁸É. V. Kal'yanov and S. O. Starkov, *Pis'ma Zh. Tekh. Fiz.* **18**(23), 49 (1992) [*Tech. Phys. Lett.* **18**, 782 (1992)].

Translated by R. M. Durham

Pair production in counterpropagating electron and laser beams

P. A. Golovinskiĭ

(Submitted December 18, 1996)

Pis'ma Zh. Tekh. Fiz. **23**, 72–75 (July 26, 1997)

An analysis is made of the collision between a high-energy electron beam and laser radiation. It is shown that when the electron energy is 800 GeV and the laser pulse has an intensity of 10^{20} W/cm², a wavelength of 248 nm, and a duration of 300 fs, a single seed electron produces 60 electrons and positrons. © 1997 American Institute of Physics. [S1063-7850(97)03107-8]

It has been shown¹⁻⁴ that the interaction between laser radiation and electrons may be accompanied by the production of electron-positron pairs by collisions with atomic nuclei in field intensities of $\sim 10^{21}$ – 10^{22} W/cm².

However, the direct action of laser radiation is insufficient to produce electron-positron pairs. This process requires an intensity of at least 10^{28} W/cm² at which the work of the field at the Compton wavelength corresponds to the production energy for an electron-positron pair, which is hardly likely to be achieved in the foreseeable future. However, the requirements imposed on the laser radiation intensity can be reduced by using electron and laser beams. A possible system involves using a counterpropagating beam geometry,⁵ which is highly typical of electron and proton accelerators. The laser radiation in the system of the particle becomes hard, as a result of the Doppler effect.

It is known that the cross section σ is invariant under Lorentz transformations. The cross section for pair production as a result of a photon–electron collision in a reference frame where the electron is initially at rest, is given by⁶

$$\sigma = \sigma_0 \left(\ln \frac{\omega}{m} - 3.47 \right), \quad (1)$$

where $\sigma_0 = \frac{28}{9} \alpha r_e^2$, where r_e is the classical electron radius, ω is the frequency of a laser photon in the reference frame of the laser.

Converting to the laboratory reference frame, for ultrarelativistic electrons of energy E we obtain

$$\sigma = \sigma_0 \left(\ln \frac{2\omega_0 E}{m^2} - 3.47 \right), \quad (2)$$

where ω_0 is the laser radiation frequency in the laboratory reference frame. The typical initial electron energy required for efficient implementation of the process is $E_0 = 20m^2/\omega_0 = 800$ GeV at a laser wavelength $\lambda = 248$ nm. This electron momentum in the laboratory reference frame is much greater than the laser photon momentum. This implies that secondary particles will be emitted in the direction of the initial electron with reduced energy after each collision with photons.

Following the theory of showers,⁷ we consider a model in which an electron-positron pair is produced as a result of a collision between a γ ray and an electron, and the energy is redistributed such that $\beta = 1/3$ of the initial particle energy is assigned to each particle. These particles then collide with the laser radiation photon flux to produce new pairs, and so

on. The production of particles in the energy layer with the energy $E_k = \beta^k E$ is indicated by the subscript k . Then for the $k+1$ layer we can write the rate equation

$$\frac{dN_{k+1}}{dt} = -W_{k+1}N_{k+1} + W_k N_k / \beta, \quad (3)$$

where N_k is the total number of particles in the k th energy layer and W_k is the probability of the production of an electron-positron pair. We use the explicit form for $W_k = F\sigma = a - bk$, where $a = \sigma_0(F \ln(2\omega_0 E/m^2) - 3.47)$, and $b = \sigma_0 F \ln \beta^{-1}$.

Having expressed the difference in Eq. (3) in terms of the derivative, we obtain a partial differential equation after replacing the discrete index k by the continuous parameter x :

$$\frac{\partial N}{\partial t} = -\frac{\partial}{\partial x} (W(x)N) + 2W(x)N. \quad (4)$$

After casting the variables in the form $n(x,t) = W(x)N(x,t)$, we then have

$$\frac{1}{W(x)} \frac{\partial n}{\partial t} = -\frac{\partial n}{\partial x} + 2n. \quad (5)$$

To solve Eq. (5), we need to know the initial distribution, which we take to be monoenergetic and describe it using a δ -function in the form

$$N(x,0) = \delta(x) = \lim_{\gamma \rightarrow \infty} g(x, \gamma), \quad (6)$$

where $g(x, \gamma) = 1/\gamma\sqrt{\pi} \exp(-x^2/\gamma^2)$ is the initial distribution normalized to a single electron.

A solution of the quasilinear equation (5) with the initial condition $n(x,0) = g(x, \gamma)W(x)$ may be found by the method of characteristics,⁸ and is given by

$$N_\gamma(x,t) = \frac{1}{\gamma\sqrt{\pi}} e^{2x+bt} \exp\left(-f(x,t) \left(2 + \frac{f(x,t)}{\gamma^2}\right)\right), \quad (7)$$

where $f(x,t) = (a - (a - bx)e^{bt})/b$.

The total number of particles formed by time t for a single seed electron is

$$\bar{N}(t) = \lim_{\gamma \rightarrow \infty} \int_0^\infty N_\gamma(x,t) dx. \quad (8)$$

The definite integral in formula (8) is calculated analytically, and after going to the limit, we obtain

$$\tilde{N}(t) = \exp\left(\frac{2a}{b}(1 - e^{-bt})\right). \quad (9)$$

We estimate the number of particles formed at the energy E_0 per electron. We take the parameters of the focused laser radiation as those for a high-power excimer laser:⁹ intensity at the focal spot $I = 10^{20}$ W/cm² and laser pulse length $\tau = 300$ fs. Then the total photon flux density during the pulse τ is $F\tau = I\tau/\omega_0 = 3 \times 10^{27}$ cm⁻². Under these conditions we find $b\tau \gg 1$ and $\tilde{N} \approx 60$ particles are generated per seed electron. Thus, this effect has all the characteristic features of breakdown of the vacuum.

Studies of the interaction between high-energy electron beams and focused laser radiation are currently being undertaken at the Stanford Linear Accelerator Center (SLAC).¹⁰ During tests on the system, nonlinear Compton scattering was observed with a beam electron energy of 46.6 GeV and a focused laser radiation intensity of 10^{18} W/cm² at wavelengths of 1054 and 527 nm. Further refinement of the system also envisages experiments to observe the production of electron-positron pairs. This may involve an experiment using the counterpropagating beam configuration considered here to study breakdown of the vacuum.

This work was partially financed by the Soros International Science Foundation (Grant No. 95-D616).

¹F. V. Bunkin and A. E. Kazakov, Dokl. Akad. Nauk SSSR **193**, 1274 (1970) [Sov. Phys. Dokl. **5**, 758 (1970)].

²K. Boyer, T. S. Luk, and C. K. Rhodes, Phys. Rev. Lett. **60**, 557 (1988).

³P. A. Golovinskiĭ, Pis'ma Zh. Éksp. Teor. Fiz. **51**, 355 (1990) [JETP Lett. **51**, 403 (1990)].

⁴P. A. Golovinski, J. Nonlin. Opt. Phys. Mat. **5**, 139 (1996).

⁵P. A. Golovinski, in *Proceedings of the Seventh International Conference on Multiphoton Processes*, Garmisch-Partenkirchen, Germany, 1966, Paper B25.

⁶A. I. Akhiezer and V. B. Berestetskii, *Quantum Electrodynamics* (Wiley, New York, 1965) [Russ. original, 3rd ed., Nauka, Moscow, 1969].

⁷A. I. Akhiezer and N. F. Shul'ga, *High-Energy Electrodynamics in Matter* [in Russian] (Nauka, Moscow, 1993).

⁸V. I. Smirnov, *A Course of Higher Mathematics*, Vol. 4 (Addison-Wesley, Reading, Mass., 1964) [Russ. original, GITTL, Moscow, 1957].

⁹B. Bouma, T. S. Luk, K. Boyer, and C. K. Rhodes, J. Opt. Soc. Am. B **10**, 1180 (1993).

¹⁰C. Bula, K. T. McDonald, E. J. Prebys *et al.*, Phys. Rev. Lett. **76**, 3116 (1996).

Translated by R. M. Durham

Enhancement of the precision of fiber-optic interferometers by using couplers with high spectral power or antisymmetric supermode cutoff

É. I. Alekseev and E. N. Bazarov

Institute of Radio Engineering and Electronics, Russian Academy of Sciences, Moscow

(Submitted January 20, 1997)

Pis'ma Zh. Tekh. Fiz. **23**, 76–80 (July 26, 1997)

It is shown that in 2×2 single-mode optical-fiber directional couplers operating with cutoff of the antisymmetric normal mode of a composite waveguide, the additional stray phase shift of the waves in the forward and cross channels (found in normal couplers) vanishes. Thus, by using these couplers (instead of the usual ones) in various interferometers, the precision can be enhanced substantially. It has also been shown that the precision of interferometers with wide-band radiation sources (such as white-light interferometers and fiber-optic gyroscopes) can be improved by replacing the usual couplers with couplers of high spectral power whose splitting ratio can execute a large number of oscillations within the radiation line width, efficiently eliminating the afore-mentioned stray phase shift. © 1997 American Institute of Physics. [S1063-7850(97)03207-2]

1. The precision of single-mode fiber interferometers is determined to a considerable extent by the characteristics of the directional couplers. Conventional 2×2 directional couplers with the phase parameter $N \approx 0.25$ are currently used in single-mode fiber-optic interferometers. We recall that N is the number of oscillations of the splitting ratio in directional couplers, $N = \Delta\varphi / (2\pi)$, where $\Delta\varphi$ is the difference between the phases φ_1 and φ_2 of the symmetric and antisymmetric normal modes (supermodes) of a composite waveguide.¹ As a result of the difference between the losses α_1 and α_2 of the supermodes in real directional couplers, the relative phase shift of the signals in the forward and cross channels (γ) differs from the value $\pi/2$ obtained in an ideal directional coupler.² Consequently, a stray phase shift δ of the interfering waves is established in the directional coupler, and its variations lead to a “zero” drift of the single-mode fiber interferometer and therefore reduce its precision. We show that this shortcoming of single-mode fiber interferometers can be eliminated by using directional couplers with antisymmetric supermode cutoff or with a fairly high spectral power $R = \eta N$ (η is a coefficient between 2 and 5 for fused directional couplers¹).

2. The transmission matrix of 2×2 directional couplers at the frequency ω , expressed in terms of the transmission coefficients of the symmetric $V_1 = \exp(-\alpha_1 + i\varphi_1)$ and antisymmetric $V_2 = \exp(-\alpha_2 + i\varphi_2)$ supermodes, is given by

$$T = \| \| t_{ij} \| \| = \begin{vmatrix} V_1 + V_2 & V_1 - V_2 \\ V_1 - V_2 & V_1 + V_2 \end{vmatrix}, \quad i, j = 1, 2. \quad (1)$$

Using Eq. (1), we find (see also Ref. 2):

$$\gamma = \arctan \{ 2 \sin(\Delta\varphi) \exp[-(\alpha_1 + \alpha_2)] \times [\exp(-2\alpha_1) - \exp(-2\alpha_2)]^{-1} \} = \arctan m. \quad (2)$$

As a result of the cutoff of the antisymmetric supermode we obtain $\alpha_2 \rightarrow \infty$ so that $\gamma \rightarrow 0$ and therefore for the stray phase shift we find $\delta \rightarrow 0$. It can therefore be expected that the use of directional couplers with antisymmetric supermode cutoff will improve the precision characteristics of single-mode fiber

interferometers. Let us discuss this aspect in greater detail for the case of a fiber ring interferometer (see Fig. 1), assuming that the radiation source is monochromatic.

Using Eq. (1), the signals at the symmetric (E_1) and asymmetric (E_2) outputs of a fiber ring interferometer are given by:

$$E_1 = 2E_0 \exp[-(\alpha + i\beta L)] t_{12} t_{22} \cos \theta, \quad (3)$$

$$E_2 = E_0 \exp[-(\alpha + i\beta L)] \times [\exp(i\theta) t_{12} t_{21} + \exp(-i\theta) t_{11} t_{22}].$$

Here α are the losses in a circuit of length L , β is the propagation constant, and θ is the nonreciprocal phase shift of the counterpropagating waves. As was to be expected, when the symmetric output of the fiber ring interferometer is used, no stray phase shift is observed, whereas for the asymmetric output, such a shift is observed and is determined by the argument of the complex quantity $t_{11}^* t_{22}^* t_{12} t_{21}$. The calculations yield $\delta = 2\gamma$. For the estimates we can set $|\sin(\Delta\varphi)| = 1$ and then, assuming that $\exp(-\alpha_2)$ is small, we find $\delta \approx 4 \exp(\alpha_1 - \alpha_2)$, and for $\alpha_2 \rightarrow \infty$, we have $\delta \rightarrow 0$, which supports the assumption made above.

At present, no detailed experimental data are available on the operation of couplers with antisymmetric supermode cutoff. Nevertheless, there is reason to suppose that these couplers, having a broad range of properties, will be suitable for use in fiber ring interferometers and other types of single-mode fiber interferometers. For instance, it was shown in Ref. 3 that these couplers may be compact (comparable in size to the “usual” directional couplers) and may have a splitting ratio almost independent of wavelength and bends. They have the disadvantage of relatively high losses (≥ 3 dB) but in many cases, this can be tolerated because of the enhanced precision of the measurements.

3. When fabricating fused couplers, the splitting ratio oscillates very rapidly with increasing length of the neck-down, particularly close to antisymmetric supermode cutoff.^{1,3} Similar rapid oscillations are observed in the wave-

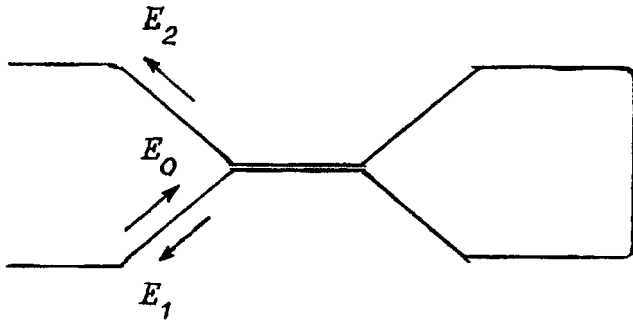


FIG. 1. Diagram of fiber ring interferometer.

length dependence of the splitting ratio. The spectral period of these oscillations may be made so small that a large number of these will fall within the line width of the radiation source of a single-mode fiber interferometer. This operating regime of the directional coupler (superstrong coupling or extremely long interaction lengths) is also of interest for a single-mode fiber interferometer since in this case, the stray phase shift introduced by the directional coupler is averaged and the resultant stray phase pedestal may be significantly reduced. By way of example, we again consider a fiber ring interferometer (see Fig. 1).

When a wide-band radiation source having the intensity I_0 and the line profile $\Phi(\omega)$ normalized to unity, is used in fiber ring interferometers, the photodetector current at the asymmetric output is given by

$$i = I_0 \langle |t_{11}t_{22}|^2 + |t_{21}t_{12}|^2 + \exp(i2\theta)t_{12}t_{21}t_{11}^*t_{22}^* + \exp(-i2\theta)t_{12}^*t_{21}^*t_{11}t_{22} \rangle, \quad (4)$$

where the angle brackets denote integration over ω with the weight $\Phi(\omega)$ and the other notation has the same meaning as above.

To a first approximation, it may be assumed that θ and also α_1 and α_2 do not depend on ω . Then, in the superstrong coupling regime but far from antisymmetric mode cutoff, high-quality directional couplers have low normal mode

losses and the loss difference is small. In this case, we find $m \approx K \sin(\Delta\varphi)$, where K is a quantity inversely proportional to the difference between the normal mode losses, and for high-quality couplers $K \gg 1$. With these qualifications in mind and also taking into account the rapid oscillations (4) of the function $\cos(2\Delta\varphi)$, we find that apart from a multiplicative factor:

$$i \approx I_0 \left[1 - \frac{1}{2} \cos(2\theta) \right]. \quad (5)$$

From this it follows that in this particular case, the stray phase shift averages to zero, to a first approximation.

4. It has thus been shown that in many cases in single-mode fiber interferometers, it is expedient to use couplers with antisymmetric supermode cutoff. These couplers have the disadvantage of comparatively high losses, but they have the advantage of improving the precision of a single-mode fiber interferometer (in a fiber ring interferometer, they also simplify the optical system because the asymmetric output can be used). Other possible operating regimes of directional couplers in single-mode fiber interferometers include superstrong coupling and/or ultralong interaction length, where the splitting ratio oscillates rapidly within the line width of the radiation source. The stray phase shift introduced by real directional couplers is then efficiently averaged, although the visibility of the interference pattern deteriorates slightly.

The authors would like to thank V. P. Gubin and N. I. Starostin for their interest in this work and for useful discussions.

This work was supported by the Russian Fund for Fundamental Research, Grant No. 96-02-18434.

¹A. G. Bulushev, Yu. V. Gurov, E. M. Dianov *et al.*, *J. Lightwave Technol.* **LT-6**, 1575 (1988).

²R. C. Youngquist, L. F. Stokes, and H. J. Shaw, *IEEE J. Quantum Electron.* **QE-19**, 1888 (1983).

³F. Bilodeau, K. O. Hill, D. C. Johnson, and S. Faucher, *Opt. Lett.* **12**, 614 (1987).

Translated by R. M. Durham

Equation of state for a weakly ionized gas-discharge plasma

G. I. Mishin

Applied Physics Laboratory, Johns Hopkins University, Laurel, MD 20723-6099

(Submitted May 20, 1997)

Pis'ma Zh. Tekh. Fiz. **23**, 81–88 (July 26, 1997)

A modification is proposed for the van der Waals equation for a real gas, which transforms it into an equation of state for a thermally nonequilibrium weakly ionized gas-discharge plasma. This modification reflects the existence of collective interactions between neutral particles in the gas-discharge plasma, which generates quasistructural formations impeding the compression and expansion of the plasma. This equation completely describes the characteristics of the dynamic processes in the gas-discharge plasma, provides a quantitative explanation of these processes, and reveals the essential physical features of this phenomenon. © 1997 *American Institute of Physics*. [S1063-7850(97)03307-7]

In the late sixties and early seventies it was observed that in weakly ionized gases, the velocity and amplitude of sound are higher than the corresponding calculated gaskinetic values.^{1–3}

The theoretical analyses performed at that time were based on a modification of the volume heat release which takes place as a result of the transfer of the energy of fast electrons to neutral particles through elastic collisions (see, e.g., Refs. 4 and 5).

However, it soon became clear⁶ that this mechanism could not explain the increased speed of sound or its increased intensity.

Different versions of this theoretical concept continued to be analyzed subsequently.⁷

In 1978 it was established that the Mach number of a spherical body in a low-temperature gas-discharge plasma is considerably lower than that in un-ionized gases at the same velocity and temperature.

Results of studying this effect were published in 1991 (Ref. 8). Estimates made using these results indicated that the observed effects may be attributed to the existence of a specific plasma sound velocity W , substantially higher than the corresponding gas-kinetic value. Subsequent investigations of shock waves in ionized gases provided extensive information on this phenomenon.

Without giving details of the results of specific studies, the general conclusions deduced from these may be presented.

1. A low-temperature gas-discharge plasma (degree of ionization 10^{-5} – 10^{-7}) of all the gases studied (air, CO₂, N₂, Ar, Ne, and Xe) exhibits anomalous dynamic properties at pressures of 1–200 torr and temperatures between 100 and 1400 K.

2. Dynamic characteristics are not observed in a thermally ionized plasma.

3. The velocity of sound in a plasma is isotropic and does not depend on the orientation of the electric field or the direction of motion of the body.⁸

4. After shunting the discharge current, the anomalous properties of the plasma do not disappear “instantaneously” but decay relatively slowly with a time constant $\approx 2 \times 10^{-2}$ s

(Ref. 9), which is substantially longer than the electron recombination time.

5. The anomalous properties of the plasma do not occur “immediately” after the onset of the discharge: the average time taken for their establishment is $\approx 3 \times 10^{-4}$ s (Ref. 10).

6. In regions where a gas-discharge plasma exists, the velocity of sound is higher in regions of higher electron temperature T_e and depends only weakly on the electron density n_e (Ref. 11).

7. Ultraviolet irradiation of the plasma tends to increase the velocity of sound.¹²

8. A weak transverse magnetic field (~ 100 Oe) appreciably reduces the velocity of sound.¹³

9. The velocity of sound in a gas-discharge plasma increases in proportion to the gas-kinetic temperature.

10. An increase in the ratio E/P (electric field strength/gas pressure) increases the velocity of sound.

Since the square of the velocity of sound in a weakly ionized gas is determined by the compressibility of the neutral particles at constant entropy s ,

$$W^2 = (\partial P / \partial \rho)_s, \quad (1)$$

it may be assumed that although the neutral particles are far apart in the gas-discharge plasma, a strong interaction exists between them.

Thus the the concept of a plasma as an ideal gas is an extremely attractive vehicle for describing its dynamic properties.

The van der Waals equation¹⁴ is a simple and physically well-justified equation of state for a real gas, which for 1 mole of gas (neglecting the volume correction) has the form

$$\left(P + \frac{a}{V^2} \right) V = RT, \quad (2)$$

where P is the external pressure, V is the molar volume, and a is the pressure correction.

Equation (2) can allow for the existence of forces of attraction between the plasma particles, which increase the pressure in the plasma by the additional internal pressure $P_i = a/V^2 = an^2$, where $a = \alpha N^2$, $N = 6.023 \times 10^{23}$ mole⁻¹ is Avogadro's number, and $n = N/V$ is the particle density.

However, it is easy to show that this equation leads to an absurd situation, since the value of α satisfying the experimentally measured velocity of sound corresponds to a pressure P_i more than 30% of P .

Such a high additional pressure in the plasma could not have gone unnoticed and would immediately have been observed experimentally.

Thus, for the case of a gas-discharge plasma we need to take into account another difference from the usual ideal gas — in the absence of dynamic perturbations, the internal pressure is $P_i=0$ and expression (2) is transformed to give the equation for an ideal gas $PV=RT$.

The equation of state for a weakly ionized gas-discharge plasma should therefore be written as

$$\left(P - \frac{a}{V^2} + \theta \right) V = RT, \quad (3)$$

where $\theta = a/V_0^2 = \alpha n_0^2$, and V_0 and n_0 are the molar volume and the plasma density in the initial state, respectively.

It can be seen that in the plasma “rest” state, Eq. (3) is identical to the equation for an ideal gas.

However, when the plasma is perturbed by an acoustic wave, it becomes “unbalanced” as a result of changes in the density distribution under the action of the external forces, and as a result, the term describing the interparticle interaction, $\theta - \alpha n^2$, becomes nonzero.

Under compression this term is $\theta - \alpha n^2 < 0$ and the forces between the particles are repulsive, whereas under expansion, $\theta - \alpha n^2 > 0$ they are attractive.

In both cases, the particles are exposed to intermolecular forces that tend to return them to the former equilibrium position.

In order to establish the functional relation between the velocity of sound W and the plasma parameters, we use Eqs. (1) and (3) together with the equation of the first law of thermodynamics in differential form.

The derivative $(\partial P / \partial \rho)_s$ is found by assuming that the molar specific heat of the plasma at constant volume, C_V , has the same value as for an ideal gas, since the interparticle distance does not change and the relation $VT C_V / R = \text{const}$ therefore holds.

We also take into account that acoustic waves are weak perturbations (even for a strong acoustic wave the change in pressure is no greater than $\sim 10^{-3}$ of the pressure) and thus the difference is $|\theta - a/V^2| \leq 10^{-3} P$.

After suitable transformations, we obtain the required dependence:

$$\left(\frac{\partial P}{\partial \rho} \right)_s = \frac{C_V + R}{C_V} \cdot \frac{RT}{\mu} + \frac{2a}{V_0 \mu}, \quad (4)$$

where μ is the molecular weight.

Replacing $a = \alpha n^2$ and $V = N/n$, we obtain

$$W^2 = \left(\frac{C_V + R}{C_V} + \frac{2\alpha n_0 N}{RT} \right) \cdot \frac{RT}{\mu}, \quad (5)$$

from which it follows that Poisson’s ratio is

$$\gamma = \gamma_{\text{ug}} + \frac{2\alpha n_0 N}{RT}, \quad (6)$$

where $\gamma_{\text{ug}} = (C_V + R)/C_V$ is the ratio of the specific heats in the un-ionized gas.

Before analyzing Eqs. (5) and (6), let us examine the results of Refs. 8 and 10, taking into account the conclusion drawn from Eq. (7): the ratio of the specific heats in a weakly ionized gas is always higher than that in an un-ionized gas.

In Ref. 8 schlieren photographs of a spherical model passing through ionized air at a pressure of 45 torr and $T = 1350$ K were obtained using a ballistic system. The ratio of specific heats corresponding to this temperature is $\gamma = 1.33$.

These photographs were used to measure the relative standoff of the shock wave head Δ/r (Δ is the standoff and r is the radius of the sphere).

The standoff of the shock wave head is a parameter that depends on the Mach number of the flight and on the ratio γ . The lower the Mach number $M = v/W$ (v is the flight speed) and the higher the ratio γ , the greater is the relative standoff Δ/r for the same flight speed.

The results of the measurements show that the values of the standoff correspond to the Mach numbers determined by the velocity of sound W , which is 1080 m/s.

However, it follows from Eq. (6) that in a plasma, the ratio of the specific heats is greater than that in un-ionized air, and thus the value of W should be lower than 1080 m/s.

Since the dependence $\Delta/r(M, \gamma)$ cannot generally be given by a simple expression, a method of successive approximations must be used to calculate W and γ : an approximate value of W is set and the Mach number is determined using the known flight speed, and then the ratio γ is obtained using Eq. (6).

These values of M and γ are used to calculate Δ/r which is compared to the experimental value measured for a given flight speed.

In particular, the calculations showed that for $V = 1800$ m/s, the measured relative standoff of the shock wave corresponds to $\gamma = 2.1$ and $M = 2$, i.e., $W = 900$ m/s.

Thus, the real velocity of sound in this case is 1.2 times lower and γ is 1.6 times higher than was previously assumed.

Equation (6) is used to find α and to determine the binding energy of 1 mole of plasma particles under the experimental conditions $U_s = 2\alpha n_0 N = 7.2 \times 10^3$ J.

The results of measurements of the velocity of sound in a “cold” plasma (not heated by Joule heat) are now considered.¹⁰ A shock tube was used to determine the velocity of sound. The velocities of acoustic pulses in an air plasma were measured approximately 500 μs after initiating a pulsed gas discharge with $E/P \approx 4$ V/cm·Torr. The plasma pressure was 6 Torr and the gas-kinetic temperature did not exceed 400 K.

The measurements showed that under these conditions, the velocity of sound in the plasma is $W = 688$ m/s, i.e., 1.7 times higher than that in un-ionized air.

Using the measured velocity of sound, the adiabatic exponent $\gamma = 4.1$ is determined according to formula (5) and

then, in accordance with Eq. (6), we find $\alpha = 0.53 \times 10^{-30}$ erg/cm³.

It can be seen that a decrease in the plasma temperature is accompanied by an increase in the adiabatic exponent.

Note that the energy of 1 mole of plasma is then $U_s = 9.6 \times 10^3$ J.

The difference between U_s in the first and second experiments arises because E/P in the second case is twice than in the first.

The introduction of the positive constant $\theta = \alpha n_0^2$ and the negative variable αn^2 in the van der Waals equation implies that the equilibrium state between the particle centers, in which the interaction potential energy is zero, is tens of times greater than that in un-ionized gases.

It was established experimentally in Ref. 9 that the ‘‘lifetime’’ constant of the anomalous properties of a gas-discharge plasma is relatively high, $\approx 2 \times 10^{-2}$ s, and their existence should be attributed to the presence of metastable particles or long-lived complexes in the plasma (observation 4). Metastable particles are formed in the plasma as a result of inelastic collisions between electrons and neutral particles in the gas-discharge process and therefore a certain time must elapse after initiation of the discharge before a sufficient quantity of these particles are formed (observation 5).

If the electron temperature (energy) T_e increases, both the collision frequency and the probability of inelastic collisions increase. Thus an increase in the ratio E/P leads to an increase in the velocity of sound.

In this case, T_e obviously plays a major role and the density is of secondary importance (observations 6 and 10).

In a thermally ionized plasma T_e is approximately ten times lower than its value in a gas discharge and the electron energy is below the excitation potential for metastable states.

Therefore in a thermally ionized plasma no anomalous dynamic properties are observed for any electron densities n_e (observation 2) and even a weak magnetic field, slowing the electrons, significantly reduces the observed anomalous effects (observation 8).

Since these results have shown that the increase in the velocity of sound in a plasma is caused by the interaction of neutral particles controlled by gasdynamic laws, the properties of the plasma should be isotropic, except of course for the electrode zones (observation 3).

In experiments in which plasma particles were activated by absorbing ultraviolet radiation, the probability of formation of metastable particles was increased, as was the velocity of sound (observation 7).

It follows from the proposed concept of a gas-discharge plasma that despite the existence of structure in the plasma, the propagation of acoustic waves remains an adiabatic and isentropic process which is not accompanied by any dissipation of energy, although some dispersion of the sound should be observed at high frequencies.

An analysis of the energy balance of a gas-discharge plasma shows that in addition to kinetic energy, the plasma also possesses a potential binding energy for its particles, which is $U_s = 2\alpha n_0 N$ per mole.

For the two cases described above, the gas-discharge plasma has a high binding energy $U_s = 9.6 \times 10^3$ J at $T = 400$ K. This energy is approximately three times higher than the binding energy of molecules in the critical state and $\sim 10^3$ times higher than the ionization energy, and is of the same order of magnitude as the gaskinetic energy of 1 mole of air under normal conditions.

In addition to kinetic energy and ionization energy, the plasma generator also consumes binding energy during the generation of metastable particles.

Equation (4) shows that the increase in the velocity of sound in a gas-discharge plasma is determined by the parameter $\alpha(a)$.

It is therefore advisable to increase (within certain limits) the electric field strength to increase W .

It is also clear that heating of the gas conventionally leads to an increase in the velocity of sound (observation 9).

In conclusion, this investigation indicates that the proposed modification of the van der Waals equation for a real gas not only qualitatively, but also quantitatively, describes the anomalous gasdynamic effects observed in experiments to study acoustic and shock waves in a weakly ionized gas-discharge plasma.

¹ U. Ingard, Phys. Rev. **145**, 41 (1966).

² Y. Ishida and T. Idehara, J. Phys. Soc. Jpn. **35**, 1747 (1973).

³ M. Hasegawa, J. Phys. Soc. Jpn. **37**, 193 (1974).

⁴ U. Ingard and M. Schulz, Phys. Rev. **158**, 106 (1967).

⁵ L. D. Tsendin, Zh. Tekh. Fiz. **35**, 1972 (1965) [Sov. Phys. Tech. Phys. **10**, 1514 (1965)].

⁶ P. Kaw, Phys. Rev. **188**, 506 (1969).

⁷ N. L. Aleksandrov, A. P. Napartovich, A. F. Pal', A. O. Serov, and A. N. Starostin, Fiz. Plazmy **16**, 862 (1990) [Sov. J. Plasma Phys. **16**, 502 (1990)].

⁸ G. I. Mishin, Yu. L. Serov, and I. P. Yavor, Pis'ma Zh. Tekh. Fiz. **17**(11), 65 (1991) [Sov. Tech. Phys. Lett. **17**, 413 (1991)].

⁹ I. V. Basargin and G. I. Mishin, Zh. Tekh. Fiz. **66**(7), 198 (1996) [Tech. Phys. **41**, 742 (1996)].

¹⁰ A. I. Klimov, G. I. Mishin, A. B. Fedotov, and V. A. Shakhovatov, Pis'ma Zh. Tekh. Fiz. **15**(19), 31 (1989) [Sov. Tech. Phys. Lett. **15**, 800 (1989)].

¹¹ I. V. Basargin and G. I. Mishin, Pis'ma Zh. Tekh. Fiz. **11**, 209 (1985) [Sov. Tech. Phys. Lett. **11**, 85 (1985)].

¹² A. Yu. Gridin, A. I. Klimov, and G. I. Mishin, Pis'ma Zh. Tekh. Fiz. **16**(8), 30 (1990) [Sov. Tech. Phys. Lett. **16**, 295 (1990)].

¹³ G. I. Mishin, A. I. Klimov, and A. Yu. Gridin, Pis'ma Zh. Tekh. Fiz. **17**(16), 84 (1991) [Sov. Tech. Phys. Lett. **17**, 602 (1991)].

¹⁴ L. D. Landau and E. M. Lifshitz, *Statistical Physics*, Parts 1 and 2, 3rd ed. (Pergamon Press, Oxford, 1980) [Russ original, Nauka, Moscow, 1976, 1978].

Translated by R. M. Durham

Physical model of the formation of a periodic structure on the surface of pyrolytic graphite under high-energy ion bombardment

D. V. Kulikov, A. L. Suvorov, R. A. Suris, Yu. V. Trushin, and V. S. Kharlamov

A. F. Ioffe Physicotechnical Institute, Russian Academy of Sciences, St. Petersburg;
Institute of Theoretical and Experimental Physics, Moscow
(Submitted March 25, 1997)

Pis'ma Zh. Tekh. Fiz. **23**, 89–93 (July 26, 1997)

A physical model is proposed for the formation of a structure consisting of “micropoints” and “cavities” on the surface of pyrolytic graphite bombarded by 210 MeV Kr^+ ions. This structure may be explained in terms of the depth distribution of the energy deposited by the bombardment. © 1997 American Institute of Physics. [S1063-7850(97)03407-1]

The experimental possibilities of using bombardment to modify the surface of various types of graphite to produce emission cathodes with a periodic surface structure were investigated by us in Refs. 1–3. The surfaces were bombarded with 30–500 keV Ar, La, and Bi ions at doses of 10^{16} – 10^{18} cm^{-2} . The energy and dose, as well as the angle of incidence of the ions on the surface were varied. As a result, we obtained a system of randomly distributed micropoints on the surface of the sample, whose tips differed substantially in terms of height and curvature.

In Ref. 4 we reported results of the bombardment of highly oriented pyrolytic graphite (HOPG) by a high-energy ion beam, which produced a periodic “micropoint–cavity” structure on the surface of the material. Here we propose a physical model for this effect, based on analyzing the energy released by inelastic interaction between the incident ions and the material.

In Ref. 4 samples of pyrolytic graphite were bombarded by 210 MeV Kr^+ ions with a dose of 4.3×10^{12} cm^{-2} , the flux density of the incident particles was $\sim 10^{10}$ $\text{ions} \cdot \text{cm}^{-2} \cdot \text{s}^{-1}$, and the ions were incident perpendicular to the surface. The periodic structure formed on the surface was examined using an STM/NL-20 scanning tunneling microscope operating in air. The average height of the micropoints was ap-

proximately 60 Å and the average spacing between them was around 170 Å (see Ref. 14).

The formation of micropoints on the surface of carbon samples under ion bombardment may be described in terms of the depth distribution of the energy deposited by the bombardment. Calculations performed using the TRIRS program^{5,6} show that when pyrolytic graphite is bombarded by 210 MeV Kr^+ ions, the inelastic losses extend to appreciable depths h , of the order of hundreds of thousands of angstrom (Fig. 1). To a depth $h = 50\,000$ Å the losses are almost constant, and the energy released is dissipated in heating the material. Using data on the energy release (see Fig. 1), calculations were made of the temperature distribution in the track of an incident ion using a formula presented in Ref. 7:

$$T(r, t) = \frac{F_D(h)}{4\pi\zeta t} \exp\{-C_V r^2 / (4\zeta t)\} + T_0.$$

Here r is the distance along the radius of the particle track, t is the time, F_D is the energy dissipated in ionization per unit length, h is the depth of penetration of the ion, ζ is the thermal conductivity, C_V is the specific heat per unit volume, and T_0 is the irradiation temperature.

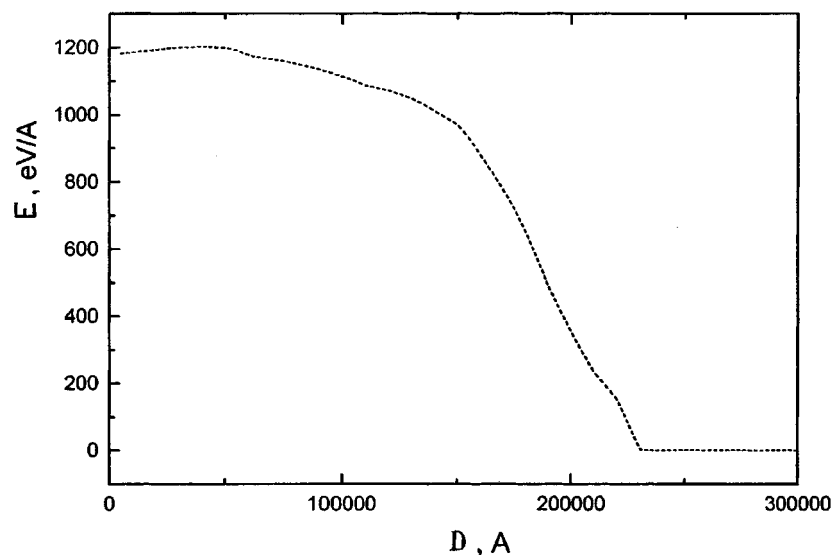


FIG. 1. Energy dissipated in ionization versus depth of ion penetration when pyrolytic graphite is bombarded by a 210 MeV Kr^+ ion.

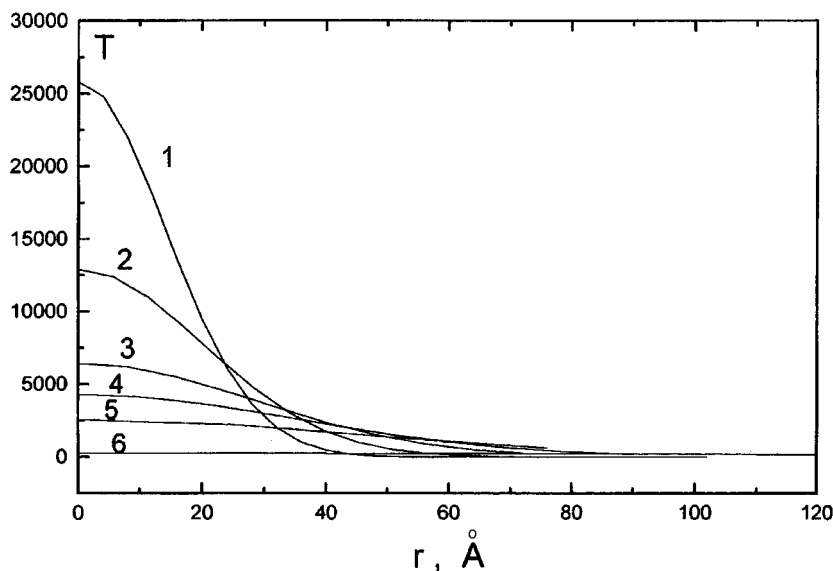


FIG. 2. Temperature of pyrolytic graphite as a function of distance from ion track at various times after transit of the ion: 1 — $t=1 \times 10^{-13}$ s, 2 — $t=2 \times 10^{-13}$ s, 3 — $t=4 \times 10^{-13}$ s, 4 — $t=6 \times 10^{-13}$ s, 5 — $t=1 \times 10^{-12}$ s, and 6 — $t=1 \times 10^{-11}$ s.

Calculations of the temperature $T(r,t)$ according to this formula were made for graphite with the following parameters: $F_D=1200$ eV/Å, $\zeta=40$ W/(m·K), $C_V=4000$ kJ/(m³·K) (Ref. 8), and melting point 4200 K (Ref. 9). It can be seen from the results of calculating the temperature $T(r,t)$ for various times (see Fig. 2) that at 6×10^{-13} s, the temperature in regions of approximately 100 Å diameter exceeds the melting point. Thus, intensive remelting of the material may occur along the track of the bombarding particle. Then, after approximately 10^{-10} s, the material rapidly cools down.

It is known^{10,11} that pyrolytic graphite contains both crystalline (*cr*) and amorphous (*a*) components, with the crystalline component accounting for a significantly greater fraction. Remelting of the crystalline phase by the energy released by the incident ion may cause the formation of the amorphous phase as a result of the rapid cooling (around 10^{-12} s, see Fig. 2). However, the densities (*d*) of these phases differ: $d_{cr}=2.26$ g/cm³ and $d_a=1.8$ g/cm³. Thus, a volume difference is established during cooling with the formation of an amorphous phase and it is supposed that this may help to “squeeze out” the excess volume to the surface. The average volume of a single micropoint can be estimated experimentally as $V=\pi R^2 h/3 \approx 6 \times 10^5$ Å³, by approximating the micropoint by a cone with base radius $R=100$ Å and height $h=60$ Å. Since the densities of the amorphous and crystalline phases differ by approximately a factor of 1.2, this squeezed-out excess volume is approximately 20% of the volume of the remelted crystalline phase from which this micropoint was formed. Thus, the volume of the remelted crystalline phase along the track of a single ion is $V_{cr} \approx 5 \cdot V = 3 \times 10^6$ Å³. If we assume that the graphite undergoes remelting in a cylindrical region of radius $R_{cr}=50$ Å along the ion track, we find that the depth from which excess atoms are squeezed out to the surface is $h_{cr} \approx 400$ Å, which is substantially less than the depth at which energy is released

by inelastic losses. These initial micropoints have the result that the subsequent bombarding particles are incident on a severely distorted surface on which a highly stressed structure is formed. The stress field of stresses in the crystalline phase of the pyrolytic graphite, formed by inclusions of remelted amorphous phase, possibly determine the conditions for the formation of subsequent micropoints, which may result in their ordering. However, an equally probable explanation for the formation of these periodically distributed micropoints may involve the specific characteristics of the pyrolytic graphite. In order to refine this model and determine the physical conditions for the formation of periodically distributed micropoints on the surface, we need to obtain and analyze additional experimental data and use additional methods of investigation such as conventional scanning microscopy and x-ray structural analysis. The authors of Ref. 4 and this Letter propose to perform these studies.

¹A. L. Suvorov *et al.*, Rev. “Le Vide, les Couches Minces,” No. 271, Suppl., 326 (1994).

²A. L. Suvorov *et al.*, *Final Program and Abstracts of NANO 3*, Denver, CO, 1994, p. 306.

³A. L. Suvorov, E. P. Sheshin, V. V. Protasenko *et al.*, Zh. Tekh. Fiz. **66**(7), 172 (1996) [Tech. Phys. **41**, 719 (1996)].

⁴A. L. Suvorov, Yu. V. Trushin, R. A. Suris *et al.*, in *Proceedings of the 43rd International Field Emission Symposium*, Moscow, 1996, p. 90.

⁵E. E. Zhurkin, in *Proceedings of the Eleventh Conference on Ion-Surface Interaction*, Moscow State University, 1993, Vol. 3, p. 105.

⁶B. Ya. Ber, E. E. Zhurkin, A. V. Merkulov, Yu. V. Trushin, and V. S. Kharlamov, Zh. Tekh. Fiz. **66**(3), 54 (1996) [Tech. Phys. **41**, 261 (1996)].

⁷M. Nastasi and J. V. Mayer, Radiat. Eff. Def. Solids **130/131**, 367 (1994).

⁸N. S. Rasor and J. D. McClelland, J. Phys. Chem. Solids **5**, 17 (1960)].

⁹S. V. Shulepov, *Physics of Carbon Materials* [in Russian], Metallurgiya, Chelyabinsk (1990).

¹⁰G. E. Bacon, Acta Crystallogr. **3**, 137 (1950).

¹¹E. S. Pugacheva, I. E. Il'cheva, A. P. Kalinovskii, O. I. Buzhinskiĭ, and I. V. Opimakh, Poverkhnost' Fiz. Khim. Mekh. No. 9, 71 (1995).

Translated by R. M. Durham